

**Design studies on
Cardiovascular & Intraoperative
Brachytherapy
and Multiphase Flow Metering**

New applications of radiation in medicine and industry

M. C. Clarijs

Cover design: Jan van Waarden, Ram Vormgeving, Asperen



The research described in this thesis was performed at the Radiation Technology Group of the Interfaculty Reactor Institute (IRI), Delft University of Technology, Mekelweg 15, 2629 JB Delft, The Netherlands.

**Design studies on
Cardiovascular & Intraoperative
Brachytherapy
and Multiphase Flow Metering**

New applications of radiation in medicine and industry

PROEFSCHRIFT

ter verkrijging van de graad van doctor
aan de Technische Universiteit Delft,
op gezag van de Rector Magnificus prof. ir. K. F. Wakker,
voorzitter van het College voor Promoties,
in het openbaar te verdedigen op maandag 8 januari 2001 om 10.30 uur

door

Martijn Christian CLARIJS

natuurkundig ingenieur
geboren te Schiedam

Dit proefschrift is goedgekeurd door de promotor:
Prof. dr. ir. C.W.E. van Eijk

Samenstelling promotiecommissie:

Rector Magnificus,	voorzitter
Prof. dr. ir. C.W.E. van Eijk,	Technische Universiteit Delft, promotor
Prof. dr. ir. A.H.M. Verkooijen,	Technische Universiteit Delft
Prof. dr. ir. T.H.J.J. van der Hagen,	Technische Universiteit Delft
Prof. dr. H. Postma,	Technische Universiteit Delft
Prof. dr. J.J. Broerse,	Universiteit Leiden
Dr. ir. V.R. Bom,	Technische Universiteit Delft
Ir. A.M. Scheers,	Shell Int. Exploration and Production

Published and distributed by: DUP Science

DUP Science is een imprint van
Delft University Press
P.O. Box 98
2600 MG Delft
The Netherlands
Telephone: +31 15 2785121
Telefax: +31 15 2781661
E-mail: DUP@Library.TUDelft.NL

ISBN 90-407-2066-5

Copyright © 2000 by M.C. Clarijs

All rights reserved. No part of the material protected by this copyright notice may be reproduced or utilized in any form or by any means, electronic or mechanical, including photocopying, recording or by any information storage and retrieval system, without written permission from the publisher: Delft University Press.

Printed in The Netherlands

“Making the simple complicated is commonplace; making the complicated simple, awesomely simple, that’s creativity.”

-- *Charles Mingus* (1922-1979)

Contents

1	Introduction	1
1.1	Study I: Modelling of a $^{188}\text{W}/^{188}\text{Re}$ beta line source for coronary brachytherapy by means of EGS4 Monte Carlo simulations.....	1
1.1.1	The problem of restenosis	1
1.1.2	Cause and nature of restenosis	2
1.1.3	Methods to control restenosis	3
1.1.4	Treatment with radiation	3
1.1.5	The biological target	4
1.1.6	Electron emitters	4
1.1.7	Photon versus beta irradiation.....	5
1.1.8	Potential beta emitters.....	5
1.1.9	Need for accurate dosimetry	6
1.1.10	Monte Carlo simulations.....	7
1.1.11	Aim of the study.....	7
1.2	Study II: Feasibility of an intraoperative brachytherapy source	8
1.2.1	Cancer treatment with radiation	8
1.2.2	Radiation therapy in combination with surgery.....	8
1.2.3	The advantages of intraoperative brachytherapy	9
1.2.4	Remote afterloading	10
1.2.5	Shielding problems with current IOBT.....	10
1.2.6	Rationale: achieving 'real' IOBT.....	10
1.2.7	Aim of the study.....	11
1.3	Study III: Design of an X-ray setup for a multiphase flow metering device	11
1.3.1	Changes in multiphase flow metering techniques	11
1.3.2	Flexible multiphase flow metering	12
1.3.3	Dual Energy Gamma-Ray Absorption.....	12
1.3.4	The (dis)advantages of the DEGRA technique.....	12
1.3.5	The benefits of an X-ray tube	13
1.3.6	Water salinity	13
1.3.7	Aim of the study.....	13

Study I: Modelling of a $^{188}\text{W}/^{188}\text{Re}$ beta line source for coronary brachytherapy by means of EGS4 Monte Carlo simulations

2	Simulation models of the coronary brachytherapy source.....	17
2.1	Introduction.....	17
2.2	Source requirements.....	17
2.2.1	Irradiation in the coronary artery	17
2.2.2	Dose homogeneity.....	18
2.2.3	Source centring	18
2.3	Rationale of $^{188}\text{W}/^{188}\text{Re}$	19
2.3.1	The $^{188}\text{W}/^{188}\text{Re}$ electron spectrum	19
2.3.2	Neutron activation.....	21
2.4	The source design	22
2.4.1	Rationale of the tungsten line source	22
2.5	Radionuclide spectra.....	23
2.5.1	$^{188}\text{W}/^{188}\text{Re}$ photon spectrum	24
2.5.2	^{185}W and ^{181}W spectra.....	24
2.6	EGS4 and DOSRZ	26
2.7	The solid tube model with density correction (DENCOR).....	28
2.8	The solid tube model with diameter correction (DIACOR)	29
2.9	The square rings model (SR)	30
3	Simulation results for the therapeutic depth-dose distribution in water	31
3.1	Representation format.....	31
3.1.1	Formalisms for endovascular line sources.....	32
3.1.2	Alternative source characterization.....	32
3.1.3	Verification of simulated depth-dose distributions in water.....	33
3.2	Simulation results for $^{188}\text{W}/^{188}\text{Re}$ electrons	33
3.3	Simulation results for $^{188}\text{W}/^{188}\text{Re}$ gamma/X-rays.....	35
3.4	Other depth-dose rate contributions.....	35
3.5	Use of the source models	36
4	Comparison with experimental data	39
4.1	Phantom measurements with TLDs.....	39
4.1.1	The PMMA phantom	39
4.1.2	The thermoluminescent detector (TLD)	40
4.2	Corrections to experimental data	42
4.2.1	Influence of TLD size	42
4.2.2	Influence of TLD insensitive base	42
4.3	Comparison between experiment and simulation for PMMA	43
4.4	Final results for the therapeutic depth-dose rate distribution in water.....	44
4.4.1	The therapeutic depth-dose rate distribution.....	44
4.4.2	Source activity for therapy	45
4.4.3	Effective source length L_{eff} based upon $z_{\text{max}}(r)$	46
4.4.4	Depth-dose distribution for small r and at source ends.....	47
4.4.5	Conclusions for therapeutic depth-dose rate distribution in water	48

5	Radiation safety during therapy	49
5.1	Dose received by patient and medical staff	49
5.1.1	Dose received by patient	49
5.1.2	Dose received by medical staff	50
5.1.3	Determination of air kerma rates	50
5.2	Simulation model of the source and water shielding	51
5.2.1	The simulation concept for air kerma	51
5.3	Contributions to air kerma rate	51
5.3.1	Simulated gamma/X-ray contributions	51
5.3.2	Simulated bremsstrahlung contributions	52
5.3.3	Simulated fluorescence X-rays contributions	52
5.3.4	Verification of simulated air kerma rate for $^{188}\text{W}/^{188}\text{Re}$	53
5.4	Final results for radiation safety during therapy	54
5.4.1	Experimental data	54
5.4.2	Total air kerma rate during therapy	55
5.4.3	Beta dose rate from unshielded source	56

Study II: Feasibility of an intraoperative brachytherapy source

6	Radiation output requirements for an intraoperative brachytherapy source	59
6.1	Introduction	59
6.1.1	Requirements for an IOBT source	60
6.2	Source applicator	60
6.3	Calculational model of source and applicator	61
6.3.1	The point source grid	61
6.3.2	Accumulated depth-dose	63
6.3.3	Outline for therapeutic analysis	64
6.4	Compton scattering and dose build-up factors	64
6.5	Therapeutic dose distributions	67
6.5.1	Required intermediate photon yield (I)	67
6.5.2	Required intermediate photon yield (II)	69
6.5.3	Transversal homogeneity in the target	72
6.5.4	Lateral homogeneity in the prescription plane	73
6.5.5	Source capsule absorption	74
6.5.6	Final values for the required intermediate photon yield	76
6.6	Calculations on radiation safety	77
6.6.1	Therapeutic energies below 100 keV	78
6.6.2	Shielding of energies above 100 keV	79
7	Selection of radionuclides for application in IOBT	81
7.1	Outline for feasibility analysis	81
7.1.1	Therapeutic requirements	82
7.1.2	Shielding requirements	82
7.2	Suitability of ^{125}I	83

7.2.1	Maximum specific activity.....	83
7.3	Production of ^{125}I	84
7.3.1	Compartment model algorithm	84
7.3.2	Neutron activation of ^{124}Xe	86
7.4	^{125}I photon yield in an IOBT source	87
7.4.1	Influence of a carrier on ^{125}I abundance and self-absorption.....	87
7.4.2	Feasibility of ^{125}I as an IOBT source	88
7.5	Shielding of photons from ^{126}I	89

Study III: Design of an X-ray setup for a multiphase flow metering device

8	Multiphase flow metering based on photon absorption	93
8.1	Introduction.....	93
8.2	The Dual Energy Gamma Ray Absorption principle.....	94
8.3	The DEGRA meter	95
8.4	X-ray composition meter requirements	95
8.4.1	Salinity	97
8.5	Feasibility of integrated salinity determination	97
8.5.1	The Multiple Energy X-ray Absorption principle.....	97
8.5.2	Parametrization of photon-matter interaction	98
8.5.3	Analytical solution	100
8.5.4	Sensitivity of MEXA analysis (I).....	100
8.5.5	Conclusions for the feasibility	101
8.6	Optimum X-ray spectra for MEXA	101
8.6.1	Analysis.....	102
8.6.2	Monoenergetic X-rays.....	102
8.6.3	Sensitivity of MEXA analysis (II)	103
8.6.4	Optimum set of energies	103
9	Transmission Secondary Fluorescence X-ray Spectra.....	105
9.1	Rationale of the Transmission Secondary Fluorescence X-ray set-up	105
9.1.1	The primary X-ray spectrum.....	105
9.1.2	Rationale of secondary fluorescence.....	107
9.1.3	Rationale of an end-window X-ray tube	107
9.2	Simulation of a TSFX set-up	107
9.2.1	The anode.....	108
9.2.2	Simulation of bremsstrahlung	109
9.2.3	Electron impact ionization in EGS4	111
9.2.4	The secondary fluorescence foils.....	111
9.2.5	Calculation of normalized intensities.....	112
9.3	Initial results from simulations	112
9.4	Quantitative verification	114
9.4.1	Bremsstrahlung intensity.....	114
9.4.2	Sm K_{α} fluorescence intensity.....	115
9.4.3	Ag K_{α} fluorescence intensity	115

9.5 The optimized TSFX spectrum.....	116
9.5.1 MPFM with the optimized TSFX spectrum.....	117
9.6 Comparison with measurements.....	117
9.6.1 Experimental set-up.....	118
9.6.2 Simulation of the experimental set-up.....	119
9.6.3 Data processing.....	120
9.6.4 Results.....	121
10 Reflection Secondary Fluorescence X-ray Spectra.....	123
10.1 Simulation of a RSFX set-up.....	123
10.1.1 The anode.....	125
10.1.2 Foil order.....	125
10.2 Results from simulations.....	126
10.2.1 Comparison between the RSFX set-ups.....	126
10.2.2 Influence of foil rotation.....	127
10.2.3 The optimized RSFX spectrum.....	127
10.3 Comparison with measurements.....	129
10.3.1 Results.....	129
10.4 MPFM with RSFX spectra.....	130
10.5 The prototype RSFX set-up for MPFM.....	131
10.5.1 The Trufocus MAX-10 X-ray tube.....	131
10.5.2 The Amptek XR-100CR Si detector.....	132
10.5.3 Inclusion of the second detector.....	133
10.5.4 The foil holder assembly.....	134
10.6 Simulation of the prototype RSFX set-up.....	135
10.6.1 The fluorescence foil order.....	136
10.6.2 The optimized spectrum for the prototype RSFX set-up.....	136
11 Conclusions.....	139
11.1 Study I: Modelling of a $^{188}\text{W}/^{188}\text{Re}$ beta line source for coronary brachytherapy by means of EGS4 Monte Carlo simulations.....	139
11.2 Study II: Feasibility of an intraoperative brachytherapy source.....	141
11.3 Study III: Design of an X-ray setup for a multiphase flow metering device.....	142
References.....	145
Abbreviations.....	153
Summary.....	155
Samenvatting.....	161
Dankwoord / Acknowledgements.....	167
Curriculum Vitae.....	169

1 Introduction

In medicine, radiation is used for therapeutic and diagnostic purposes. The therapeutic application of radiation is as a means of dose deposition in order to prevent or cure a disease. In diagnostic applications radiation is used to inspect the internal parts of the (human) body, e.g. by means of radiotracers, scanning and tomographic techniques, as discussed by Smith et al. (1995). Non-medical applications also make use of the diagnostic qualities of radiation, e.g. for non-destructive testing in quality control of materials and constructions, and non-invasive inspection techniques, such as luggage control at airports and monitoring of multiphase flows in the chemical and process industry, as discussed by Chaouki et al. (1997).

In this thesis, three studies on relatively new applications of radiation in medicine and industry are presented. The use of Monte Carlo (hereafter: MC) simulations plays an important role in all three studies. In this introductory chapter we discuss the background to each of the studies.

1.1 Study I: Modelling of a $^{188}\text{W}/^{188}\text{Re}$ beta line source for coronary brachytherapy by means of EGS4 Monte Carlo simulations

1.1.1 The problem of restenosis

One of the relatively new therapeutic applications of radiation lies in the field of restenosis prevention. The potential role of radiation in preventing restenosis was first discussed by Dawson (1991). Restenosis can be defined as the re-narrowing of an artery following interventions aimed at taking away obstructions in the blood vessel. In this context, we speak of re-narrowing in a later phase, since with availability of modern techniques acute closure of the arteries due to recoil of the elastic blood vessel wall is relatively uncommon. The degree of narrowing is usually arbitrarily defined as a percentage of the lumen (see section 1.1.2) diameter or cross-section in the adjacent normal artery segments.

Not only is restenosis a possible cause of major complications in coronary arteries with lethal consequences, but also an important adverse result is economic. This can be understood by the fact that coronary artery disease is the leading cause of morbidity and mortality in the western world, as discussed by Levy (1979). Approximately 450,000 angioplasties (see below

for explanation) are performed annually in the USA. Although major complications from angioplasty occur in only 1%-2% of patients, angiographically^{*} diagnosed restenosis occurs in 35%-40% of patients, as discussed by Pocock et al. (1995). Restenosis may necessitate repeated angioplasty treatment which results in extra costs. The societal cost of restenosis in the United States of America is estimated between 800 and 2000 million dollars per year.

1.1.2 Cause and nature of restenosis

Restenosis may for instance occur after a procedure known as Percutaneous Transluminal Coronary Angioplasty[†] (hereafter: PTCA). Levy (1979) discusses how in 1977, Gruentzig introduced a new dimension to the field of interventional cardiology by performing the first coronary balloon angioplasty. The primary objective of angioplasty is to re-establish a stable lumen[‡] with a diameter similar to that of the normal artery. This is achieved by inflating a balloon within the coronary artery in order to stretch the blood vessel wall, aimed at taking away a vascular lesion. It has been observed however that the artery may become obstructed again following PTCA due to three separate mechanisms which are elaborately described by King (1996) and which will briefly be touched upon here. The medical terminology is covered by Nath et al. (1999).

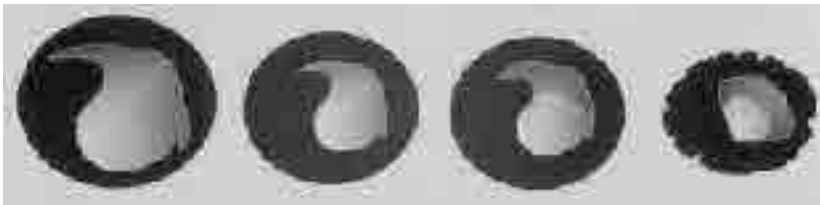


Figure 1.1 From left to right: Post dilatation and the components of restenosis: early recoil, neointima formation and late contraction. Reprinted by courtesy of Nucletron B.V. and S. B. King.

Figure 1.1 depicts the different stages in the process of restenosis. Chronologically, the first is the elastic recoil which occurs promptly after the overstretch of the artery and does not seem to progress much beyond the first few minutes after balloon deflation. The second component of restenosis is intimal proliferation, resulting in new tissue growth occupying the cracks and tears in the vessel wall and sometimes growing to produce a very severe reobstruction of the artery. This process probably begins within days after angioplasty and continues for weeks or months. The third mechanism for restenosis which has been recently elucidated is analogous to wound contracture. The entire artery may become contracted so that the external elastic lamina occupies a smaller circumference than it did following the procedure. It has been

^{*} Angiogram – X-ray image of a blood vessel filled with a contrast medium.

[†] Percutaneous – through the skin, Transluminal – through the lumen of a vessel, Coronary – pertaining to the heart, Angioplasty – repair of a blood vessel. PTCA is usually synonymous with balloon angioplasty.

[‡] Lumen – space in the interior of a tubular structure. In this context: part of the blood vessel through which the blood flows.

estimated by Mintz et al. (1994) that this process may account for up to 60%-65% of the lumen loss judged by intravascular ultrasound.

1.1.3 Methods to control restenosis

In the early stages of angioplasty, attempts to control the process were made using a wide variety of methods, discussed by King (1996). Trials with various drugs and agents have been performed but the general conclusion is that no drug has yet been recognized or generally used for restenosis prevention. Besides the balloon angioplasty treatment as discussed above, there are other methods for achieving increased lumen size with new interventional devices, discussed by Nath et al. (1999). They fall into two general categories:

- atherectomy or tissue removing techniques: in cases where balloon angioplasty cannot be used it may be possible to remove tissue by cutting (atherectomy device), abrading (rotoblator) or vaporizing (laser).
- stenting or vascular splinting techniques which resist elastic recoil and minimize loss of lumen diameter due to remodelling.

Because the risk of arterial wall perforation is clearly much higher with tissue removing techniques, they are only used to initially “debulk” the lesion, and then followed by balloon angioplasty and/or stent placement. Although stents are being placed in an increasing fraction of PTCA procedures as they significantly improve the short term result of angioplasty, they do not appear to eliminate neointima formation and may in fact actually stimulate obstructive tissue growth. It is for this reason that there is a strong interest in finding a method, such as radiation therapy, which can be used in conjunction with, or instead of stenting to produce a definitive answer to the restenosis problem.

1.1.4 Treatment with radiation

Several groups investigating the use of ionizing radiation to prevent restenosis following (cardio-) vascular procedures such as PTCA have reported on a possible beneficial effect of radiation on the rate of restenosis. A recent overview of research on dosimetry for endovascular brachytherapy by a number of different Dutch groups is given by Dries et al. (1999). More specific, recent preclinical studies have indicated that irradiation in the dose range of 15-30 Gy may reduce the problem of restenosis in patients who have undergone an angioplasty.

Various means to deliver a therapeutic dose of radiation to the vascular lesion have been investigated, including e.g. irradiation with external beams of different types of radiation and endovascular brachytherapy, i.e. irradiation by means of balloon catheters filled or coated with radioactive materials and radioactive stents. We speak of brachytherapy whenever the irradiation is performed with the radioactive source nearby or in close contact with the biological target.

Waksman (1996) estimated that the restenosis rate may drop from roughly 35%-40% to well below 10% if radiation is delivered to the obstruction site during or after an angioplasty. The potential of intravascular brachytherapy therefore has aroused much interest in the cardiology community.

1.1.5 The biological target

The length of the lesion to be treated is usually in the order of several centimeters. As far as the radial target dimensions are concerned, the dosimetry of intravascular brachytherapy is in the millimeter range. Whereas in traditional brachytherapy the dose is typically specified at 1 cm from the source (cf. Study II in this thesis, Chapters 6 and 7), in intravascular brachytherapy the lesion is 1 to 3 mm in thickness. In this context, it is also important to denote that consensus on the exact dimensions and nature of the biological target to be irradiated is not achieved to date. It is therefore not possible to assign a definite value to the target depth in the vessel wall. As this subject has recently been reviewed by a number of authors, the interested reader is referred to the following authors for details and further references: Nath et al. (1999), Bertrand et al. (1997), Diamond et al. (1998a, 1998b), Weinberger et al. (1997), Waksman et al. (1999). As a consequence of the lack of a well-defined target depth, accurate dosimetry over the full radial range up to the maximum possible target depth should be ensured. This is further discussed in section 1.1.9. In principle there are two candidate types of radiation for intravascular brachytherapy: electrons and photons.

1.1.6 Electron emitters

For both irradiation with electron and photon sources in the application of intravascular brachytherapy, the energy of the radiation emitted by the source must be such that the dose is delivered in the millimeter region. This implies that the energy of the emitted electrons must be about 1 MeV, in agreement with values mentioned in the literature by Nath et al. (1999).

Electron emitters such as metastable isotopes showing internal conversion and electron-capture isotopes emitting Auger electrons are therefore not suitable since the energy of the electrons is too low (although these radionuclides may serve well as low energy gamma and/or X-ray sources). Beta emitters however seem appropriate for the treatment of restenosis as the short spatial range and high dose deposition from beta radiation with energies in the order of 1 MeV allows treatment to be focused in the small diametrical dimensions of a blood vessel.

Two types of beta emitters exist: β^- emitters that emit electrons and β^+ emitters that emit positrons. When a positron is absorbed in matter, two 511 keV annihilation gammas are created. This is a serious disadvantage in case of a vascular brachytherapy source as it will increase the effective dose received by a member of the medical staff. For this reason positron emitters are not considered suitable for intravascular brachytherapy, and hereafter the term beta exclusively refers to β^- radiation.

1.1.7 Photon versus beta irradiation

Most intravascular brachytherapy studies to date have used ^{192}Ir gamma emitters and for some time it was the only available type of source for this application. An advantage of gamma emitters is that they generally deliver a more uniform dose to the vessel wall (especially for higher energies) than beta emitters.

The more fundamental problem with high energy gamma emitters such as ^{192}Ir is the relatively low energy deposition at the target distance of several millimeters, and on the other hand the increased radiation safety problems for corresponding high source activities. In the context of radiation safety, beta emitters have the advantage of little or no dose deposition beyond the target volume because of the finite range of beta particles which is in the order of several millimeters, as discussed by e.g. Weinberger (1996).

The energy deposition in water by photons with energies in the order of 10 keV is predominantly in the prescribed target-depth range of several millimeters. Photons with energies in the order of 10 keV are characterized by the same numerical values for the interaction coefficients as electrons with energies around 1 MeV. Thus, as the fluence rate is proportional to the source activity, in order to obtain the same dose rate, the source activity per unit volume must be about 100 times higher for a photon source than for a beta source with equal dimensions. Schaart (1995a) estimates that the required activity of a beta source with energies around 1 MeV is in the order of 10 to 100 mCi (i.e. 370 to 3700 MBq, since $1 \text{ Ci} = 3.7 \times 10^{10} \text{ Bq}$), in agreement with Weinberger (1996). Required source activities for low energy gamma and X-ray emitters may thus well be considerably larger than 1 Ci, which is higher than those currently available, as is discussed for ^{125}I and ^{103}Pd by Nath et al. (1999).

Although the required source activity is lower for higher energy photon emitters, the energy deposition at the target distance of several millimeters is still relatively low, and on the other hand radiation safety problems remain larger than with beta emitters. The conclusion must be that beta emitters are in principle more suitable than photon emitters. What is new in the field of intravascular brachytherapy is that much recent effort has been directed towards the development of beta sources, as discussed by Weinberger (1996).

1.1.8 Potential beta emitters

Different activation techniques to obtain beta sources were compared, either via neutron capture inside a reactor, or via activation with heavy charged particles (accelerated to an energy of 10 to 100 MeV) such as protons, deuterons or alpha-particles from a cyclotron. The source radionuclide may also be a fission product, produced in a nuclear reactor. Activation with charged particles does not seem promising due to the short irradiation times in the order of a day; this means that the half-life of the source must be short in order to reach sufficient source activity. Higher (specific) source activities can be achieved by means of radiochemical techniques, but this implies that the source can only be manufactured and encapsulated after activation. Based on the above arguments, it seemed best to concentrate on neutron activated

beta sources, also since activation via an (n, γ) reaction has the advantage that the source can be constructed and encapsulated before neutron activation.

Schaart (1995b) selected a number of 12 beta emitters which were considered suitable for a vascular brachytherapy source. The selection was based upon requirements that concern the emission, activation and mechanical properties of the source material, which means that the selected radionuclides are favourable from a physical point of view. For example, economical and logistic aspects were not included in the selection procedure.

Although each of the selected isotopes can in principle be used in a vascular brachytherapy source, some are more attractive than others depending on the properties that are considered most important. For instance, amongst those selected, isotopes such as $^{90}\text{Sr}/^{90}\text{Y}$, $^{106}\text{Ru}/^{106}\text{Rh}$ and $^{144}\text{Ce}/^{144}\text{Pr}$ are most preferable in terms of high maximum beta energies $E_{\text{max}} = 2.3 \text{ MeV}$, 3.5 MeV and 3.0 MeV , respectively, taken from Sowby et al. (1983), and long half-lives $t_{1/2} = 29 \text{ y}$, 368 days and 284 days , respectively. A relatively low dose to the medical staff due to photons emitted by the source is expected from ^{32}P , $^{90}\text{Sr}/^{90}\text{Y}$, ^{89}Sr , ^{91}Y (and to some degree from ^{123}Sn and $^{144}\text{Ce}/^{144}\text{Pr}$). Other isotopes, such as ^{32}P and ^{86}Rb (and to some degree $^{188}\text{W}/^{188}\text{Re}$ and $^{115\text{m}}\text{Cd}$) are considered suitable as they can be produced with sufficient activity by direct neutron activation.

It was decided to use the isotope combination $^{188}\text{W}/^{188}\text{Re}$ for the development of a prototype coronary brachytherapy source. The main rationale for this choice is the fact that the metal tungsten can relatively easily be used in the construction of the source (see section 2.4.1). This was considered an important advantage that outweighs the fact that relatively high neutron fluxes are required to activate the source. The neutron activation and the emission properties of $^{188}\text{W}/^{188}\text{Re}$ are further discussed in section 2.3.

1.1.9 Need for accurate dosimetry

It is important for the radiation source to be characterized and calibrated adequately prior to clinical use. As there are indications that too low a dose may actually stimulate restenosis while excessively high doses may lead to dangerous late complications (see e.g. Bertrand et al. (1997), Diamond et al. (1998b)), knowledge of the dose distribution around the source is vital to successful treatment. This knowledge furthermore allows for the evaluation, interpretation and comparison of the results of the various clinical studies to be conducted with different devices.

Treatment can be performed by directly advancing the source into the coronary artery, or, more likely, into a conventional or slightly modified balloon catheter. In either case, it is desirable that the source be centred within the coronary artery to ensure uniform dose to the arterial walls. Asymmetry in the radial dose profiles resulting from inaccurate source centring can be a factor of two or even more, with beta sources yielding even larger asymmetries than gamma sources.

In addition to the problem of source centring, the ultimate success of treatment may also depend on the definition of the target, as mentioned in section 1.1.5. If, for example, a minimum dose of 15 Gy is required to prevent restenosis, and the inner as well as the outer parts of the artery (lumen and adventitia, respectively) must all be treated, depth-dose considerations alone indicate dose asymmetries of at least 50%, as discussed by Weinberger (1996). It may thus be difficult to deliver an adequate dose to all target tissues without overdosing other tissues. This is further complicated by significant local curvature in the coronary artery, which is not uncommon. Thus, in anticipation of a well-defined target depth, accurate dosimetry over the full radial range up to the maximum possible target depth is essential for both the efficacy and safety of the therapy.

At radial distances smaller than 5 mm, which are of interest in intravascular brachytherapy, measurements are difficult due to the large dose gradients and other technical considerations, discussed by Nath et al. (1999). Dose perturbations caused by scatter and self-absorption of low-energy secondary radiations also make analytical calculations difficult.

1.1.10 Monte Carlo simulations

Monte Carlo computer simulations with the EGS4 code can provide excellent possibilities for achieving accurate source dosimetry. These simulations describing the transport of electrons and photons through matter can provide a relatively quick method of inspection for radiation transport and dose deposition processes. It also yields information which often cannot be obtained from measurements, e.g. the distinction between scattered and unscattered radiation.

The EGS4 Monte Carlo code is an example of such a Monte Carlo computer simulation code that has been extensively adopted by the medical physics community. It is a well documented and tested public domain code. One is referred to Nelson and Jenkins (1980), Nelson et al. (1985) and Jenkins et al. (1987) for further documentation and details about EGS4.

1.1.11 Aim of the study

The aim of Study I is to quantify the absolute dose distribution about the prototype $^{188}\text{W}/^{188}\text{Re}$ beta source for coronary brachytherapy by means of EGS4 Monte Carlo simulations. In particular, (1) the absolute dose rate over the full radial range up to the maximum possible target depth in the vessel wall and (2) the homogeneity of the dose distribution in the vessel wall in the direction along the lesion must be quantified, as these are decisive for the suitability of the source for the application of restenosis prevention after PTCA.

In addition to the above, the air kerma rate that members of the medical staff are exposed to during treatment must be determined in order to estimate the radiation safety of the $^{188}\text{W}/^{188}\text{Re}$ beta source.

1.2 Study II: Feasibility of an intraoperative brachytherapy source

1.2.1 Cancer treatment with radiation

Radiation therapy for cancer treatment can be divided into three areas. Firstly, nuclear medicine involves the use of radionuclides as open sources in the human body, as discussed by Smith et al. (1995); this means that the radionuclide (as a pure emitter or compound) is not enclosed in or shielded by any source capsule or container, and is distributed in the human body as it is in direct contact with organs, tissues or blood flow.

A well-known example is the use of radioactive iodine for irradiation of the thyroid gland. Secondly, teletherapy is performed with charged or uncharged particle beams which are used to irradiate the body from outside. The background to this application is e.g. discussed by Khan (1992). Thirdly, we speak of brachytherapy as opposed to teletherapy, whenever an enclosed radiation source is at a short distance from, or in direct contact with the tumour or tumour bed.

The nature and location of the tumour in the body dictate the specific treatment by means of brachytherapy. For example, so-called interstitial brachytherapy is applied in treatment of cancer in the head, neck and breast. It involves the use of needles which are – often percutaneously (i.e. through the skin) – placed within the tumour and through which a radioactive source can be transported to the tumour. Intraluminal brachytherapy applies to the radioactive source placed inside a body lumen (tubular structure) and is used in treatment of e.g. rectal and oesophageal cancer. A third technique is so-called intracavitary brachytherapy, which demands the presence of a readily accessible body cavity for the delivery of brachytherapy dose by means of a source applicator. As an example of such a cavity, Nori (1994) mentions the treatment of primary cervical carcinoma that entails a brachytherapy dose boost of 40 Gy with external beam therapy to 45 Gy, adding up to a total dose deposition of 85 Gy at the prescribed position in the target.

1.2.2 Radiation therapy in combination with surgery

Radiation therapy by itself can be adequate for cancer treatment, however it is often performed during surgery to treat remainders of a tumour (bed) which are not surgically removed. This makes it possible to irradiate tumours that cannot be reached by means of the brachytherapy techniques mentioned above. It also enables selective irradiation of the tumour (bed) while minimizing the dose deposition in adjacent healthy tissues and organs, i.e. a high so-called conformity. A single, large dose boost in the order of 10 Gy is then delivered to a surgically exposed tumour or tumour bed while displacing or shielding some or all of the dose-limiting radiation-sensitive normal tissues.

In such situations, the term intraoperative radiation therapy (hereafter: IORT) is used for dose delivery by means of electron beams in the 6 to 18 MeV range produced by a linear accelerator. This may be done in a shielded surgery room with the use of a dedicated linear

accelerator, or the anesthetized patient may be moved to the radiation therapy suite for the treatment. The high dose boost during surgery is normally followed, after closure of the incision, by fractionated irradiation, i.e. delivery of several smaller dose fractions by means of conventional irradiation techniques during a time period up to several weeks, adding up to the required total dose deposition.

1.2.3 The advantages of intraoperative brachytherapy

Complementary to IORT, one speaks of intraoperative brachytherapy (hereafter: IOBT) when irradiation is performed during surgery with a brachytherapy source instead of with electron beam techniques. As discussed in section 1.2.1, treatment of primary cervical carcinoma entails a brachytherapy dose boost of 40 Gy. It is due to the inherent radiation tolerance of the local pelvic organs that such high doses can be used for the treatment of cervical carcinoma and cure can be achieved (although especially the rectum and bladder are dose-limiting sensitive organs). In contrast, other organs, e.g. the central and peripheral nervous structures, lung, kidneys and liver, each have dose limiting tolerances which, if exceeded, may lead to complications and increased morbidity.

It can be problematic to exclusively irradiate complex anatomical structures during surgery, particularly in the pelvis or chest, with available electron IORT techniques, as argued by Harrison (1995). It is often difficult to orientate the equipment such that these regions can be treated adequately without overexposing adjacent radiation-sensitive organs. In addition, it is quite expensive to either install a linear accelerator into a dedicated surgery room, or to equip a linear accelerator room with surgery facilities.

This seriously limits the number of medical centres that use this form of therapy. The alternative of transporting a patient under general anaesthesia from the surgery room to the radiation oncology department entails obvious safety concerns and logistic problems which result in relatively high treatment costs. These constraints have stimulated development of different techniques of more accurate dose delivery to the target site during surgery without overexposing surrounding dose-restricting organs.

In IOBT, a higher conformity can be achieved by using a radioactive source in combination with a source applicator. The applicator generally consists of a flexible material that can shape to any (surgically exposed) surface to which it is applied. It may contain an array of paths through which the radioactive source is transported, using a preprogrammed dwell time distribution. Harrison (1995) argues that the approximately $1/r^2$ dependence of the intensity from the radioactive source is favourable in order to achieve high conformity, the applicator thus becoming a radioactive mould for accurate dose deposition in the target area.

Furthermore, IOBT equipment is far less expensive than a linear accelerator and involves the use of a remote afterloader (see section 1.2.4), which is a portable unit that can be brought into the surgery room when needed and that can also be used for other irradiation procedures.

1.2.4 Remote afterloading

Iridium-192, a gamma emitter with a maximum and average gamma energy of 0.6 and 0.37 MeV, respectively (data taken from Lederer et al. (1978)), is a radionuclide commonly used in combination with the technique of so-called remote afterloading brachytherapy. Iridium-192 is for example used in the microSelectron-HDR afterloader, see Figure 1.2, taken from and discussed by van 't Hooft et al. (1996).

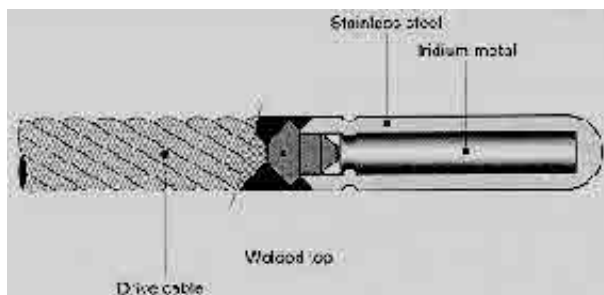


Figure 1.2 Schematic diagram of the Iridium-192 source and the microSelectron-HDR afterloader. Reprinted by courtesy of Nucletron B.V.

Afterloading, as the word suggests, implies that the radioactive sources are temporarily loaded into specially designed devices (such as applicators, needles or catheters), only after these have been positioned correctly in the human body. The radioactive source is then transported to the target site for irradiation by means of a drive wire, and back into a shielding container after the treatment. Whereas up to the mid-1970s brachytherapy sources were loaded manually, the use of remotely controlled afterloading machines has significantly reduced radiation hazards to the medical staff during treatment.

1.2.5 Shielding problems with current IOBT

Due to the maximum gamma energy of 0.6 MeV, the application of IOBT with iridium-192 is limited by possibilities of radiation shielding. In most treatment centres the applicators are inserted in the surgery theatre, but the radiation is delivered subsequently. As is the case with IORT, patients have to be brought from the surgery theatre to the radiation therapy department, which is costly, time-consuming and entails safety problems. Strictly speaking, it may therefore not be called intraoperative brachytherapy, but rather perioperative brachytherapy.

1.2.6 Rationale: achieving 'real' IOBT

Overcoming the radiation shielding problems while performing 'real' IOBT, is what is being aimed at in the development of a new IOBT source. Ideally, during the entire treatment period the patient is anaesthetised in the surgery theatre and the personnel is protected from exposure without having to leave the room. It is important to mention that when a member of the

medical staff is not qualified as a radiological worker, maximum doses for members of the public apply (see section 5.1.2), as recommended in ICRP Publication 60 (1990) by the International Commission on Radiological Protection (hereafter: ICRP).

This imposes strict requirements for the radiation output of a potential radionuclide. On one hand, the radiation yield from the radionuclide should be high enough to achieve the prescribed dose deposition within the available treatment time. On the other hand, it must be possible to shield the personnel from such a high-activity radiation source by means of realistic shielding measures that do not impede treatment.

1.2.7 Aim of the study

The aim of Study II is to determine the feasibility of using a gamma and/or X-ray emitting radionuclide for application in IOBT. The various requirements for the radiation output of a potential radionuclide are determined in Chapter 6, both in terms of therapeutic dose delivery and radiation safety. Therapeutic dose deposition is dictated by the use of a source applicator described in the analysis by a mathematical model, and is furthermore dependent on the photon energy and source activity. A low energy gamma and/or X-ray source seems most suitable since the predominant dose deposition range matches well with the prescribed target depth at 1 cm from the source, discussed by Nath et al. (1999), and shielding problems are relatively easy to overcome. In Chapter 7, a selection procedure is derived from the radiation output requirements, which is used to assess the feasibility of iodine-125 for application in IOBT.

1.3 Study III: Design of an X-ray setup for a multiphase flow metering device

1.3.1 Changes in multiphase flow metering techniques

The production of crude oil is often accompanied by large amounts of gas and water. Measurement of the individual oil, water and gas flow rates is required for the purpose of reservoir management and production allocation. Traditionally in oil production, the multiphase flow was separated into its constituent component parts, which allowed straightforward single phase metering techniques to be used. This approach proved to be both practical and effective, although it did involve processing systems like separators which were quite heavy, bulky and expensive.

The disadvantages of using separators were becoming more apparent during the 1980s, when there was a partial shift in oil production from major oil fields to numerous smaller satellite fields. The development of these smaller fields would only become attractive if accompanied by lower expenditures.

1.3.2 Flexible multiphase flow metering

From the situation it was clear that more operationally flexible metering technologies were going to be needed. For existing platforms the prime purpose of this technology would be to improve processing flexibility, and for new field developments the aim would be to completely eliminate the need for costly and bulky platform-based process plants.

To take up these challenges, considerable research has been conducted into so-called multiphase flow metering (hereafter: MPFM) techniques since the early 1980s. In all of these multiphase flow meters the mass or volume flow rates of the oil, water and gas components through pipelines are determined by means of a combination of instantaneous measurements of e.g. velocities and cross-sectional fraction of each component, and complex two-phase flow models. The ultimate aim in multiphase meter technology is to replace the function of the large and expensive separators and/or (sub sea) test lines by a cheap, accurate and maintenance free device which can be used on every single oil well with large processing flexibility for fluctuating flow rates.

There are different measurement principles on which multiphase flow meters are based, discussed by e.g. Hammer et al. (1998). The difference in electrical permittivity between water and oil can be used to determine the amount of water in the liquid component, i.e. the water-cut (hereafter: WC). Together with this technique, electrical conductivity measurements can be used to determine the sum of oil and gas fractions, resulting in a complete determination of the oil, water and gas components.

1.3.3 Dual Energy Gamma-Ray Absorption

The measurement principle of Dual Energy Gamma Ray Absorption (hereafter: DEGRA) can be used to directly yield the oil, water and gas fractions. The total absorption of radiation through the mixture is determined by its composition and is energy dependent. In principle, using a radiation source with two different photon energies yields two equations with the three flow component fractions as unknowns. Because the cross-sectional sum of the oil, water and gas fractions equals one, it is possible to solve the system of equations, as discussed by Van Santen et al. (1995).

1.3.4 The (dis)advantages of the DEGRA technique

There are both advantages and disadvantages attached to the DEGRA technique. On one hand, the technology is based on a single physical principle (photon absorption), it can cover a large range of component fractions with high accuracies, and it forms a reliable, relatively inexpensive and non-intrusive method. On the other hand, if the mixture is not homogeneous (see section 8.4), the method is flow regime dependent which limits the possibilities of techniques that make use of a single beam of radiation. This may be overcome by techniques that apply multiple radiation beams, but these are more complex and more expensive.

The main disadvantage of the technique is that all commercially available gamma or X-ray absorption based multiphase flow meters do, at present, use permanent radioactive sources to generate the gamma or X-rays. Issues like licensing procedures, transportation, on-site safety, disposal and furthermore the social, environmental and emotional barriers which accompany the use of radioactive sources, make their application difficult.

1.3.5 The benefits of an X-ray tube

The application of an X-ray tube can help to overcome some of these problems. It maintains the advantages of the superior photon absorption technique while at the same time eliminating all the hazards, cumbersome and extensive licensing procedures and disposal problems attached to the use of radioactive sources. By applying an X-ray tube (that can be switched off) instead of a radioactive source, the hazards which exist during transportation, installation, maintenance or emergency situations can be eliminated. Furthermore, licensing procedures for X-ray equipment are far more relaxed than those applicable to radioactive sources.

Besides this, an X-ray tube can yield additional profits. By using an X-ray tube instead of a radioactive source, one is no longer restricted to (fixed) radionuclide photon energies but in principle free to choose a number of (tunable) energies. The high X-ray tube radiation intensities compared to photon intensities emitted by radionuclides will result in improved accuracy in the composition analysis and thus form another advantage of the X-ray tube.

1.3.6 Water salinity

Perhaps application of an X-ray tube could also serve to solve a different problem. Although the DEGRA method can be used for the complete range of the multiphase flow component fractions, the salinity of the water component can cause problems. Since salt has a high attenuation coefficient compared to water, a change in the salinity of the water will cause a significant error in the measured water fraction, unless this is compensated for. If three radiation energies are used instead of two, this additional unknown parameter (i.e. the salinity) can in principle be determined. This technique will be referred to as Multiple Energy X-ray Analysis (hereafter: MEXA).

Because of these reasons use of an X-ray tube would be preferable. An MPFM device based on X-ray technology is however not yet available to date.

1.3.7 Aim of the study

The aim of Study III is to design an MPFM device consisting of an X-ray tube instead of a radioactive source. An additional aim is to attain an integrated determination of water salinity. In Chapters 8 through 10 we describe the measurement principles of DEGRA and MEXA, and the study on the optimum design of an X-ray set-up for MPFM.

Study I , Chapters 2 - 5

**Modelling of a $^{188}\text{W}/^{188}\text{Re}$ beta line source for coronary
brachytherapy by means of EGS4 Monte Carlo
simulations**

2 Simulation models of the coronary brachytherapy source

In this chapter we present three different simulation models that were used to determine the dose distribution around a $^{188}\text{W}/^{188}\text{Re}$ coronary brachytherapy source by means of EGS4 Monte Carlo simulations. A paper about this study was published by Clarijs et al. (2000). This research was performed by request of and in cooperation with Nucletron B.V., Veenendaal, The Netherlands.

2.1 Introduction

In Chapter 1 we discussed the background to Study I on the modelling of a $^{188}\text{W}/^{188}\text{Re}$ beta line source (see sections 2.3 and 2.4) for coronary brachytherapy by means of EGS4 Monte Carlo simulations. The $^{188}\text{W}/^{188}\text{Re}$ beta line source proved to be a suitable vascular brachytherapy source for the application of restenosis prevention after PTCA. It was selected on the basis of physical requirements, discussed in detail by Schaart (1995a, 1995b). The first of these two references provides the requirements that a radionuclide should meet for successful application in coronary brachytherapy, while the second one lists a number of potential radionuclides that were selected according to these criteria, which will be treated hereafter.

2.2 Source requirements

2.2.1 Irradiation in the coronary artery

As previously mentioned in Chapter 1, there are indications that a dose of ~ 15 Gy in the vessel wall is required to prevent restenosis successfully. A schematic longitudinal cross-section of a coronary artery is shown in Figure 2.1.

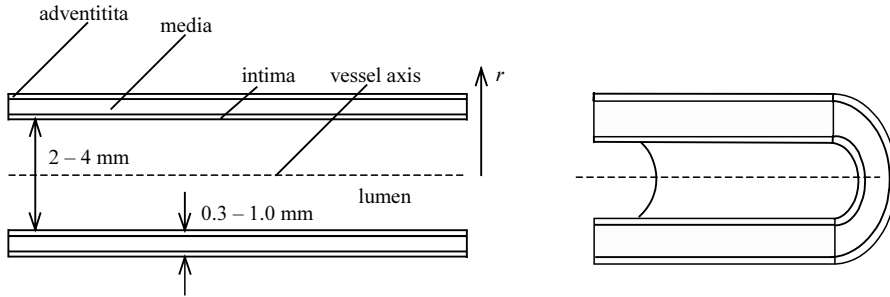


Figure 2.1 Schematic longitudinal cross-section of a coronary artery.

The inner diameter of a coronary artery typically ranges from about 2 mm to about 4 mm. The vessel wall consists of the intima (thickness several hundreds of μm), the media (0.3 – 0.8 mm) and adventitia (thin). The length of the lesion to be treated is usually in the order of several centimeters. The maximum diameter and the length of a long thin beta coronary brachytherapy source should be about 0.6 mm and 40 mm, respectively.

2.2.2 Dose homogeneity

The homogeneity of the dose distribution in the vessel wall, in the direction of the vessel axis, will be referred to as *lateral homogeneity*. The lateral homogeneity in the vessel wall is preferably as high as possible over the length of the lesion to be irradiated. This means that in the prescribed lateral region the isodose rate curves should ideally be parallel to the source axis. In this context, a so-called effective source length L_{eff} is defined in section 3.1.2, which quantifies the lateral dose homogeneity for a given source.

A quantification of the required *radial homogeneity* of the depth-dose distribution into the vessel wall by means of a homogeneity factor (as in section 6.5.3 for transversal homogeneity) is not available, mainly because consensus on the exact target prescription depth is yet to be achieved. It appears that not only the dose received by the intima, but also the dose received by the media is of importance. The relative radial dose distribution in the vessel wall depends on the mean beta energy but not on the source geometry, as long as the mean range of the beta particles is larger than the radius of the outer surface of the vessel wall. As a result, the mean beta energy must be chosen high enough to guarantee an acceptable decrease in dose deposition with increasing radial distance. Assuming that the source can sufficiently be centred in the coronary artery, the range of the beta particles should at least be about 3 mm in water, which implies that the mean beta energy must be higher than about 600 keV.

2.2.3 Source centring

As discussed in section 1.1.9, source centring techniques are essential for the efficacy of radiation treatment for restenosis prevention. In case the source is fixed in a centred balloon

the dose must be delivered within about one minute because the coronary artery is obstructed. The source activity should therefore be very high and uncontrolled irradiation during positioning may become a serious problem. A source with a centring device that allows perfusion of blood during irradiation has the advantage that the source activity can be about one order of magnitude lower as the irradiation time may be longer, up to about 15 minutes.

It was estimated however that beta source activities should be fairly high in the last case, in the order ~ 370 MBq/cm for a source with a mean beta energy of 0.8 MeV, in order to achieve a dose rate of 1 Gy/min at 3 mm radial distance*. As a consequence, this means that the treatment device must form a closed system that shields the source radiation if the source is not inside the body of the patient.

Self-absorption of beta particles in the source material may significantly influence the required source activity, depending on the density of the source material and the beta energy. As an example, calculations by de Vries and Grimbergen (1995) on a 0.4 mm diameter ^{89}Sr beta line source with mass density $\rho = 2.6$ g/cm³ and average beta energy $E_{\text{mean}} = 0.58$ MeV indicate that energy loss due to self-absorption is about 33%. Absorption in the source encapsulation was found to be less influential: a metal layer with a thickness of the order of 10 μm hardly attenuates beta radiation. For example, for a beta line source with $E_{\text{mean}} = 1$ MeV the energy loss in 10 μm of metallic material is estimated to be less than 2%.

2.3 Rationale of $^{188}\text{W}/^{188}\text{Re}$

As mentioned in section 1.1.8, the main rationale for the choice of $^{188}\text{W}/^{188}\text{Re}$ is the fact that the metal tungsten can relatively easily be used in the construction of the source (as explained in section 2.4.1). This was considered an important advantage that outweighs the fact that relatively high neutron fluxes are required to activate the source, as is discussed in section 2.3.2. The emission properties that make $^{188}\text{W}/^{188}\text{Re}$ a suitable radionuclide for a vascular brachytherapy source are first discussed.

2.3.1 The $^{188}\text{W}/^{188}\text{Re}$ electron spectrum

The ^{188}Re radionuclide emits beta radiation with maximum beta energy $E_{\text{max}} = 2.1$ MeV that is intended to deposit the therapeutic dose. The spectral data used are from Lederer et al. (1978) and Sowby et al. (1983). The decay scheme is ^{188}W ($t_{1/2} = 69.4$ days) \rightarrow ^{188}Re ($t_{1/2} = 17$ hours) \rightarrow ^{188}Os (stable). The branching ratio for the $^{188}\text{W} \Rightarrow ^{188}\text{Re}$ transition equals 1. Due to the difference in half-lives for both isotopes the activity of ^{188}W will be equal to the activity of its sole daughter product ^{188}Re , if

* Absorption of beta radiation in the source material (and encapsulation) was neglected in this calculation.

- there is an equilibrium between both isotopes (this is reached in approximately 4 days after neutron activation, see section 2.3.2).
- there is a large number of ^{188}W disintegrations (this is not a restriction in practice).

Taking into account that the ^{188}W and ^{188}Re activities are equal, we define the source activity as the activity of either of these. The maximum beta energy of the mother radionuclide ^{188}W is $E_{\max} = 0.35$ MeV and therefore the maximum energy of the combined beta spectrum from ^{188}W and ^{188}Re is also $E_{\max} = 2.1$ MeV. The sum of the ^{188}W and the ^{188}Re beta spectrum contributions (hereafter: $^{188}\text{W}/^{188}\text{Re}$ beta spectrum) is thus anticipated to be suitable for dose deposition at the target during brachytherapy treatment. The ^{188}W half-life of 69.4 days is sufficiently long for practical applications.

Conversion electrons have been included in the total $^{188}\text{W}/^{188}\text{Re}$ electron spectrum used in the simulations, but only for ^{188}Re ; the 7 keV (0.2%) and 51 keV (0.3%) conversion electrons from ^{188}W were omitted as their contribution to the total dose distribution is negligible. The total $^{188}\text{W}/^{188}\text{Re}$ electron spectrum used in the simulations is shown in Figure 2.2. The average beta energy of the spectrum is $E_{\text{mean}} = 0.78$ MeV.

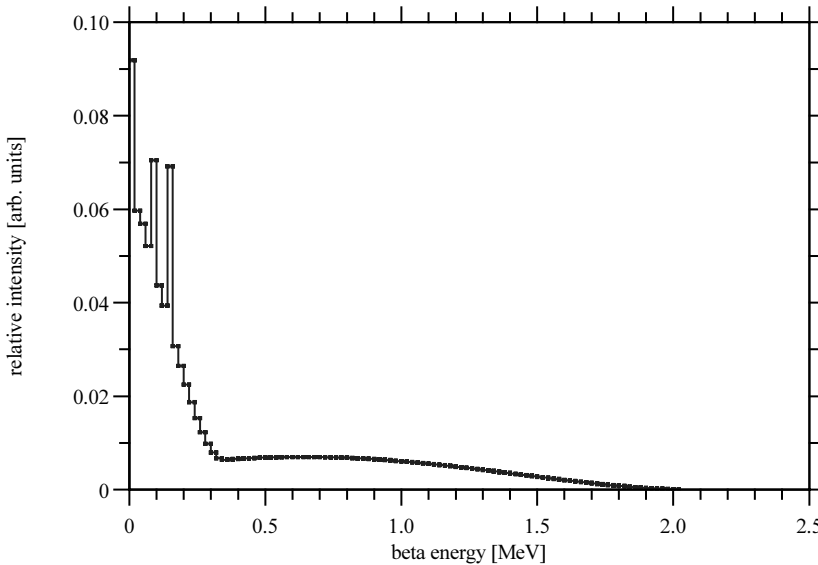


Figure 2.2 The combined $^{188}\text{W}/^{188}\text{Re}$ beta spectrum as used in the simulations, including the rhenium conversion electrons. The EGS4 Monte Carlo code takes care of the normalization of the spectral intensities, which are presented in arbitrary units in this figure.

2.3.2 Neutron activation

Production of $^{188}\text{W}/^{188}\text{Re}$ is via neutron activation of ^{186}W : successive capture of two neutrons by ^{186}W results via $^{187}\text{W}(n,\gamma)$ in production of ^{188}W . It was anticipated that production of $^{188}\text{W}/^{188}\text{Re}$ via direct neutron activation of ^{186}W requires high neutron fluxes, as will now be discussed.

Assuming irradiation of tungsten with naturally occurring isotopic abundances $a(^{186}\text{W}) = 28.6\%$, $a(^{184}\text{W}) = 30.6\%$, $a(^{183}\text{W}) = 14.3\%$, $a(^{182}\text{W}) = 26.5\%$ and $a(^{180}\text{W}) = 0.13\%$ with a thermal neutron flux of $\phi_{th} = 10^{14}$ neutrons $\text{s}^{-1} \text{cm}^{-2}$, the specific saturation activity for ^{188}W is $A_{sat} \sim 60 \text{ GBq cm}^{-3}$, based upon thermal neutron activation cross-sections $\sigma_{th}(^{186}\text{W} \text{ to } ^{187}\text{W}) = 38 \text{ b}$ and $\sigma_{th}(^{187}\text{W} \text{ to } ^{188}\text{W}) = 70 \text{ b}$. The ^{188}W isotope is in radioactive equilibrium with its sole daughter product ^{188}Re approximately 4 days after neutron activation. Data were taken from Lederer et al. (1978), Seelmann-Eggebert et al. (1981) and Wilson et al. (1966).

Since the tungsten volume in the anticipated source design (see section 2.4.1) is $V \sim 3.3 \times 10^{-3} \text{ cm}^3$, the source activity is calculated as $A \sim 200 \text{ MBq}$. The required activity for a beta line source with mean beta energy $E_{mean} = 0.8 \text{ MeV}$ was estimated at $\sim 370 \text{ MBq/cm}$, i.e. $\sim 1.5 \text{ GBq}$ for a 40 mm beta line source in order to achieve a dose deposition of 1 Gy/min at 3 mm radial distance (see section 2.2.3). This means that irradiation with a thermal neutron flux of $\phi_{th} = 10^{14}$ neutrons $\text{s}^{-1} \text{cm}^{-2}$ results in a source activity that is too low by a factor 7.5.

However, when neutron activation is performed with a thermal neutron flux $\phi_{th} = 2 \times 10^{15}$ neutrons $\text{s}^{-1} \text{cm}^{-2}$, as provided by the 85-MW High Flux Isotope Reactor (hereafter: HFIR) at Oak Ridge National Laboratory, Tennessee, USA, the problem of insufficient source activity could be overcome. This is due to the fact that the specific saturation activity A_{sat} for ^{188}W is, in good approximation, proportional to the square of the thermal neutron flux ϕ_{th} ; as a consequence, the maximum source activity could be higher by a factor 400, resulting in $A \sim 80 \text{ GBq}$, which is well above the required value of 1.5 GBq.

These calculations indicate that it is possible to produce the $^{188}\text{W}/^{188}\text{Re}$ beta line source with sufficient source activity. The fact that the metal tungsten can be used in the construction of the source was considered an important advantage that outweighs the fact that relatively high neutron fluxes are required for its production.

During neutron activation of tungsten with naturally occurring isotopic abundances, two other tungsten isotopes are created besides $^{188}\text{W}/^{188}\text{Re}$: ^{185}W and ^{181}W . The isotope ^{185}W (with a half-life $t_{1/2} = 75$ days) emits beta radiation with $E_{max} = 0.43 \text{ MeV}$ and is produced via $^{184}\text{W}(n,\gamma)$. The corresponding thermal neutron cross-section is $\sigma_{th}(^{184}\text{W} \text{ to } ^{185}\text{W}) = 1.8 \text{ b}$. The isotope ^{181}W (with a half-life $t_{1/2} = 121$ days) emits X-rays with energies in the order of 60 keV and is produced via $^{180}\text{W}(n,\gamma)$. The corresponding thermal neutron cross-section is $\sigma_{th}(^{180}\text{W} \text{ to } ^{181}\text{W}) = 10 \text{ b}$. The spectral data and activities of these radionuclides are discussed in section 2.5.

2.4 The source design

2.4.1 Rationale of the tungsten line source

A line source with an active length in the order of several centimeters enables simultaneous irradiation of the complete lesion. Also, due to its geometry, a line source ensures high lateral dose homogeneity (see section 2.2.2). These are important advantages of a line source over shorter, so-called stepping sources that usually necessitate longer irradiation times.

The coronary artery is often strongly curved. This may not only complicate accurate source centring, but also source transporting to the target site by means of afterloading techniques (see section 1.2.4). This implies that, if a line source is to be used, it should be very flexible. A thin tungsten coil meets the above requirements. Such a tungsten coil is easily manufactured and can be wrapped around a flexible central drive wire, thus creating a line source that can be advanced with great manoeuvrability in the coronary artery via a catheter. For these reasons, the prototype coronary brachytherapy source comprises a thin radioactive tungsten coil, enabling simultaneous irradiation of the complete lesion with high lateral homogeneity.

A graphical representation of a section of the prototype beta line source is given in Figure 2.3. The term *line source* is used to denote a cylindrical source with a length L much larger than its outer diameter: $L = 40 \text{ mm} \gg 0.48 \text{ mm}$.

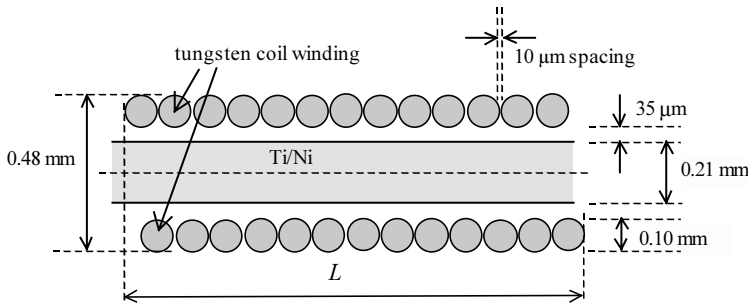


Figure 2.3 Longitudinal cross-section from the prototype beta line source: the tungsten coil is wrapped around a flexible Ti/Ni central driving wire. The outer diameter of the source is 0.48 mm and the length $L = 40 \text{ mm}$.

The source comprises a tungsten coil that is 0.1 mm thick and that is wrapped around a flexible Ti/Ni alloy central drive wire with a diameter of 0.21 mm. The active length of the source $L = 40 \text{ mm}$ and the outer diameter (0.48 mm) meet the requirements from section 2.2.1 and were also chosen on the basis of compatibility with the dimensions of the catheter.

Individual windings of the tungsten coil are spaced by 10 μm due to the wrapping around the central driving wire. In order to prevent possible release of radioactive material, the tungsten coil is sealed with a thin ($< 5 \text{ μm}$) but wear-resistant coating of inactive material.

Although the final composition of the coating was yet to be defined at the time the simulations were performed, its influence on the dose distribution in the medium around the source is negligible (see section 2.2.3) and it was therefore omitted in the simulation models.

The tungsten coil is mounted in between two AISI 316 L stainless steel bushings on the distal ends of the central drive wire. Figure 2.4 shows these bushings and their implementation in the simulation models.

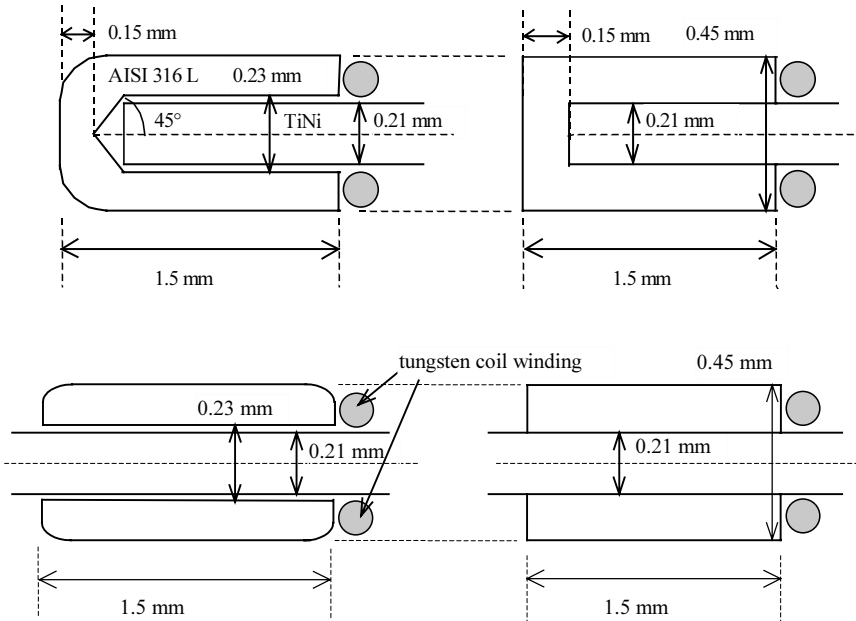


Figure 2.4 Left: The two AISI 316 L stainless steel bushings at both ends of the tungsten coil. Right: Implementation of these bushings in the simulation models.

2.5 Radionuclide spectra

The use of the vascular brachytherapy source is based on the dose deposition by $^{188}\text{W}/^{188}\text{Re}$ beta particles, the spectrum of which was discussed in section 2.3.1. Nuclear decay also involves the emission of photon radiation by $^{188}\text{W}/^{188}\text{Re}$ (gamma and/or X-rays). As discussed in section 2.3.2, the technique of neutron activation of tungsten with natural isotopic abundances leads to a number of different isotopes, each one of them emitting one or more (characteristic) types of radiation. This adds up to a total spectrum that must be fully covered in order to realistically simulate the dose distribution about the source.

Besides $^{188}\text{W}/^{188}\text{Re}$, two other tungsten isotopes are produced: ^{185}W and ^{181}W , and the contributions of these radionuclides to the total dose have been assessed by performing EGS4

simulations for the corresponding radiation spectra (both electrons and photons) and taking into account the corresponding isotope activities. The latter activities were assessed by measurements, performed by de Vries (1997), and were found to be $A(^{188}\text{W}/^{188}\text{Re}) = 204 \pm 8$ (2.8) MBq, $A(^{185}\text{W}) = 1.2 \pm 0.2$ GBq and $A(^{181}\text{W}) = 60 \pm 20$ MBq. We hereby mention the use of the BETASPEC computer program, based upon data from Dillman and von der Lage (1975) and Kocher (1981), for the creation of the beta spectra from the various radionuclides. The gamma and X-ray spectral data are taken from Lederer et al. (1978).

The minimum radiation energy yield from ^{188}Re was taken as a criterion for inclusion of gamma and X-ray spectral lines from the other isotopes: the minimum energy yield from ^{188}Re corresponds to the 845 keV line, $y(i) \times E(i) = 7.2 \times 10^{-5} \times 8.451 \times 10^{-1} = 6.08 \times 10^{-5}$ MeV $\text{Bq}^{-1} \text{s}^{-1}$, with radiations yield $y(i)$ for energies $E(i)$ taken from Lederer et al. (1978). Taking into account the ^{181}W , ^{185}W and $^{188}\text{W}/^{188}\text{Re}$ isotope activities, the gamma and X-ray spectral lines from these radionuclides have been included if the corresponding energy yields in units $[\text{MeV s}^{-1}]$ exceed this value.

Radionuclide activities depend on neutron activation conditions that may vary. The simulations for the dose distribution due to each of the radionuclides were therefore performed separately in order to maintain flexibility in adding the different contributions to the final dose distribution for different activities. Since the EGS4 Monte Carlo code takes care of the normalization of the spectral intensities, the latter are presented in arbitrary units in the next sections.

2.5.1 $^{188}\text{W}/^{188}\text{Re}$ photon spectrum

From the $^{188}\text{W}/^{188}\text{Re}$ radionuclide combination, ^{188}Re is primarily responsible for dose deposition from photons and therefore all its gamma and X-ray lines have been included in the spectra for the EGS4 simulations. In the $^{188}\text{W}/^{188}\text{Re}$ gamma and X-ray spectrum that is depicted in Figure 2.5, 3 gamma lines from ^{188}W have been included based on the criterion of minimum energy yield $y(i) \times E(i)$ from ^{188}Re : those with energies 63.6, 227 and 291 keV.

2.5.2 ^{185}W and ^{181}W spectra

For ^{185}W , with $t_{1/2} = 75$ days, $E_{\max} = 0.43$ MeV and $E_{\text{mean}} = 0.13$ MeV, the beta spectrum is depicted in Figure 2.6.

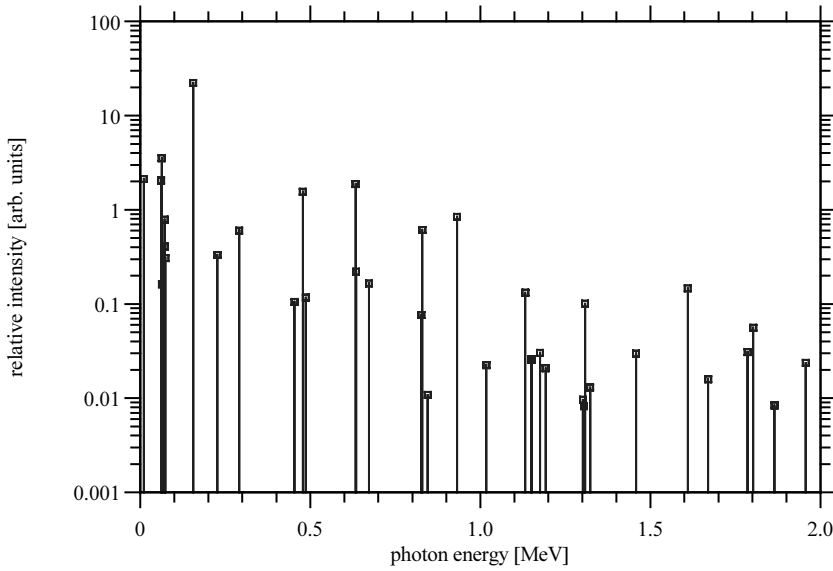


Figure 2.5 The combined $^{188}\text{W}/^{188}\text{Re}$ gamma and X-ray spectrum as used in the simulations. The EGS4 Monte Carlo code takes care of the normalization of the spectral intensities, which are presented in arbitrary units in this figure.

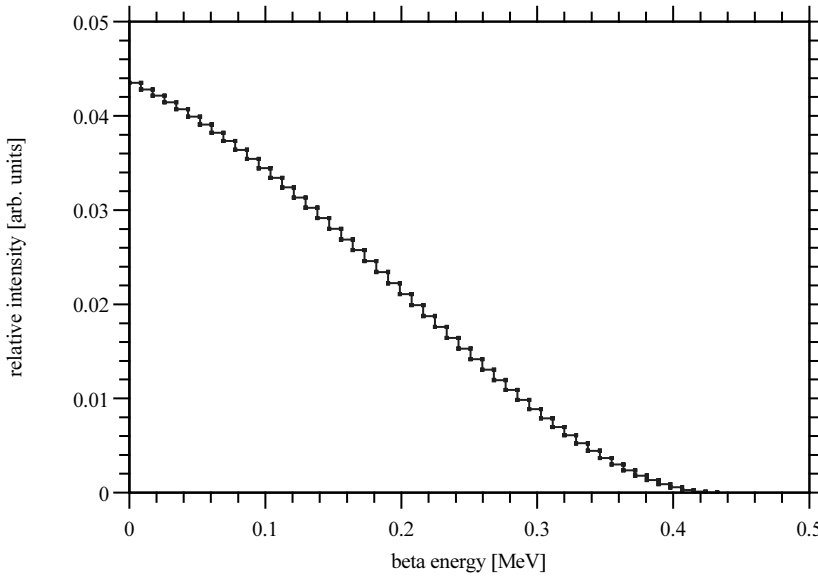


Figure 2.6 The ^{185}W beta spectrum as used in the simulations. The EGS4 Monte Carlo code takes care of the normalization of the spectral intensities, which are presented in arbitrary units in this figure.

Simulation of the charged particles of ^{181}W has not been performed as the expected contribution in dose rate at therapeutically relevant distances is negligible; the decay mode for ^{181}W is electron capture, resulting in a number of conversion electrons and Auger electrons with energies below 140 keV. Considering the fact that the ^{181}W activity is also lower by about a factor 3 than the $^{188}\text{W}/^{188}\text{Re}$ activity, the dose rate contribution at small therapeutic distances within the beta range of ^{181}W can also be neglected.

Taking into account the ^{181}W , ^{185}W and $^{188}\text{W}/^{188}\text{Re}$ isotope activities, the minimum radiation energy yield from ^{188}Re is the criterion for inclusion of gamma and X-ray spectral lines from the other isotopes, as explained above. One gamma (125 keV) and two X-ray lines ($K_{\alpha 2}$: 59.7, $K_{\alpha 1}$: 61.1 keV) from ^{185}W , and 6 X-ray lines from ^{181}W (L_{α} : 8.14, L_{β} : 9.41, $K_{\alpha 2}$: 56.3, $K_{\alpha 1}$: 57.5, $K_{\beta 1}$: 65.2, $K_{\beta 2}$: 67.0 keV) were included in the simulations spectra (not illustrated).

2.6 EGS4 and DOSRZ

As mentioned in Chapter 1, the EGS4 (version 3) computer code has been used to simulate the dose distribution around the $^{188}\text{W}/^{188}\text{Re}$ source. The EGS4 Monte Carlo system has been extensively adopted by the medical physics community. It is a well documented and tested public domain code. Further documentation and details about EGS4 are provided by Nelson and Jenkins (1980), Nelson et al. (1985) and Jenkins et al. (1987). The user code DOSRZ was employed which provides a planar-cylindrical geometry.

Furthermore, the following input values for the radiation transport parameters in the simulation program were used: the fractional energy loss per electron step ESTEPE=0.01, ECUT (including the electron rest mass energy of 0.511 MeV) and PCUT are the cut-off energies of electrons and photons for transport, respectively; ECUT=0.521 MeV, PCUT=0.010 MeV, UE and UP are the upper cut-off energies of electrons and photons for each medium, respectively; UE=2.611 MeV, UP=2.1 MeV, and PRESTA is the electron transport algorithm that is used; default PRESTA input: 0, 0, 0, 0, 0.0*.

The media surrounding the source in the simulations are water, the common substitute in dosimetry for tissue, and PMMA (polymethylmethacrylate), that was used in the measurements (see section 4.1.1). It should be mentioned that the effect of electron binding correction for Compton scattering has been included in the simulations. It is important to realize that the validity of a simulation primarily depends on the quality of two input items: the radiation spectra and the radiation-matter interaction data. While the first were discussed in section 2.5, we will now address the latter.

* We mention and quantify these specific parameters primarily for those EGS4 experts who are interested in performing similar simulations.

The quality of the radiation-matter interaction data used is very decisive for the reliability of a Monte Carlo simulation. It is therefore important to check the data used in EGS4 with standard references. The most well-known and appreciated data in this field are provided by the ICRU (1984). The standard EGS4 routine for generation of radiation-matter interaction data, PEGS4, does not intrinsically guarantee consistency with ICRU data. Duane et al. (1989a, 1989b) describe how this consistency can be achieved for the generation of the radiation-matter interaction data by using special switches. A modified version of PEGS4, called PEGS4NB, was used, taking into account the interference effects due to the fact that the atoms in a substance are bound and cannot be treated with the free atom model, as was first discussed by Leliveld (1996). It was in this way verified that EGS4 radiation-matter interaction data sets are consistent with ICRU Report 37 (1984), within 2% for electron collision and radiative stopping powers and within 1% for photon total attenuation coefficient data.

The simulated geometries involve small dose scoring bins. In the radial direction, these bins compose a grid in the homogeneous water medium with dimensions that range from 0.1 to 0.5 mm, depending on the gradient of the depth-dose curve. In the lateral direction, the dimensions of the dose scoring bins in the water range from 0.1 mm at the source ends to 0.5 mm at the source centre. Dose scoring in the water medium could thus be performed with a spatial resolution up to 100 μm . Even smaller dose scoring bins have been applied within the source itself, in order to realistically simulate its microstructure.

An example is the 35 μm air spacing between the tungsten coil and the Ti/Ni central wire. It has been investigated by Dries (1997) whether these small dimensions influence the reliability of the simulated dose distributions around the source due to e.g. violation of the multiple scattering conditions. Summarizing the conclusions from this study, we can say that calculated dose distributions are not significantly influenced by these small dose calculation volumes.

It is difficult to implement the spiral geometry of the tungsten coil in EGS4, since it is characterized by two orthogonal cylindrical parts: the transverse cross-sections of the central wire and the tungsten coil result in two perpendicular circles. Because of the limited possibilities of implementing such geometries with the available software, we were forced to use different approximations for this geometry. The underlying idea of this approach is the desire to use the most flexible and simple source model without altering the dose distribution around the source. Three different models have been used, which are discussed in the following sections.

2.7 The solid tube model with density correction (DENCOR)

Figure 2.7 presents an approximation of the real source (depicted in Figure 2.3), referred to as the solid tube model with density correction (hereafter: DENCOR model).

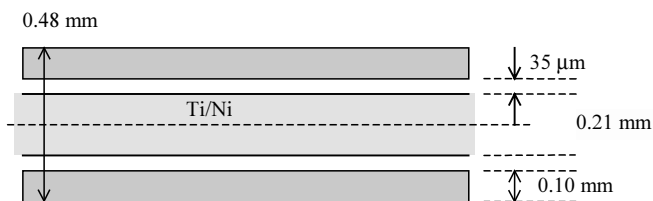


Figure 2.7 Longitudinal cross-section from the geometrical model of the source in the DENCOR approach as implemented in the DOSRZ user code.

The concept for this model is substitution of the tungsten source coil by a cylindrical bulk region of tungsten, enclosed between two radii, thus creating a solid tube. By doing this, we change the real geometry by replacing the individual circular cross-sections of the spiral wire by squares having a width equal to the wire diameter. This leads to a surplus of source material: a factor $4/\pi$ due to the representation of the circle by a square, and, besides this, a factor 1.11 due to the neglect of the clearances between the spiral windings in the real source (10 μm apart, thus equal to 10% of the tungsten wire diameter).

Due to the increase of the amount of radioactive source material there will be an increase of the self-absorption of radiation energy. This is corrected for in the DENCOR model by reducing the mass density of the tungsten tube in such a way that the total mass of the tube equals that of the real tungsten coil. The reduction is from 19.3 g/cm^3 to 13.6 g/cm^3 , a factor $0.9 \cdot \pi/4$ as explained above. The reduction of mass density does not affect the source activity. The latter is not accounted for in the simulations, as these merely calculate the scored dose in units [Gy/hist.], i.e. the dose divided by the total number of simulated particles (one simulated particle = one history) in the assigned source volume.

The rationale for this approach is as follows: EGS4 uses tabulated values for the mass stopping powers $S/\rho = dE/(\rho dx)$ that describe the energy loss by electrons due to collisions with the atomic electrons and radiative losses. The energy loss ΔE along a path with length Δx is then calculated as $(S/\rho) \cdot \rho \cdot \Delta x$. This means that by altering the mass density ρ , we can adjust the energy loss ΔE along a path with length Δx . For instance, we find that for the tungsten with $\rho = 13.6 \text{ g/cm}^3$, an energy loss of 0.023 MeV is related to a $1.962 \cdot 10^{-6} \text{ cm}$ step-size in the simulations, while for $\rho = 19.3 \text{ g/cm}^3$, this energy corresponds to a step-size of $1.383 \cdot 10^{-6} \text{ cm}$. The ratio of these numbers is 1.419 (equal to ratio of the mass densities). This ratio is a constant for all electron energies.

Simulations in the DENCOR geometry with both the real and the reduced tungsten mass density show that reduction of the mass density in the tungsten leads to lower total energy

deposition by the electrons in the tungsten (less self-absorption). However, what turns out to be even more important is that, since the total tungsten mass is also reduced, the net effect is that the total dose in units [J/kg] in the tungsten itself is higher for the reduced tungsten mass density. The reduced self-absorption implies that the electrons enter the water region with a higher average energy, resulting in a higher dose deposition in the surrounding medium.

We conclude that reduction of the tungsten mass density qualitatively compensates the error that we make by enhancing the radioactive source volume, due to the fact that the total radioactive mass remains equal. Quantitative conclusions on this issue are given in section 3.2.

2.8 The solid tube model with diameter correction (DIACOR)

Figure 2.8 shows an approximation referred to as the solid tube model with diameter correction (hereafter: DIACOR model).

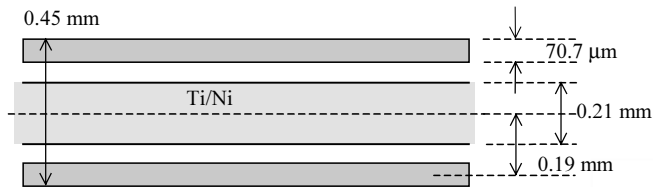


Figure 2.8 Longitudinal cross-section from the geometrical model of the source in the DIACOR approach as implemented in the DOSRZ user code.

The concept for this model is as follows: the tungsten source coil is substituted by a bulk region of tungsten, enclosed within two radii and thus forming a tube, as in the DENCOR approach. The difference with the latter model is that equivalence to the real source geometry is not maintained by adjusting the tungsten mass density but by scaling the inner and outer radius of the tungsten region, thus creating a solid tube region with exactly the same amount of tungsten (mass and volume) as in the real source. As in the DENCOR approach, the ‘moment of inertia’ for the radioactivity around the central axis remains equal to that of the real source (i.e. radial radioactivity center at $r = 0.19$ mm), which was considered crucial for realistic source modelling. This is also taken into account for the third and final source simulation model discussed in the next section.

2.9 The square rings model (SR)

Figure 2.9 shows the source model with implementation of square rings (hereafter: SR model) as an approximation of the individual circular cross-sections of the spiral wire.

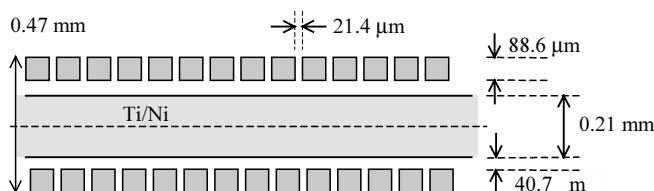


Figure 2.9 Longitudinal cross-section from the geometrical model of the source in the SR approach as implemented in the DOSRZ user code.

The final geometrical model of the source is the most elaborate and detailed one used. It takes account of the microconfiguration of the tungsten coil, and provides the opportunity to study the effects of this microconfiguration on the dose distribution at short distances. Because of the geometry format in the EGS4 user code DOSRZ, the configuration of the tungsten coil had to be adjusted: the circular wire was substituted by a square one having the same cross-sectional area. As can be seen in Figure 2.9, the source material in the simulation model is no longer a single volume, but consists of multiple rings (with square cross-sections) in which EGS4 samples the starting positions of the particles randomly.

The default options in the DOSRZ geometry set-up do not enable this. Therefore, the source code of the program was modified to implement this method of sampling: first, a random sampling of one ring out of an array that contained the same number of rings as the number of individual loops in the real coil. Secondly, a random sampling of the starting coordinates in this ring was performed, thus ensuring a random sampling of the starting coordinates out of the total volume of the tungsten regions.

In the next chapter, results from simulations with the three source models will be compared. The different contributions to the total dose rate, originating from electron and photon radiation emitted by all radionuclides in the source, have been calculated at therapeutically relevant source-target distances.

3 Simulation results for the therapeutic depth-dose distribution in water

Based upon the different geometrical models used to simulate the prototype vascular brachytherapy source, the results will now be presented and compared. This provides insight in the quality of the simulation models, as well as in the contributions to the total dose rate from the different radiation components.

3.1 Representation format

Statistical fluctuations in the dose distribution data have (unless otherwise mentioned) been reduced to a maximum standard deviation of 2% (2 σ) by simulating a therefore required number of particles. Therefore, data points are indicated without error bars. In some figures, depth-dose distribution data are depicted up to a radial distance of 3 mm, whereas in other figures this value is 5 mm. As mentioned by Diamond and Vesely (1998b), the intended target depth is in the range of 1-3 mm for coronary arteries and slightly more distant for peripheral vessels. Therefore, in order not to underestimate the maximum therapeutically relevant radial distance, the latter was assigned the value of 5 mm, whereas we originally used a value of 3 mm for the maximum radial distance. Hence some data are depicted for radial distances up to 3 mm.

Comparisons are made for different source models as described in sections 3.2 and 3.3, with depth-dose distributions from simulations presented in units [Gy/hist.], i.e. the scored dose divided by the total number of simulated particles (one simulated particle = one history). The calculation of the absolute dose rate distributions via the source activity and the radiation yields of the radionuclides is postponed until Chapter 4, after a comparison with experimental data has been made.

3.1.1 Formalisms for endovascular line sources

The simulation data enable specification of the relative dosimetric functions $G(r, \theta)$ and $F(r, \theta)$ as recommended by the AAPM Task Group 60, by Nath et al. (1999). One can effectively describe dose rate variation versus angle using these parameters for line sources with an active length L that is not much larger than the therapeutically relevant distances, as was done by e.g. Soares et al. (1998).

However, for an endovascular beta line source with a relatively long active length L of 40 mm, one may argue that this representation is less suitable, as is discussed by Schaart et al. (2000b) and therefore a different presentation was chosen. In short, this presentation is based on an alternative that is specifically to be used for the description of the dose rate distribution about an endovascular line source. It is believed that this formalism effectively solves some complications associated with the Task Group 60 formalism, which are due both to the choice of coordinate system and to the definition of its individual components.

Thus, results for the dosimetry of the beta line source are presented in a format that is not in full accordance with the dose calculation formalism recommended by the AAPM Task Group 60. Nevertheless, the alternative formalism still preserves the essential concepts of the AAPM approach, namely the decoupling into independent normalized quantities, each of them describing a key aspect of the dose rate distribution. The alternative characterization of the depth-dose distribution is presented in the next section.

3.1.2 Alternative source characterization

For any cylindrically symmetric and linearly uniform beta line source with an active length $L > 2R$, with R the maximum range of the beta particles in the medium surrounding the source, there is a region in which the isodose rate curves are parallel to the source axis, as exemplified in Figure 3.1.

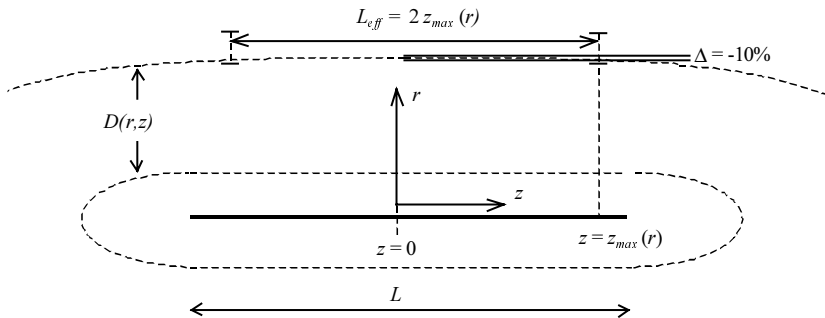


Figure 3.1 Characterization of a cylindrically symmetric beta line source by Cartesian coordinates r and z , the dose deposition $D(r, z)$ and the effective source length L_{eff} . Isodose curves are shown as dashed lines. The curvature of the isodose curves in this figure is for purposes of illustration only.

Within this region, the dose rate distribution around the source can accurately be described by means of a one-dimensional depth-dose distribution in the direction along the transverse bisector at $z = 0$, as a function of radial distance. For this reason the source is characterized using Cartesian coordinates r and z as indicated in Figure 3.1 by means of:

- The depth-dose rate curve $D(r, z=0)$, defined as the dose rate at $z = 0$ as a function of the radial distance r to the source axis.
- The region $|z| < z_{\max}(r)$ in which $D(r, z)$ does not deviate from the depth-dose rate distribution $D(r, z=0)$ by more than a certain percentage, taken as 10%; $z_{\max}(r)$ is then defined by the requirement $|D(r, z=0) - D(r, z_{\max}(r))| / D(r, z=0) = 0.1$. Based upon this region we define an effective source length L_{eff} that is discussed below.
- Specification of the depth-dose rate distribution for r smaller than the therapeutic range and at the ends of the source, i.e. for $|z| > z_{\max}(r)$.

This characterization format allows us to define an effective source length L_{eff} as twice the smallest $z_{\max}(r)$ value over the range of therapeutically relevant radial distances, i.e. for $1 \text{ mm} < r < 5 \text{ mm}$ (see section 4.4.3). Assuming an essentially cylindrical target shape, $D(r, z=0)$ gives sufficient information for dose prescription in case of vascular application, provided that the length of the lesion to be irradiated does not exceed L_{eff} .

3.1.3 Verification of simulated depth-dose distributions in water

As until now depth-dose distributions in water have only been assessed by Monte Carlo simulations, the final characterization of the source according to section 3.1.2 is postponed until Chapter 4. We first present in the next chapter experimental dosimetry data using a polymethylmethacrylate (hereafter: PMMA) phantom, that will be compared with the results for simulated depth-dose distributions in water. Results of the source characterization are then presented in section 4.4.

3.2 Simulation results for $^{188}\text{W}/^{188}\text{Re}$ electrons

The beta rays emitted by $^{188}\text{W}/^{188}\text{Re}$ (cf. Figure 2.2) are anticipated to be most relevant for the therapeutic dose deposition and are therefore considered first. In Figure 3.2 it is shown that all the three source approaches yield the same radial depth-dose distribution curve within 10% over the therapeutically relevant radial region. We therefore conclude that for beta radiation there is an acceptable consistency between the three different models.

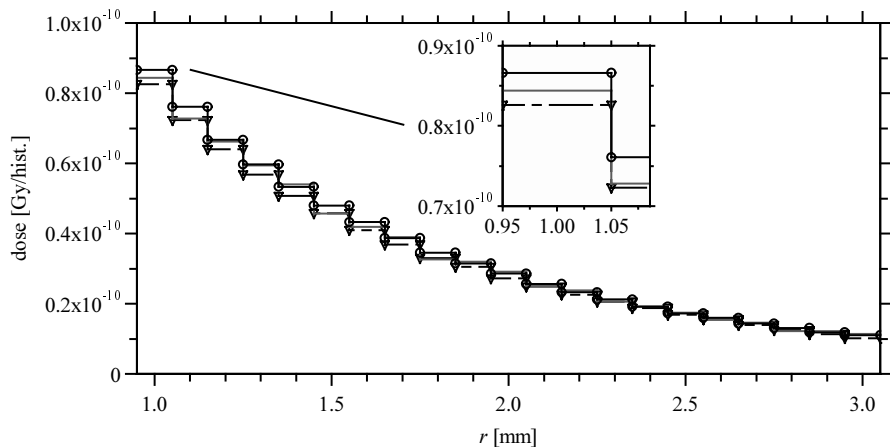


Figure 3.2 Relative radial depth-dose distribution curves in water from the three source approximation models for $^{188}\text{W}/^{188}\text{Re}$ beta radiation: DENCOR model (solid line with open circles), DIACOR model (dashed with triangles) and SR model (solid line without data points).

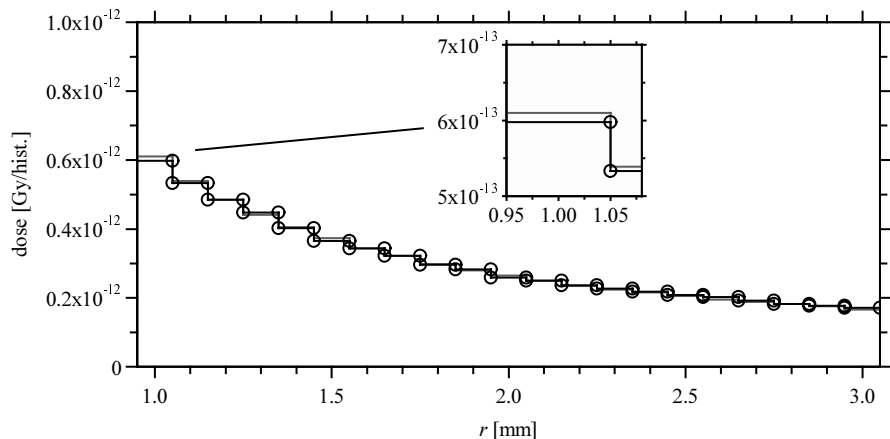


Figure 3.3 Relative radial depth-dose distribution curves in water for the superposed gamma and X-ray spectra from $^{188}\text{W}/^{188}\text{Re}$; DENCOR model (solid with circles) and SR model (solid without data points).

3.3 Simulation results for $^{188}\text{W}/^{188}\text{Re}$ gamma/X-rays

The superposed gamma and X-ray spectra from the ^{188}W and ^{188}Re isotopes (cf. Figure 2.5) were used in simulations with the SR model and the DENCOR model. Figure 3.3 presents the depth-dose distribution curves. They are equal within 5%. The agreement is better than for the beta radiation because the influence of the different source diameters in the three models on the radial photon dose curves is quite small. In the energy range of interest these curves are intrinsically less steep than electron dose curves.

In the therapeutically relevant radial region the gamma and X-ray dose contribution is less than 2% of the beta dose rate (cf. section 3.4), which means that the 5% inconsistency between the different photon depth-dose distribution curves will not cause a significant increase of the uncertainty in the total dose rate.

3.4 Other depth-dose rate contributions

Simulations of the dose deposition from the other two radionuclides in the source, ^{185}W and ^{181}W , for both beta and gamma/X-ray particles, have been performed using the DENCOR simulation model and the spectra that were given in section 2.5.2. Results from these simulations have been summarized in Figure 3.4 and need some further explanation: we show the contribution in depth-dose rate arising from all types of radiation (electrons and photons) from all radionuclides in the source, relative to the depth-dose rate originating from the therapeutically relevant radiation, i.e. $^{188}\text{W}/^{188}\text{Re}$ beta radiation.

This means that corrections for both the radiation yield $y(i)$ (the number of emitted particles per disintegration with an energy indicated by i) of each type of radiation and absolute radionuclide activities have already been taken into account. Radionuclide activities $A(^{188}\text{W}/^{188}\text{Re}) = 204 \text{ MBq}$, $A(^{185}\text{W}) = 1.2 \text{ GBq}$ and $A(^{181}\text{W}) = 60 \text{ MBq}$ are used in this calculation as discussed before in section 2.5. The dose rate contribution of the electrons includes that of absorbed bremsstrahlung photons that are generated as electrons are decelerated in the source material and the surrounding water medium. The simulation of bremsstrahlung photons is discussed in detail in section 9.2.2.

Figure 3.4 shows that, compared to $^{188}\text{W}/^{188}\text{Re}$ beta radiation, the contribution from $^{188}\text{W}/^{188}\text{Re}$ gamma/X-rays is predominant in the therapeutic radial range, and that there are no large variations with r for the different relative contribution curves. The only exception concerns beta radiation from ^{185}W , for which the maximum radial range is about 2 mm; fluctuations in the relative depth-dose rate contribution for $r > 2 \text{ mm}$ are caused by poor statistics since there is only little dose deposition in this region due to bremsstrahlung emitted by ^{185}W beta particles.

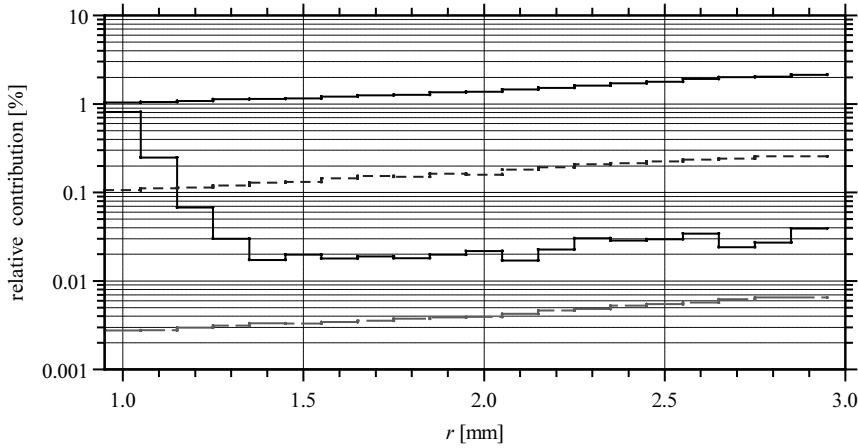


Figure 3.4 Relative contribution in depth-dose arising from both electrons and photons from all radionuclides in the source, compared to the depth-dose rate arising from $^{188}\text{W}/^{188}\text{Re}$ beta radiation. From top to bottom at $r = 2.0$ mm: $^{188}\text{W}/^{188}\text{Re}$ photon radiation (solid), ^{181}W photon radiation (dashed), ^{185}W electron radiation (solid) and ^{185}W photon radiation (dashed).

There is furthermore a relatively high contribution from ^{181}W photon radiation, consisting of 6 X-ray lines with significant radiation yield (as discussed in section 2.5.2), especially compared to the contribution due to photon radiation from ^{185}W , the latter with an activity that is 20 times higher.

Most important, for $r < 3$ mm, depth-dose rate contributions from *any* kind of radiation emitted by the source do not exceed 2% of the dose deposited by $^{188}\text{W}/^{188}\text{Re}$ beta radiation. The contribution from $^{188}\text{W}/^{188}\text{Re}$ gamma/X-rays is $\sim 5\%$ at $r = 5$ mm (and is included in Figures 4.4 and 4.5). This means that, in good approximation, therapeutic dose is only delivered by $^{188}\text{W}/^{188}\text{Re}$ beta particles.

3.5 Use of the source models

Based on the previous sections, we conclude that all three source models are equally good representations of the source. No physical processes are violated in the DENCOR model and, as far as the depth-dose distribution is concerned, adjustment of source material mass density can be used to correct a surplus of source material. For most of the simulation runs, the DENCOR model was used since it was the most practical model. A big advantage of the DENCOR model is that whenever a feature of the endovascular brachytherapy source is changed, this model provides a quick, flexible means of inspecting the influence on the depth-dose distribution. For example, simulations with the DENCOR model were performed in order to study the influence of a thinner central wire, around which the tungsten coil is

wrapped. Such a modification can quite easily be implemented in the DENCOR model, whereas use of the SR model would take considerably more effort.

On the other hand, the influence of the microstructure of the source on dose deposition in the small r range is best studied using the SR model as this is the one model with a detailed distribution of radioactive material, closely resembling the distribution of radioactivity in the real source (see section 2.9).

The DIACOR model is considered to represent a less elegant compensation for the surplus of source material, since the inner and outer diameter of the real source have been altered. We will therefore no longer use this source model - in spite of its results that are consistent with those of the other two models.

4 Comparison with experimental data

In this chapter results are presented from measurements performed by Winkelman and Bos (1997) on a polymethylmethacrylate (hereafter: PMMA) phantom, which are compared to the simulated depth-dose distributions about the $^{188}\text{W}/^{188}\text{Re}$ coronary brachytherapy source; the degree of agreement between experimental and simulated data for PMMA determines the validity of the simulated radial depth-dose rate distribution curves. Final results for the radial depth-dose distribution in water are presented in section 4.4, after this agreement has been quantified.

The comparison between experimental and simulated data in this chapter primarily concerns the therapeutic depth-dose distribution, while a comparison for radiation safety is discussed in the next chapter about results for air kerma rates from the source under therapeutic conditions, assessed by simulation, analytical calculation and experiment.

4.1 Phantom measurements with TLDs

The technique of an accurate measurement of a radial depth-dose distribution about a beta line source is described in great detail by Schaart et al. (2000a) and Winkelman and Bos (1997). Here we concentrate on summarizing the experimental conditions and, more important, on the results.

4.1.1 The PMMA phantom

Dose measurements were performed using a cylindrical PMMA phantom with a diameter of 45 mm and a length of 130 mm, see Figure 4.1. The line source was positioned along the central axis in a capillary hole with a diameter of 0.50 mm. The phantom was constructed such that it could easily be fastened to the source container. The line source (40 mm in length) can be moved (remotely controlled) from the container into the phantom. Perpendicular to the axis of the phantom (in the middle of the positioned line source) a hole of 8.0 mm diameter was milled towards the capillary.

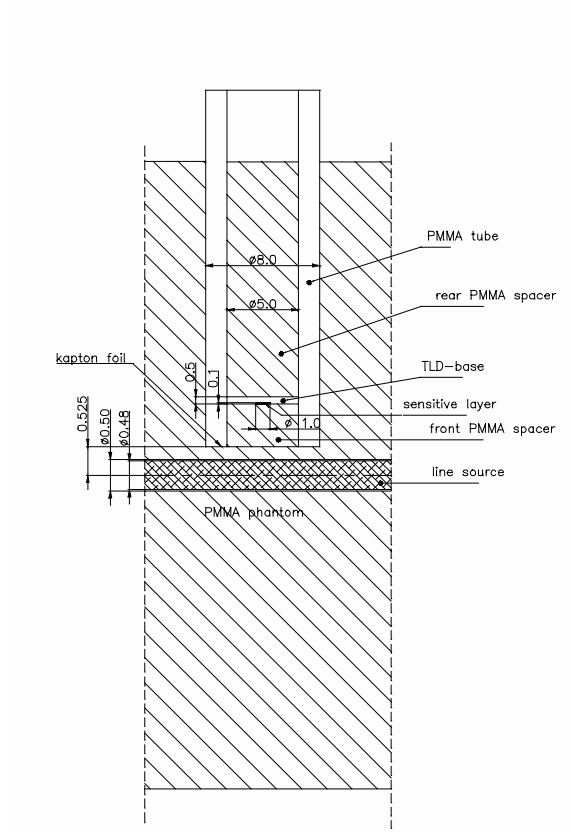


Figure 4.1 Cylindrical PMMA phantom used in the measurements of the radial depth-dose distribution about the $^{188}\text{W}/^{188}\text{Re}$ beta line source. Dimensions are given in units [mm].

Inside this hole a PMMA tube (outer diameter 8 mm, inner diameter 5.0 mm) closed with a 25 μm kapton foil was placed. In the tube, in turn, a thermoluminescent detector (hereafter: TLD) positioned and held in place by PMMA spacers can be placed. The minimum distance between the axis of the phantom and the sensitive layer of the TLD is 0.525 mm. Using spacers of different lengths placed in front of and behind the TLD, dose can be measured at any position between 0.525 mm and 7.5 mm with a spatial resolution of (0.25 ± 0.02) mm.

4.1.2 The thermoluminescent detector (TLD)

For these measurements special purpose ultra thin LiF:Mg,Cu,P (MCP) TLDs, see Figure 4.2, were developed and produced by the Institute of Nuclear Physics in Krakow, Poland, as discussed by Bilski et al. (1995).

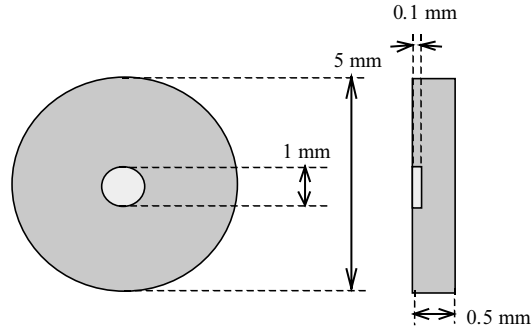


Figure 4.2 The LiF:Mg,Cu,P (MCP) thermoluminescent detector used in the measurements of the radial depth-dose distribution about the $^{188}\text{W}/^{188}\text{Re}$ beta line source.

The sensitive part is embedded in a TL-insensitive base material of diameter (4.63 ± 0.050) mm and nominal thickness 0.5 mm consisting of LiF(AR grade) mixed with a small amount of graphite (3% weight fraction). The TL-sensitive layer of MCP material is centred in the base material and has dimensions of 1.0 mm in diameter and thickness of only (100 ± 10) μm . From a batch of 60 MCP samples, 20 were selected with a thickness of (0.50 ± 0.01) mm. The mass density of this MCP material was determined by weighing and found to be $\rho = (2.21 \pm 0.06)$ g/cm^3 which is considerably lower than the value for crystalline LiF ($2.64 \text{ g}/\text{cm}^3$).

Calibration of the TLDs was performed at the Dutch Radiation Standard Laboratory (Nederlands Meetinstituut, NMI), using a ^{90}Sr - ^{90}Y Buchler secondary standard beta source calibrated by the Physikalisch-Technische Bundesanstalt (PTB). The TLDs were placed in 0.50 mm deep holes (\varnothing 5.0 mm) in a 20 mm thick PMMA block and covered with a 25 μm kapton foil to simulate the *in situ* situation. The variation in dose response of the 20 samples selected on thickness was found to be 15% (1 σ). Therefore, all samples were calibrated individually. The linearity in dose response was checked with a calibrated ^{60}Co source. The TL response was found to be linear up to approximately 40 Gy. TLDs show sublinear behaviour for higher dose values. Before each irradiation the TLDs were annealed at 240 $^{\circ}\text{C}$ for 10 minutes and cooled down to room temperature quickly. The TLDs show good reproducibility ($\sigma < 3\%$).

Measurements were performed on the prototype $^{188}\text{W}/^{188}\text{Re}$ line source that was discussed in section 2.4. Irradiation times varied between 2 min and 120 min depending on the distance between source and TLD. At each distance the measurement was repeated once and at two distances (0.577 mm and 1.587 mm) twice. The measurement uncertainty in the dose rate is 8% (2σ) in the range of radial distances between 0.8 and 5.1 mm.

4.2 Corrections to experimental data

In order to make a realistic comparison between simulated and experimental data, the latter need to be corrected for two effects that influence the recorded dose in the TLDs.

4.2.1 Influence of TLD size

It is desirable to quantify dose deposition at or in a point in the medium surrounding the source, but the finite dimensions of the sensitive layer of the TLD hinder this. The difference between point-dose and measured volume averaged dose (in the sensitive layer of the TLD) that is obtained by measurements becomes more significant when the TLD is positioned close to the source. This is clarified in Figure 4.3, depicting a side-view on scale of a TLD positioned at 1 mm (minimum therapeutically relevant distance) from the $^{188}\text{W}/^{188}\text{Re}$ beta line source, with the bold arrow indicating the location where the point-dose should ideally be measured.

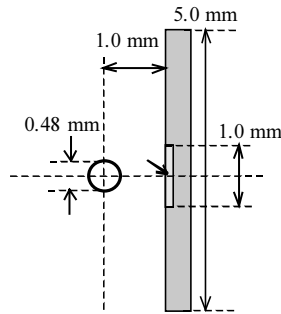


Figure 4.3 Side-view of a TLD positioned at 1 mm (minimum therapeutically relevant distance) from the $^{188}\text{W}/^{188}\text{Re}$ beta line source (perpendicular to drawing plane). The bold arrow indicates the location where the point-dose should ideally be measured.

TLD readings were corrected for finite dimensions of the TLD by means of analytical calculations, as discussed by Winkelman and Bos (1997). The difference between the volume averaged dose recorded in the sensitive layer of the TLD and the ideal point-dose was determined by integrating the different dose contributions from line source volume elements to detector volume elements. Correction factors of 1.2 and 1.4 for measured depth-dose at a minimum distance of 0.58 mm were assessed for zero attenuation (approaching gamma attenuation in PMMA) and $\mu = 0.369 \text{ mm}^{-1}$ (average beta attenuation in PMMA) respectively. Corrections drop below 1% however for distances larger than 5 mm ($\mu = 0$) and 3 mm ($\mu = 0.369 \text{ mm}^{-1}$) respectively.

4.2.2 Influence of TLD insensitive base

The TLD contains an insensitive LiF base that surrounds the sensitive layer on one of its two sides (see section 4.1.2). If electron backscattering in LiF and PMMA are different, there will

be an influence on the dose deposition in the sensitive layer. We therefore simulated a geometry in which a single TLD is placed in a bulk medium of PMMA material at a short (0.5 mm), an intermediate (3.5 mm) and a large (5 mm) distance from a $^{188}\text{W}/^{188}\text{Re}$ beta source. Since, using the DOSRZ program (see section 2.6), the $^{188}\text{W}/^{188}\text{Re}$ beta line source could not be included in this geometry, both a $^{188}\text{W}/^{188}\text{Re}$ point source and an isotropic disc source (100 μm thickness, 10 mm diameter) were simulated and compared in order to take into account the effect of source geometry. These simulations were then repeated with the insensitive LiF base from the TLD replaced by PMMA, i.e. simulating an 'ideal' TLD with its sensitive part embedded in a uniform PMMA medium.

Results show that there is indeed higher electron backscattering from the insensitive base of the TLD samples than from PMMA, leading to higher TLD readings. The difference increases with radial distance, however it is not very large, about 3% for 3.5 mm and 5% for 5 mm source-to-TLD distance, but will become more predominant for distances > 5 mm (i.e. beyond the therapeutically relevant radial range, see section 4.4.3), where beta particles have lost a larger fraction of their initial energy and backscattering becomes more important.

4.3 Comparison between experiment and simulation for PMMA

The mean depth-dose rate distribution values from measurements (corrected for the finite dimensions of the TLD) are shown in Figure 4.4, together with the depth-dose rate distribution $\dot{D}(r, z=0)$ from simulations, comprising beta and gamma dose deposition from the $^{188}\text{W}/^{188}\text{Re}$ source, with $z = 0$ mm at the source centre (the source is positioned between $z = -20$ and $z = +20$ mm).

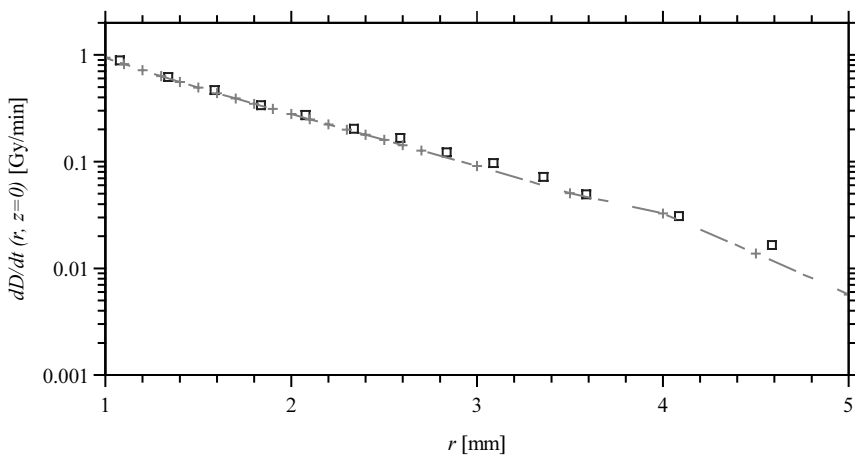


Figure 4.4 Depth-dose rate distribution curves in the direction along the transverse bisector at $z = 0$, as a function of radial distance, for a 204 MBq $^{188}\text{W}/^{188}\text{Re}$ line source (40 mm) in PMMA assessed by simulations (dashed line) and measurements (square points).

Electron and photon dose contributions from ^{185}W and ^{181}W have been ignored for reasons mentioned in section 3.4. The depth-dose rate value at $z = 0$ mm is approximated in the simulations by the average value scored in a z -bin between $z = -2.5$ mm and $z = +2.5$ mm.

Measurements yield $\dot{D}(r_0, z=0) = 0.292 \pm 0.018$ Gy/min for a 204 ± 8 (2σ) MBq $^{188}\text{W}/^{188}\text{Re}$ source in PMMA, with $r_0 = 2$ mm, in agreement with simulations predicting $\dot{D}(r_0, z=0) = 0.280 \pm 0.011$ (2σ) Gy/min. It should be noted that source activities used in the measurements were much lower than typical values for a standard therapeutic source (cf. section 4.4.2). The difference between $\dot{D}(r, z=0)$ curves from measurements and simulations is less than 15%, except for $r > 4$ mm, where measurement values are significantly higher than those of simulations.

Higher experimental values for dose deposition in the radial range $r > 4$ mm may be due to differences between electron backscattering from the insensitive LiF base from the TLD and PMMA, as was discussed in section 4.2.2. This only accounts however for part of the discrepancy between simulations and measurements. Another explanation for higher experimental values might be the overresponse of the TLD at low photon energies, since for the larger radial distances the photon component (i.e. dose deposition from gamma and X-radiation) takes up a higher fraction of the deposited dose and photo-electric absorption is stronger in the LiF than in PMMA due to the higher effective atomic number Z_{eff} ; as discussed by Attix (1986), the effective atomic number Z_{eff} for the photo-electric effect is $Z_{eff} = 8.31$ for LiF and $Z_{eff} = 6.56$ for PMMA.

A more elaborate discussion on the issue of the differences between $\dot{D}(r, z=0)$ from measurements and simulations is given by Schaart et al. (2000a). It is concluded that there is a reasonably good agreement between measurements and simulations for the PMMA medium for $r < 4$ mm. Based on this validation of EGS4 simulations, final results for therapeutic depth-dose rate distribution in water will now be presented.

4.4 Final results for the therapeutic depth-dose rate distribution in water

Final results for the radial depth-dose distribution in water are presented in the characterization format presented in section 3.1.2.

4.4.1 The therapeutic depth-dose rate distribution

The therapeutic depth-dose rate distribution curve for a $^{188}\text{W}/^{188}\text{Re}$ line source with activity of 204 ± 8 (2σ) MBq in a water medium is depicted in Figure 4.5 and tabulated in Table 4.1. Simulations predict $\dot{D}(r_0, z=0) = 0.313 \pm 0.012$ Gy/min for the dose rate at the reference value $r_0 = 2$ mm, as defined by Nath et al. (1999).

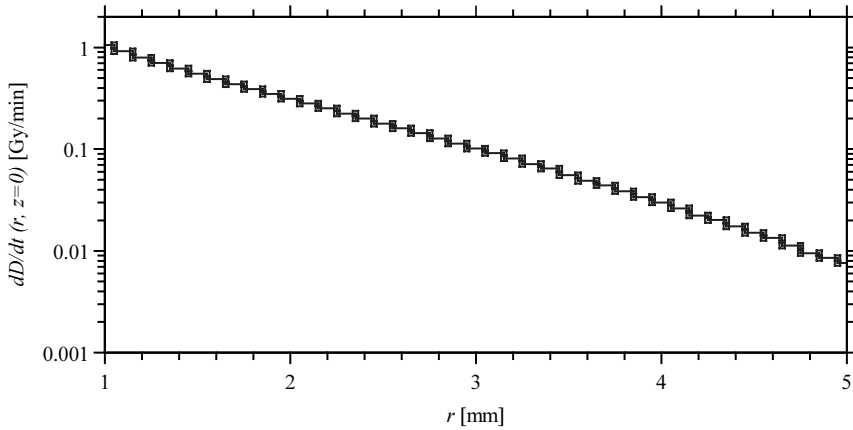


Figure 4.5 Simulated therapeutic depth-dose rate distribution curve in the direction along the transverse bisector at $z = 0$, as a function of radial distance, for a 204 MBq $^{188}\text{W}/^{188}\text{Re}$ line source (40 mm) in water.

Table 4.1 Simulated therapeutic depth-dose rate distribution $\dot{D}(r, z=0)$ for a 204 MBq $^{188}\text{W}/^{188}\text{Re}$ line source (40 mm) in water.

r [mm]	$\dot{D}(r, z=0)$ [Gy/min]
1.0	1.056
1.5	0.552
2.0	0.313
2.5	0.177
3.0	0.102
3.5	0.055
4.0	0.030
4.5	0.015
5.0	0.008

4.4.2 Source activity for therapy

Schaart (1995a) estimated a required value of ~ 370 MBq/cm for a source with a mean beta energy of 0.8 MeV in order to achieve a dose rate of 1 Gy/min at 3 mm radial distance, neglecting beta absorption in the source material and encapsulation. From Table 4.1, a required value of ~ 500 MBq/cm is derived in order to achieve a dose rate of 1 Gy/min at 3 mm radial distance, i.e. 2.0 GBq for a 40 mm long source. Based upon results from a study on different source diameters, Clarijs (1996) predicts 38% beta energy self-absorption in a 100 μm thick $^{188}\text{W}/^{188}\text{Re}$ cylindrical line source. If we correct the rough estimate from Schaart (1995a) using this result, a value of 511 MBq/cm is found, in good agreement with EGS4 results. These simulations also indicate that a typical $^{188}\text{W}/^{188}\text{Re}$ source activity for therapeutic application is about a factor of ten higher than the source activity used in the measurements (204 MBq), assuming a therapeutic treatment time of 15 minutes.

4.4.3 Effective source length L_{eff} based upon $z_{\text{max}}(r)$

An alternative graphical representation of the therapeutic depth-dose distribution is depicted in Figure 4.6, showing isodose rate curves for a 204 MBq $^{188}\text{W}/^{188}\text{Re}$ line source in water.

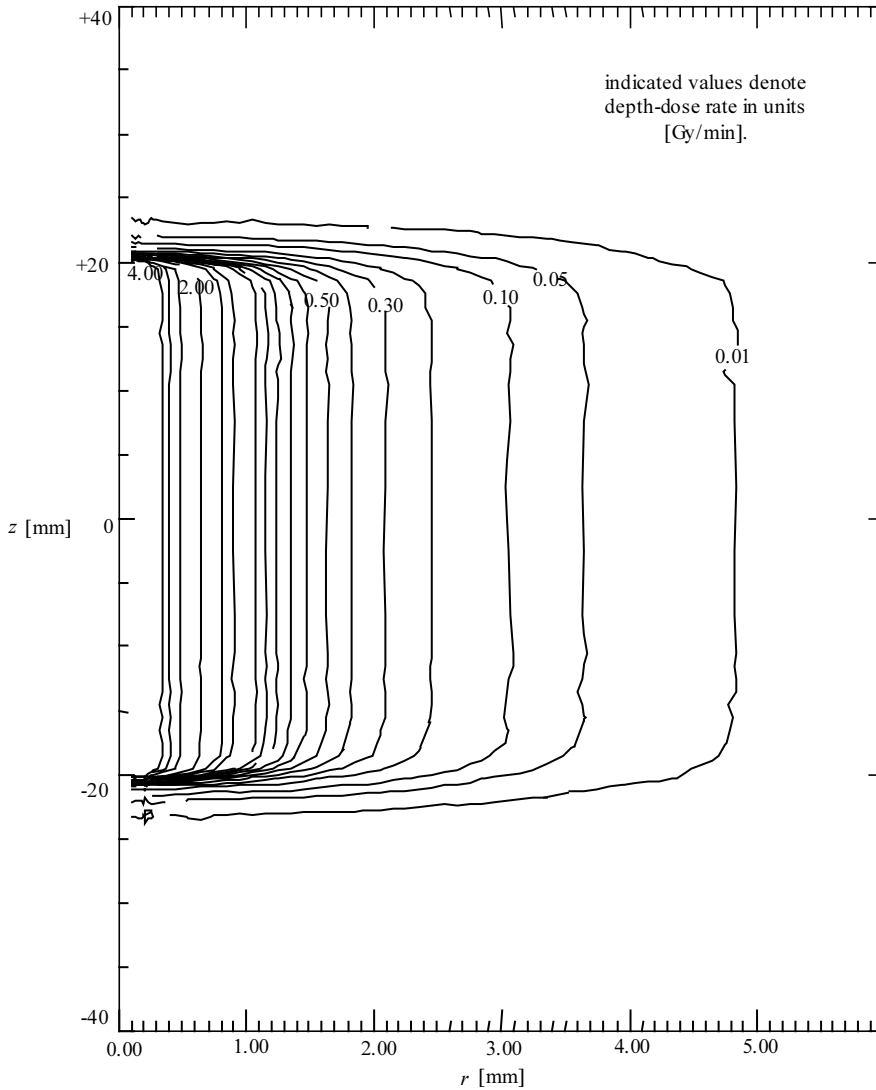


Figure 4.6 Isodose rate curves for a 204 MBq $^{188}\text{W}/^{188}\text{Re}$ line source with indicated depth-dose rate values in units [Gy/min]. The source is positioned between $z = -20$ and $z = +20$ mm in vertical direction; the horizontal axis represents the radial distance r to the source centre.

Figure 4.7 shows the length $2 \times z_{max}(r)$ for which the depth-dose rate distribution $\dot{D}(r, z)$ is almost independent of z for $|z| < z_{max}$, i.e. constant within 10%, for radial distances $1 \text{ mm} < r < 5 \text{ mm}$. The effective source length L_{eff} , defined as twice the smallest $z_{max}(r)$ value in the range of therapeutically relevant radial distances, is equal to 2.95 cm, if one defines the therapeutically relevant radial range as $1 \text{ mm} < r < 5 \text{ mm}$.

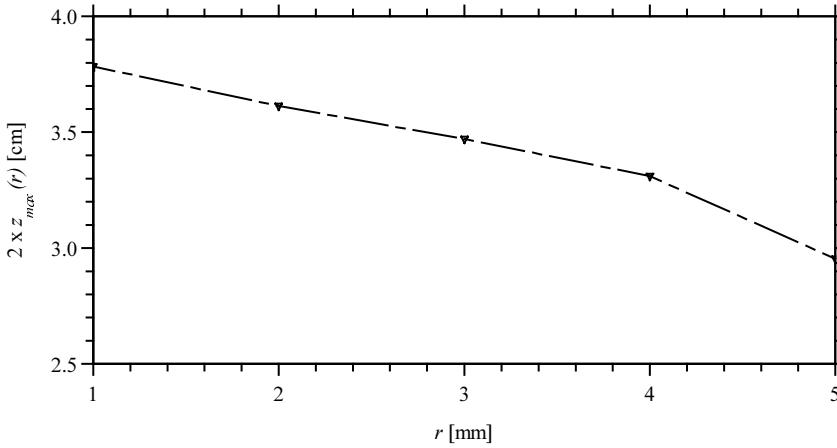


Figure 4.7 $2 \times z_{max}(r)$ for corresponding therapeutically relevant radial distances.

Note that the less restrictive requirement stating that $\dot{D}(r, z)$ must be constant within 10% at $r = 2 \text{ mm}$, as recommended by Nath et al. (1999), would lead to an effective source length of 3.61 cm. These examples clearly show the necessity of determining the true therapeutically relevant radial range, or in other words, the depth of biological target to be irradiated.

4.4.4 Depth-dose distribution for small r and at source ends

From Figure 4.8 it can be seen that ‘wiggles’ are visible in the depth-dose distribution at small r , as was assessed from simulations with the SR model for the combined $^{188}\text{W}/^{188}\text{Re}$ beta spectrum. The source is positioned between $z = -20$ and $z = +20 \text{ mm}$.

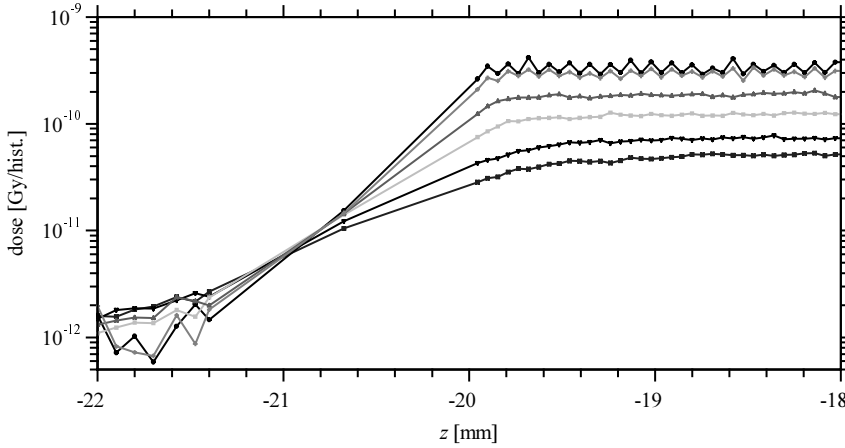


Figure 4.8 Depth-dose distribution curves for small r and at source ends for the SR source model and $^{188}\text{W}/^{188}\text{Re}$ beta radiation. In the flat part of the curves, from top to bottom: $r = 0.225, 0.25, 0.35, 0.45, 0.65$ and 0.85 mm. The source is positioned between $z = -20$ and $z = +20$ mm.

These wiggles occur for radial distances up to 0.35 mm. From the periodicity in the peak-to-peak distance of $110\text{ }\mu\text{m}$ it is concluded that those wiggles are correlated to the microstructure of the source (see Figure 2.9). Depth-dose distribution data for radial distances higher than 0.35 mm do not show wiggles that can be correlated to the tungsten radioactivity distribution. Thus, effects from the microstructure of the source do not extend into the therapeutically relevant region $1 < r < 5$ mm, which means that the dose homogeneity in the target is not disturbed. Figure 4.8 shows that the depth-dose distribution curves cross each other beyond the edges of the source. The rapid decline of the depth-dose distributions at the source ends is mainly due to self-absorption of beta particles in the source material and is more pronounced for smaller r ; the dose deposition in this region mainly originates from beta particles that, on average, travel in the direction of the source axis, and as a consequence many of them will be absorbed (not only in the source material, but also in the bushings mounted to the source ends). The effect does not play a part in the therapeutically relevant radial region.

4.4.5 Conclusions for therapeutic depth-dose rate distribution in water

The absolute dose rate distribution about the prototype $^{188}\text{W}/^{188}\text{Re}$ beta line source for coronary brachytherapy has been quantified by means of EGS4 Monte Carlo simulations, which was the principal aim of Study I. From the dose rate distribution over the full radial range up to the maximum possible target depth in the vessel wall, a source activity of 2.0 GBq for a 40 mm long source is derived in order to achieve a required dose rate of 1 Gy/min at 3 mm radial distance. Calculations in section 2.3.2 on neutron activation indicate that it is possible to produce the $^{188}\text{W}/^{188}\text{Re}$ beta line source with sufficient source activity.

The effective source length, defined in section 3.1.2, is $L_{\text{eff}} = 2.95\text{ cm}$ for the 40 mm $^{188}\text{W}/^{188}\text{Re}$ beta line source and quantifies the homogeneity of the dose distribution in the vessel wall in the direction along the lesion.

Radiation safety during therapy

In this chapter, results are presented from a study on the radiation safety for the $^{188}\text{W}/^{188}\text{Re}$ coronary brachytherapy source. The radiation safety is determined by quantification of the air kerma rate that members of the medical staff are exposed to during treatment. This yields an upper limit for the total effective dose as is discussed in section 5.1.3. The air kerma rates have been assessed by EGS4 Monte Carlo simulations, analytical calculations and experiments. Unless otherwise mentioned, air kerma rates correspond to radionuclide activities $A(^{188}\text{W}/^{188}\text{Re}) = 204 \text{ MBq}$, $A(^{185}\text{W}) = 1.2 \text{ GBq}$ and $A(^{181}\text{W}) = 60 \text{ MBq}$, as mentioned in section 2.5.

5.1 Dose received by patient and medical staff

5.1.1 Dose received by patient

Besides the desired therapeutic dose in the vessel wall, the regions adjacent to the treated coronary artery, located at the outer surface of the heart, receive a dose due to the emitted beta radiation. The importance of these locally high doses should be evaluated with respect to early effects. Also, long term effects and possibly dangerous late complications due to the high dose in the target volume itself cannot be ignored, as discussed by e.g. Bertrand *et al* (1997) and Diamond and Vesely (1998b). Since we are primarily concerned with radiation safety for members of the medical staff, these issues are beyond the scope of this research.

The patient will receive a photon dose due to bremsstrahlung and additional gamma and X-ray photons emitted by the different radionuclides in the $^{188}\text{W}/^{188}\text{Re}$ source. The patient dose due to this source radiation should be compared with the dose already received due to angiography that is performed during a PTCA procedure. Typical effective doses received by the patient, due to angiography with an X-ray tube during PTCA, are in the order of 10 mSv per treatment, depending on the treatment time. The skin dose at the side of the X-ray tube is usually about 400 mGy per treatment. It appears that the effective dose due to the source will be smaller than the dose due to X-ray angiography during PTCA, if the source meets the requirements for the dose received by the medical staff.

5.1.2 Dose received by medical staff

It is important to mention that when a member of the medical staff is not qualified as a radiological worker, the maximum doses apply as recommended in ICRP Publication 60 (1990) for members of the public. This implies limits of 1 mSv per year for the effective dose and 50 mSv per organ (e.g. skin, eye lens) per year. The effective dose received by a member of the medical staff due to interventional procedures may vary between 2 and 25 μ Sv (depending on treatment time and circumstances) and is in general several times larger than that received by most diagnostic procedures.

A maximum value of about 2 μ Sv per treatment is therefore mentioned by Schaart (1995a) as an acceptable value for the effective dose received by a member of the medical staff during an interventional procedure with the $^{188}\text{W}/^{188}\text{Re}$ source, based on the criterion that this dose should not exceed the dose already received from scattered diagnostic X-rays. This restriction corresponds to a maximum photon emission rate for the source; taking into account the radiation yields for the gamma/X-rays emitted by the different radionuclides in the source, a maximum allowed source activity can be derived. We should also include in this calculation the bremsstrahlung that is emitted by the different radionuclides in the source.

By doing so, the maximum value of 2 μ Sv per treatment is related to the required therapeutic dose of ~ 15 Gy (see section 1.1.4). In this context, about 10 μ Sv at 0.5 m per 15 Gy at a radial distance of 3 mm from a 40 mm long $^{188}\text{W}/^{188}\text{Re}$ source is the value (roughly) estimated by Schaart (1995b) for the total effective dose per treatment for a member of the medical staff. This value is calculated using so-called dose equivalent conversion coefficients for anteroposterior gamma irradiation, which are listed as a function of energy in ICRP Publication 51 (1987). Schaart (1995a) provides more information about these calculations.

5.1.3 Determination of air kerma rates

A detailed calculation on total effective dose during treatment requires information about the specific orientation of the source, patient and member of the medical staff, and furthermore entails the use of weighting coefficients for different radiation types of radiation and organs or tissues, as discussed by McCollough and Schueler (2000).

We will instead restrict ourselves to the determination of the air kerma rate, that yields a conservative estimate for the total effective dose for the following reasons:

- whereas the air kerma is determined at a point (representative for the entrance surface of the medical staff member's body), the effective dose will be lower due to attenuation of photons in the body. Use of e.g. a lead apron provides additional shielding and leads to a further reduction.
- the value of 0.5 m in the calculations applies to the 'worst-case' distance between source and the body of a member of the medical staff and means that the source can be considered a point source. Due to the corresponding $1/r^2$ geometric loss of intensity however, the average distance is larger, resulting in a lower total effective dose.

5.2 Simulation model of the source and water shielding

The photon radiation emitted by the source is shielded by the body of the patient. This shielding depends on the specific orientation of the source, patient and medical staff member during treatment. Following a ‘worst-case’ scenario, a thickness of 2 cm of patient body tissue is the estimated minimum value for the available shielding. In order to assess the air kerma rate, the shielding by the body of the patient has been modelled by simulating the source enclosed in a concentric water cylinder with a thickness of 2 cm, using the DENCOR source model (see section 2.7).

5.2.1 The simulation concept for air kerma

The evaluation of the radiation safety under therapy circumstances is based upon the air kerma rate at a certain distance from the source. The use of air regions as detectors in Monte Carlo simulations is however not very practical, since the low energy absorption in air necessitates an enormous amount of computer time to record sufficient dose deposition.

We therefore used cylindrical water detectors with a cross-sectional area of 1 cm² and afterwards scaled dose deposition in these detectors to air kerma: for photon energies between 100 keV and 10 MeV, the dose deposition in water or tissue is almost numerically equal to the air kerma (dose deposition in water is about 10% higher, as discussed by Bos (1994)) and thus only a relatively small correction is needed to obtain air kerma rates.

The detectors are positioned at radial distances of 10 and 100 cm from the source centre (the medium surrounding the source and concentric water cylinder is air). The influence of the presence of the water detector at 10 cm on the dose deposition in the second detector at 100 cm was checked and the deviation from quadratic geometric decay was found to be small: recorded dose deposition in the detector at 100 cm was (within 1.5%) two decades lower than in the detector at 10 cm.

5.3 Contributions to air kerma rate

The different contributions to the total air kerma rate at a certain distance from the ¹⁸⁸W/¹⁸⁸Re coronary brachytherapy source, shielded by a water layer thickness of 2 cm, have been assessed by simulations and analytical calculations and will now be discussed.

5.3.1 Simulated gamma/X-ray contributions

Simulations have been performed in order to assess air kerma rate contributions due to gamma/X-rays emitted by ¹⁸⁸W/¹⁸⁸Re, ¹⁸⁵W and ¹⁸¹W, using the spectra presented in sections 2.5.1 and 2.5.2. From these simulations we derive values 1.30, 0.0046 and 0.18 µGy/h at 1 m from the source, for air kerma rate contributions due to ¹⁸⁸W/¹⁸⁸Re, ¹⁸⁵W and ¹⁸¹W, respectively.

5.3.2 Simulated bremsstrahlung contributions

The contribution to the air kerma rate due to bremsstrahlung emitted by the source when electrons are decelerated and self-absorbed in the source material and the 2 cm thick water medium surrounding the source, has been assessed by simulations and analytical calculations. The charged particle simulation runs predict contributions of 0.39 and 0.14 $\mu\text{Gy/h}$ at 1 m from the source for $^{188}\text{W}/^{188}\text{Re}$ and ^{185}W , respectively. The air kerma rate originating from emitted charged particles is not only due to creation of bremsstrahlung, but also to an effect that is quantified in the next section.

5.3.3 Simulated fluorescence X-rays contributions

Fluorescence or characteristic X-rays are emitted in the process of radioactive decay of the different radionuclides in the source material, but also after excitation of the atoms in the source material and the surrounding medium. Emission of fluorescence X-rays may take place in the process of either photo-ionization or impact ionization. In the latter process, an inner-shell electron is removed from the atom after collision with an incident charged particle; when the vacancy is filled by an electron from an outer shell, a fluorescence photon is emitted (or an Auger electron, as explained in section 9.1.2). Electron impact ionization results in a fluorescence intensity that is several orders of magnitude higher than generated by photo-ionization, as discussed by Attix (1986).

In EGS4, X-ray fluorescence photons are created in assigned regions in the implemented geometry. In the case of e.g. lead, a 80 keV K-fluorescence photon is placed on the stack, if the collision between the incident and atomic electron involves an energy transfer of more than 88 keV (the K binding energy of lead). This 80 keV photon is not absorbed at the interaction position, but transported in the geometry.

In order to estimate the contribution of fluorescence X-rays to the total air kerma rate, simulations were performed for the $^{188}\text{W}/^{188}\text{Re}$ and the ^{185}W beta spectra, with and without transport of fluorescence X-rays in the source and its surrounding media (water cylinder, air regions and water detectors). Tungsten and rhenium emit K-fluorescence X-rays with energies ~ 60 keV, high enough to give a significant contribution to the air kerma rate; K-fluorescence X-rays generated in water (with energies below 1 keV) and the central source wire materials Ti (~ 5 keV) and Ni (~ 8 keV) suffer strong absorption in the source and surrounding media and do not give a significant contribution.

Besides the air kerma rate contribution from fluorescence radiation generated by $^{188}\text{W}/^{188}\text{Re}$ beta particles, a significant contribution can be expected from fluorescence radiation generated by ^{185}W beta particles. In the ^{185}W beta spectrum, with average beta energy $E_{\text{mean}} = 0.13$ MeV, most of the beta particles have energies in the order of only ~ 100 keV, which results in relatively low tungsten X-ray fluorescence intensities due to impact ionization (as discussed by Attix (1986)). Nevertheless, the high ^{185}W activity leads to a significant contribution.

From recorded dose deposition in the water detectors in the simulations, we derive a 5% and 10% increase in the air kerma rate contribution from ^{185}W and $^{188}\text{W}/^{188}\text{Re}$ beta particles, respectively, due to fluorescence X-rays generated by beta radiation from these radionuclides. Air kerma rates from charged particle runs as quantified in section 5.3.2 for $^{188}\text{W}/^{188}\text{Re}$ and ^{185}W include these contributions.

5.3.4 Verification of simulated air kerma rate for $^{188}\text{W}/^{188}\text{Re}$

Analytical calculations on the air kerma contributions due to gamma/X-rays and bremsstrahlung from $^{188}\text{W}/^{188}\text{Re}$ were performed in order to verify results from simulations.

The bremsstrahlung spectral energy distribution $N(E_i)$ for $^{188}\text{W}/^{188}\text{Re}$ (maximum beta energy $E_{max} = 2.0$ MeV) is divided into ten bins E_i of 0.2 MeV width and is given by Schaart (1995a):

$$N(E_i) = f_i \cdot \frac{E_{rad}}{E_i} \quad (5.1)$$

with f_i (data taken from Weber and Rasmussen (1985)) as the bremsstrahlung photon yield (normalized distribution) in the i -th energy bin E_i , and E_{rad} the average amount of energy converted into bremsstrahlung per beta particle in an absorber with effective atomic number Z_{eff} . E_{rad} is given by

$$E_{rad} = 2 \cdot 10^{-4} \cdot Z_{eff} \cdot E_{max} \cdot E_{mean} \quad (5.2)$$

with $E_{mean} = 0.78$ MeV as the mean beta energy. The product of E_{rad} and f_i gives the amount of energy radiated in the i -th energy bin, per beta particle, as a function of the energy bin E_i . We find an average bremsstrahlung photon energy of 23 keV, assuming that most of the bremsstrahlung is generated in the source material tungsten ($Z = 74$).

The total photon spectrum for $^{188}\text{W}/^{188}\text{Re}$, which is divided into ten bins E_i of 0.2 MeV width, is calculated by adding the bremsstrahlung distribution and the gamma/X-rays spectrum as presented in section 2.5.1. The resulting dose rate $\dot{D}(r)$ at a distance r from the source is then described by

$$\dot{D}(r) = \frac{A}{4\pi r^2} \sum_i y_i \cdot E_i \cdot \left(\frac{\mu_i}{\rho} \right)_{en} \cdot B(E_i, r, d_{abs}) \cdot \exp\left(-\frac{\mu_i}{\rho} \cdot \rho \cdot d_{abs}\right) \quad (5.3)$$

with A as the $^{188}\text{W}/^{188}\text{Re}$ radionuclide activity (204 MBq) and d_{abs} as the absorber thickness (2 cm of water). The attenuation coefficients (μ_i/ρ) and energy absorption coefficients ($(\mu_i/\rho)_{en}$) for energies E_i were taken from Hubbell (1982) for water as this is the medium both for shielding and detection. Build-up factors B_i not only depend on E_i , r and d_{abs} , but moreover on the specific geometry of the source, shielding and detectors (i.e. their relative positions during treatment) which is yet to be determined. Therefore build-up is not included in these calculations. The total photon yield per disintegration (i.e. due to both

bremsstrahlung and gamma/X-rays) for energy bin E_i is given by y_i in the above calculation. After inclusion of the 10% increase due to X-ray fluorescence, we thus find $\dot{D}(r=100\text{ cm}) = 1.71\text{ }\mu\text{Gy/h}$ as the dose rate in the water detector, which converts into an air kerma rate of $1.55\text{ }\mu\text{Gy/h}$.

The air kerma rate value assessed by simulations, with contributions from gamma/X-rays, $1.3\text{ }\mu\text{Gy/h}$ (section 5.3.1), and bremsstrahlung/X-ray fluorescence, $0.39\text{ }\mu\text{Gy/h}$ (section 5.3.2), adds up to $1.7\text{ }\mu\text{Gy/h}$ for a 204 MBq 40 mm long $^{188}\text{W}/^{188}\text{Re}$ source, and is therefore in reasonable agreement ($\sim 10\%$) with the calculated value of $1.55\text{ }\mu\text{Gy/h}$.

In section 4.4.2, we derived a required therapeutic activity value for $^{188}\text{W}/^{188}\text{Re}$ of 2.0 GBq for a 40 mm long source, in order to achieve a dose deposition of 15 Gy at 3 mm radial distance, assuming a therapeutic treatment time of 15 minutes. Based upon the results from simulations for therapeutic source intensity and air kerma rate, we can therefore conclude that (only taking into account $^{188}\text{W}/^{188}\text{Re}$) the air kerma rate is $16.7\text{ }\mu\text{Gy/h}$ at 100 cm from the source centre, for a 40 mm long source with an activity of 2.0 GBq. This is equivalent to $16.7\text{ }\mu\text{Gy}$ at 0.5 m, assuming a therapeutic treatment time of 15 minutes.

About $10\text{ }\mu\text{Sv}$ at 0.5 m per 15 Gy at a radial distance of 3 mm from a 40 mm long unshielded $^{188}\text{W}/^{188}\text{Re}$ source is the value estimated by Schaart (1995b) for the total effective dose per treatment for a member of the medical staff. Since this value is based upon calculations on an ideal line source (no absorption of radiation in the source itself), self-absorption in the source material (see section 4.4.2) must be taken into account before a comparison is made; the value from Schaart therefore converts into $\sim 14\text{ }\mu\text{Sv}$ at 0.5 m per 15 Gy at a radial distance of 3 mm from a 40 mm long $^{188}\text{W}/^{188}\text{Re}$ source.

5.4 Final results for radiation safety during therapy

Before presenting the total air kerma rate from the $^{188}\text{W}/^{188}\text{Re}$ coronary brachytherapy source during therapy, we make a comparison between measured data and results from simulations.

5.4.1 Experimental data

Winkelman and Bos (1997) derived an air kerma rate of $1.8 \pm 0.2\text{ }\mu\text{Gy/h}$ at a distance of 100 cm as the result of measurements on a 122 MBq $^{188}\text{W}/^{188}\text{Re}$ source, shielded by 2.25 cm PMMA (the photon attenuation of which is about equal to that of 2 cm water). Using data from de Vries (1997), the other radionuclide activities at the time of measurement are assessed at $A(^{185}\text{W}) = 1567.8\text{ MBq}$ and $A(^{181}\text{W}) = 29.8\text{ MBq}$.

Using air kerma rates from sections 5.3.1 and 5.3.2, simulations predict a total air kerma rate of $1.34\text{ }\mu\text{Gy/h}$, which is in the same order of magnitude as the measured value. Since the complete experimental set-up was not simulated, this can only be a rough comparison. Winkelman and Bos (1997) discuss that higher experimental values may be due to the lead shielding in the measurement set-up, which gives a contribution to the air kerma rate due to

build-up and Compton backscattering. Another explanation may be the overresponse of the TLD at low photon energies, as was discussed in section 4.3.

5.4.2 Total air kerma rate during therapy

Final results from simulations are given for the required therapeutic source activity for the $^{188}\text{W}/^{188}\text{Re}$ coronary brachytherapy source, i.e. 2.0 GBq for a 40 mm long source, as derived in section 4.4.2. The activity values for the other radionuclides in the source, that correspond to the air kerma rates in Table 5.1, have thus been scaled to $A(^{185}\text{W}) = 11.8 \text{ GBq}$ and $A(^{181}\text{W}) = 588 \text{ MBq}$, using the radionuclide activity ratios from section 2.5.

Table 5.1 Composition of total air kerma rate in units [$\mu\text{Gy/h}$] at 1 m from the source due to charged and uncharged particles from different radionuclides in the source. Source activities: $A(^{188}\text{W}/^{188}\text{Re}) = 2.0 \text{ GBq}$, $A(^{185}\text{W}) = 11.8 \text{ GBq}$ and $A(^{181}\text{W}) = 588 \text{ MBq}$.

$^{188}\text{W}/^{188}\text{Re}$ uncharg. particles	12.75
$^{188}\text{W}/^{188}\text{Re}$ charged. particles	3.82
^{185}W uncharg. particles.	0.045
^{185}W charged particles.	1.38
^{181}W uncharg. particles.	1.76
total	19.8

The total value $19.8 \mu\text{Gy/h}$ at 1 m is numerically equal to the accumulated air kerma at a distance of 0.5 m from the source during a treatment time of 15 minutes. As explained in section 5.1.3, this numerical value can be regarded an upper limit for the total effective dose. The assessed air kerma rate can be used in detailed calculations that require information about the specific positions of the source, patient and medical staff member. These calculations should also include the use of weighting coefficients for different types of radiation and organs or tissues.

When the effective dose has been determined, its value should be compared with the ‘acceptable’ value of $2 \mu\text{Sv}$ per treatment, mentioned in section 5.1.2. Note that this value applies to the effective dose limit as recommended by the ICRP (1990) for members of the public (1 mSv per year). Assuming that the effective dose does not exceed this acceptable value, treatment of 100 patients per year (which seems a reasonable number) would then result in 10% of the annual effective dose limit. If the member of the medical staff is qualified as radiological worker, an effective dose limit of 20 mSv per year applies. The relatively high effective dose to members of the medical staff was already foreseen by Schaart (1995b) and underlines the importance of adequate shielding precautions.

5.4.3 Beta dose rate from unshielded source

Assessment of the radiation safety should include an emergency scenario: any situation in which persons are exposed to an unshielded source. In addition to this, exposure to a high dose rate can also occur during the transfer of the source from the afterloader to the patient; transport takes place through a thin-walled catheter, the radiation shielding of which can be neglected (this leads to a conservative estimate of the resulting air kerma rate).

We therefore performed simulations in order to determine the dose rate at 10 and 100 cm from an unshielded source. This dose is primarily delivered by beta particles and only a negligible contribution is due to uncharged particles. Simulations were therefore performed for $^{188}\text{W}/^{188}\text{Re}$ and ^{185}W beta particles, using the simulation model that was discussed in section 5.2, but this time without any shielding medium surrounding the source. The dose was recorded in the first 1 mm layer of the 1 cm thick detector, centred at a distance of 10 cm from the source, i.e. at an average radial distance of 9.55 cm from the source, and is therefore representative for the entrance dose to e.g. the skin and the eye lens at this distance.

Simulations predict air kerma rates 0.835 mGy h^{-1} per MBq $^{188}\text{W}/^{188}\text{Re}$ and $0.00286 \text{ mGy h}^{-1}$ per MBq ^{185}W at 9.55 cm from the source. Based on source activities $A(^{188}\text{W}/^{188}\text{Re}) = 2.0 \text{ GBq}$ and $A(^{185}\text{W}) = 11.8 \text{ GBq}$, this implies a total air kerma rate of 1.70 Gy/h at 9.55 cm from a therapeutic source. It is therefore very important that, in case of emergency, the source can quickly (e.g. within 1 minute) be transferred into an emergency container. The high air kerma rate also once again illustrates that radiation safety should be guaranteed under all circumstances when operating the $^{188}\text{W}/^{188}\text{Re}$ coronary brachytherapy source.

Study II , Chapters 6 - 7

Feasibility of an intraoperative brachytherapy source

6 Radiation output requirements for an intraoperative brachytherapy source

The research described in Chapters 6 and 7 forms the second study in this thesis on a therapeutic application of radiation. This study was also performed by request of and in cooperation with Nucletron B.V., Veenendaal, the Netherlands. The aim is to answer the question whether development of a low energy gamma and/or X-ray source for intraoperative brachytherapy (hereafter: IOBT) is possible, considering a variety of boundary restrictions and requirements, as reported by Nucletron (1997). These include physical, technical, financial, safety-related and logistic restrictions and requirements.

More specific, in Study II the aim is to determine the radiation output requirements a gamma and/or X-ray emitting source should meet for application in IOBT, both in terms of therapeutic dose delivery and radiation safety.

6.1 Introduction

Intravascular brachytherapy (Study I) and IOBT are different in terms of means of dose delivery (single catheter vs. applicator-based system), target geometry (vessel wall vs. body cavity) and intended target depth ($r < 5$ mm vs. $r = 1$ cm). Taking into account this difference in target depth, the required therapeutic dose rate is comparable: ~15-30 Gy in 15 minutes for intravascular brachytherapy vs. ~10 Gy in 20 minutes for IOBT.

In IOBT the target is located at ~1 cm from the source. A low energy gamma and/or X-ray source is suitable for dose deposition in a tissue-like medium at these short distances from the source. The tissue-like medium that is irradiated during therapy can be replaced by water for purposes of analysis (see section 2.6).

We start this study by assessing the relationship between photon energy E and necessary source activity for an IOBT source, that results in the required dose profile in the target, for a certain range of photon energies. The minimum energy is determined by attenuation of photons in the water region between source and target prescription plane (see section 6.1.1), whereas the upper limit is dictated by possibilities of radiation shielding during therapy.

6.1.1 Requirements for an IOBT source

A number of assumptions and requirements for a potential IOBT source is listed by Nucletron (1997). Among these are the following properties and requirements for therapeutic dose:

- The target is a planar slab of soft tissue with finite area ($< 200 \text{ cm}^2$) and constant thickness ($< 5 \text{ mm}$).
- The source travels along well-defined positions in a plane parallel to the target; the distance between this so-called source plane and the target surface is determined by the dimensions of the source applicator (see section 6.2) and equals 5 mm (see Figure 6.1).
- Target surface and source plane are separated by means of an approximately tissue-equivalent applicator (see section 6.2).
- The anticipated dose prescription is 10 Gy at the target prescription plane (hereafter: prescription plane), located at 1 cm perpendicular to the source plane, i.e. at 5 mm depth in the target.
- Dose to be delivered within 1 minute per 10 cm^2 of target area.
- Homogeneity factor for dose distribution in the target must be < 2 (see sections 6.5.3 and 6.5.4).

These requirements will be illustrated in the next section where we discuss the source applicator.

6.2 Source applicator

The source applicator is described by Nucletron (1996) and is depicted in Figure 6.1. It consists of a two-dimensional array of tissue-equivalent silopren LSR spheres with a diameter of 1 cm, at a pitch of 1 cm, interconnected in a flexible way. The spheres in parallel rows are connected by centred air channels. Closed-end afterloading catheters are first inserted in these channels in order to ensure sterility during treatment. A drive wire with a radioactive source is then transported through the catheter to the preprogrammed source dwell positions (see also section 1.2.4).

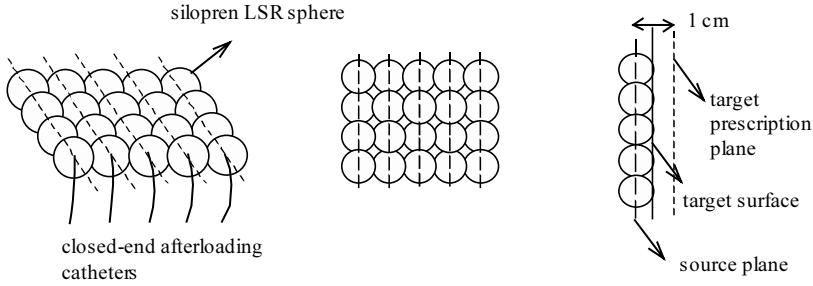


Figure 6.1 Silopren LSR source applicator to be used for IOBT. The drawing on the right describes the therapeutic geometry. The dashed lines in the applicator indicate the centred air channels for insertion of closed-end afterloading catheters, through which a drive wire with a radioactive source is transported.

The applicator serves as a flexible source plane with a well-defined distance to the prescription plane, at 0.5 cm inside the tissue (i.e. at 1 cm from the source plane). The applicator can be cut to the desired dimensions before placing it against the target surface. Therapy is performed after completion of the treatment planning that results in the desired three-dimensional dose distribution, based upon optimization of the dwell times for the source in the applicator.

6.3 Calculational model of source and applicator

In this research the requirements of section 6.1.1 are translated into requirements for radiation output. The analysis was performed with a calculational model (implemented in Mathcad 6.0 software) of the source, applicator and target, that quantifies the dose distribution profiles. Using this model, an outline for the therapeutic analysis has been derived which is presented in section 6.3.3.

6.3.1 The point source grid

The system of source positions, applicator and prescription plane is replaced in the analytical calculations by a regular point source grid in a homogeneous water medium. Although a real source applicator may be cut to any desired shape, we will only consider square (plane) applicators in the calculations. The point source grid is defined by source positions spaced by $d_s = 0.25$ cm in both x - and y -directions (this spacing is the shortest source step-size in the applicator during therapy). The square grid is depicted in Figure 6.2 with $N = 4$, i.e. 4 rows and columns and thus a total of $N^2 = 16$ source positions; the area of the source applicator is given by $A_{app} = ((N-1) d_s)^2$ in units $[\text{cm}^2]$.

The virtual source trajectory in the grid is not exactly equal to the real source trajectory through the applicator: the real source trajectory consists of parallel paths 1 cm apart instead

of a 0.25 cm pitch point source grid. The influence of this difference on the homogeneity in the prescription plane is most noticeable for photons with low energies since these are less penetrative. Calculations however show that there is no significant difference in dose deposition homogeneity in the prescription plane, by comparing the dose distribution from a 1 cm pitch grid with that from a 0.25 cm pitch grid: only a 2% decrease in dose deposition in the prescription plane between two source positions 1 cm apart for 15 keV photons, and less than 1% for 20 keV. For higher photon energies there is no significant difference in prescription plane homogeneity at all due to the higher penetrative range.

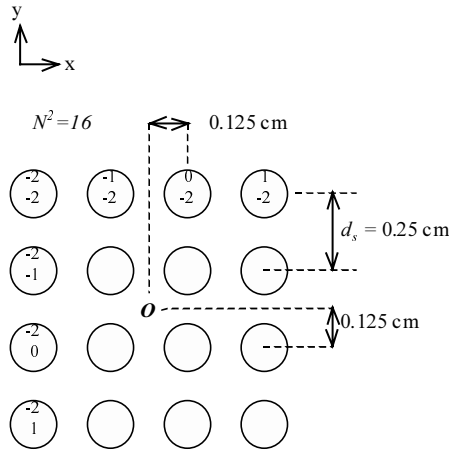


Figure 6.2 Top view of a $N^2 = 16$ point source grid: the circles indicate point source positions in the grid from the calculational model, denoted by their index number in x - and y -direction (i.e. top left = $(-2, -2)$). The origin of the source plane is denoted by O and indicated by the coordinates $(x, y, r) = (0, 0, 0)$. The source positions are spaced by a distance $d_s = 0.25$ cm in both perpendicular directions, centred around the origin of the grid.

Taking the central position in the source plane as the origin of a Cartesian coordinate system, we denote directions in the source and prescription plane by x and y and the perpendicular transversal direction by r . The primary therapeutic point of interest, centred in the prescription plane, is located at the position $(x, y, r) = (0, 0, 1)$ cm. We will denote this therapeutic point of interest by r_i . The source positions nearest to the origin of the source plane, denoted by O , are given by $(x, y, r) = (\pm 0.125; \pm 0.125; 0)$ cm (4 positions). The primary therapeutic point of interest r_i is the origin of the prescription plane.

6.3.2 Accumulated depth-dose

The dose rate in units [Gy/min], as a function of the depth into the target, denoted by r , for a mono-energetic point source emitting photons with an energy denoted by E , is given by

$$\dot{D}(r) = \left(\frac{\mu}{\rho} \right)_{en} \cdot \rho \cdot C_1 \cdot E \cdot \frac{A}{4\pi \cdot r^2} \cdot \exp\left(-\left(\frac{\mu}{\rho}\right) \cdot \rho \cdot r\right) \cdot B(r, E) \quad (6.1)$$

The accumulated dose rate that results from a source trajectory along all N^2 positions in x - and y -directions in the point source grid is then given by:

$$\dot{D}(r) = \sum_{x=-M}^{M-1} \sum_{y=-M}^{M-1} \left(\frac{\mu}{\rho} \right)_{en} \cdot \rho \cdot C_1 \cdot E \cdot \frac{\frac{A}{N^2}}{4\pi \cdot d(x, y, r)^2} \cdot \exp\left(-\left(\frac{\mu}{\rho}\right) \cdot \rho \cdot d(x, y, r)\right) \cdot B(r, E) \quad (6.2)$$

In these expressions, $M = N/2$, ρ stands for the mass density of water (1 g/cm³) and

$$d(x, y, r) = \sqrt{(r)^2 + (x \cdot 0.25 + 0.125)^2 + (y \cdot 0.25 + 0.125)^2} \quad (6.3)$$

in units [cm], represents the distance between a position ($d_s/2 - x \cdot d_s$, $d_s/2 - y \cdot d_s$, 0) (with $x, y = -M, -M+1 \dots M-2, M-1$) of the source in the source plane and a position (0, 0, r) along the axis that connects the origin of the source plane O with the origin of the prescription plane, r . The factor C_1 in the above expressions accounts for the conversion between different units: $C_1 = 60 \times 1.602 \times 10^{-13} \times 10^3$, i.e. conversion from seconds to minutes, from [MeV] to [J] and from [g] to [kg]. Mass attenuation coefficients (μ/ρ) and energy absorption coefficients (μ/ρ)_{en} are taken from Hubbell (1982), and dose build-up factors $B(r, E)$ are discussed in section 6.4.

The source activity is represented by A and denotes the activity of a virtual point source emitting mono-energetic photons with a radiation yield of $y(i) = 1$ photon (Bq \times s)⁻¹ (one photon per disintegration). Therefore, until real radionuclide radiation yield values $y(i)$ are taken into account, we will instead denote this virtual activity by the quantity A_{int} , the so-called ‘intermediate photon yield’, and express its value in units [Bq].

The calculational model makes use of the fact that the calculated depth-dose rate due to a real source with intermediate photon yield A_{int} that travels along all the N^2 source positions in the grid (representative for therapy) is equal to the accumulated depth-dose deposition per second due to simultaneous irradiation with N^2 sources with intermediate photon yield A_{int}/N^2 (as in the calculational model). In other words, it is assumed in the calculations that the source dwell time is equal for all the source positions in the grid.

6.3.3 Outline for therapeutic analysis

The requirements from section 6.1.1 can now be translated into the following outline for the analysis of source properties and aspects of therapeutic dose that are quantified in section 6.5:

1. The required intermediate photon yield A_{int} for a point source emitting mono-energetic photon radiation with energy E , that results in a dose deposition of 10 Gy at 1 cm depth in water, at the origin of the prescription plane, r_t (see section 6.5.1).
2. The required intermediate photon yield A_{int} for a point source emitting mono-energetic photon radiation with energy E , that results in an *average* dose deposition of 10 Gy in the prescription plane at 1 cm depth in water, with the restriction that dose deposition must take place within 1 minute per 10 cm² of target area, over a total area of 200 cm² at maximum, i.e. a maximum treatment time of 20 minutes (see section 6.5.2).
3. The so-called *transversal* homogeneity in the target, i.e. the ratio of dose deposition at the target surface at 0.5 cm and the prescription plane at 1 cm depth in water. The transversal homogeneity factor should be < 2 (see section 6.5.3).
4. The so-called *lateral* homogeneity in the prescription plane, i.e. the variation of dose deposition in x - and y -directions in the prescription plane itself. The lateral homogeneity factor should also be < 2 (see section 6.5.4).
5. The influence of the dimensions of the source applicator on items 1. through 4. This influence is quantified by determining both the required intermediate photon yield A_{int} and the transversal homogeneity (see sections 6.5.1 and 6.5.3, respectively) for different applicator areas A_{app} .
6. Therapy is performed with a source capsule that is attached to a drive wire and which contains radioactive material with finite dimensions. Attenuation of radiation by the source capsule is assessed in section 6.5.5, while the influence of self-absorption in the radioactive material itself is e.g. discussed in section 7.4.1 for iodine-125. By analyzing items 1, 2 and 5 we present a logical order to arrive at the final (i.e. after correction for source capsule absorption) values for the required intermediate photon yields A_{int} as a function of photon energy E , which are presented in section 6.5.6.

6.4 Compton scattering and dose build-up factors

Dose distributions in the prescription plane cannot merely be calculated assuming exponential attenuation that describes photoelectric absorption, as they are significantly influenced by Compton scattering of the low energy photons in the water medium. For water, the latter photon-matter interaction process becomes predominant over photoelectric absorption when energies are higher than ± 40 keV, as discussed by Storm and Israel (1970). In this context of

dose deposition in biologic media, we quote Williamson (1995), who argues that “in the ultra-low energy range (<40 keV), photoelectric absorption becomes significant” and “in the 60 to 200 keV range, energy transfer to biologic media is dominated by approximately elastic Compton interactions. Consequently, build-up of scattered photons overcompensates for primary photon attenuation”. Nath et al. (1999) allege that “at small distances from the source, dose perturbations caused by scatter and self-absorption of low-energy secondary radiations also make theoretical calculations difficult”.

In this study, the contribution of Compton scattered photons to dose deposition is taken into account by the dose build-up factor $B(r, E)$, (cf. equation (6.1)), equal to the ratio between total dose deposition (i.e. from both primary and secondary (scattered) radiation) and primary dose deposition.

A literature study on tabulated build-up factors revealed that these are scarce for low photon energies below 100 keV, and that most of them apply to the build-up of fluence instead of dose, i.e. they calculate the extra number of scattered photons at a certain point of interest, which is useful for shielding calculations. In dosimetry however, the energy of scattered photons and corresponding energy deposition at the point of interest needs to be included in calculations, in order to assess the total dose deposition.

For this study, Monte Carlo computer simulations were performed by Bom (1997), using GEANT software, described by Brun and Carminati (1994), in order to calculate dose build-up factors $B(r, E)$, at a distance r from a point source emitting mono-energetic photons with energy E . The simulation of dose distribution for an isotropic point source can be reduced to a one-dimensional geometry, due to the spherical symmetry. In case of a Compton interaction in the homogeneous water medium surrounding the point source, the energy of the scattered Compton electron is deposited at the location of interaction and qualified as primary (as is energy deposition due to photoelectric absorption of primary photons). The scattered Compton photon is further transported, based on the three-dimensional spatial distribution function for the Compton scattering, and after photoelectric absorption has taken place, the distance to the point source is calculated and the corresponding energy deposition is qualified as secondary. Energy deposition from double Compton scattered photons is also qualified as secondary.

As an illustration, we present in Figure 6.3 primary, secondary and total energy deposition around a point source in water emitting photons with energy $E = 100$ keV, together with the calculated dose build-up factor as a function of the radial distance r .

The primary and secondary energy deposition are equal at $r = 2.5$ cm, and for higher radial distances the secondary energy deposition is predominant, continues to increase, and reaches a maximum at about $r = 10$ cm. At this distance there is almost no energy deposition from primary, i.e. unscattered photons, and the dose build-up factor is ~ 8 . For radial distances $r > 10$ cm the secondary dose deposition and thus the total energy deposition starts to decrease. Statistical fluctuations in the simulated dose build-up data for $r > 30$ cm in the figure are caused by the fact that there is very little energy deposition at these distances.

Similar simulations have been performed for $10 < E < 100$ keV, at a pitch of 10 and 20 keV, and for $E > 100$ keV, at a pitch of 50 keV. For photon energies $10 < E < 100$ keV, most of the energy is deposited within several centimeters from the point source and the highest values for $B(r, E)$ (i.e. maximum contribution of secondary dose deposition) are found for $E \sim 50$ -60 keV.

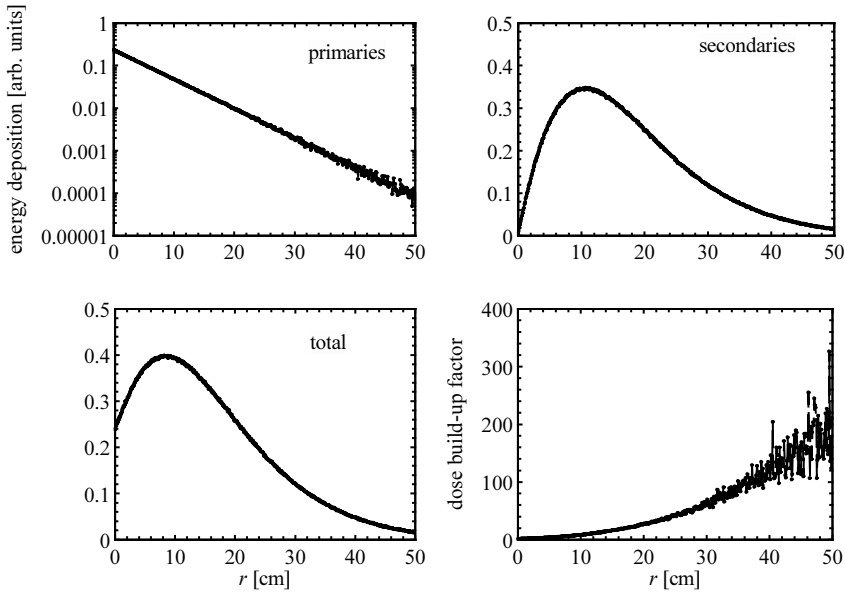


Figure 6.3 Primary, secondary and total energy deposition around an isotropic point source in water emitting photons with energy $E = 100$ keV, together with the derived dose build-up factor as a function of the radial distance r .

The simulated dose build-up data in the energy range from 10 to 100 keV are fitted with second-order polynomials (the deviation between fitted and simulated data is within 5%) in the radial range up to $r = 4$ cm. Dose build-up factor data in the range $r < 4$ cm for 10 keV photons showed poor statistics due to the strong photoelectric absorption in the water.

Dose build-up factors were finally quantified at a pitch of 5 keV for $10 < E < 100$ keV by linear interpolation on the simulated data and implemented in the equations from section 6.3.2.

Dose build-up factors for photon energies $E < 100$ keV are determined by Chilton et al. (1984) at $r = 1$ cm, the results of which are shown in Table 6.1. Dose build-up factors from Chilton et al. are higher within 10% than those from GEANT simulations. Unfortunately, Chilton et al. do not discuss experimental circumstances, nor is it explained how secondary dose deposition is separately quantified. This hinders straightforward comparison with the values derived from GEANT simulations. The consistency within 10% is nevertheless considered acceptable for the purpose of verifying simulations.

Table 6.1 Dose build-up factors in water, from GEANT simulations and from Chilton et al. (1984) for photon energies E , at $r = 1$ cm.

E [keV]	GEANT	Chilton et al. 1984	difference [%]
40	1.60	1.68	5.0
60	1.57	1.67	6.4
80	1.44	1.57	9.0
100	1.38	1.47	6.5

6.5 Therapeutic dose distributions

This section presents results of the analysis of source properties and therapeutic dose distributions according to the outline presented in section 6.3.3.

6.5.1 Required intermediate photon yield (I)

Firstly, we compare the depth-dose distributions for a single point source in water, emitting photons with two different energies $E = 10$ and 35 keV. The latter energy is that of the gamma line from ^{125}I , which was considered a suitable radionuclide for an IOBT source, as discussed in section 7.2. The results are depicted in Figure 6.4. The depth-dose distribution curves are shown in arbitrary units and have been normalized at $r = 0.5$ cm.

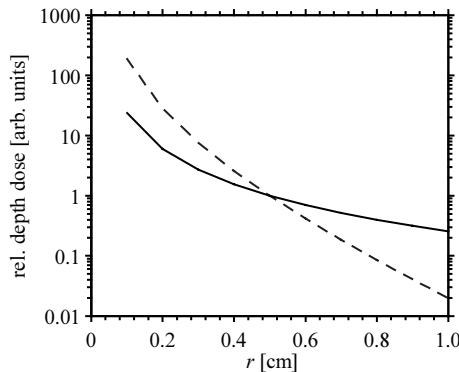


Figure 6.4 Relative depth-dose distribution curves, normalized at $r = 0.5$ cm, as a function of the radial distance r in water for a single point source emitting photons with energies $E = 10$ keV (dashed) and 35 keV (solid).

It is evident that the 10 keV depth-dose distribution curve shows stronger attenuation than the 35 keV curve; almost a factor 10^4 for 10 keV vs. a factor of about 10^2 for 35 keV in the radial

range $0.1 < r < 1$ cm. For photons with higher energies the curves will decrease more gradually with increasing r due to lower photon absorption probability.

Secondly, if the single point source is replaced in the calculations by a relatively small source applicator, e.g. one for which $N = 16$ and $A_{app} = 14.1 \text{ cm}^2$, the depth-dose rate curve along the axis that connects O with r_t decays more gradually in the radial range $0.1 < r < 1$ cm, e.g. with a ratio of 3.2 for 35 keV photons, as is depicted in Figure 6.5. Since the total treatment time for delivery of 10 Gy is restricted to 20 minutes, the corresponding required dose rate at r_t is 0.5 Gy/min. For 35 keV photons, this results in a value $A_{int} = 387.4 \text{ GBq}$.

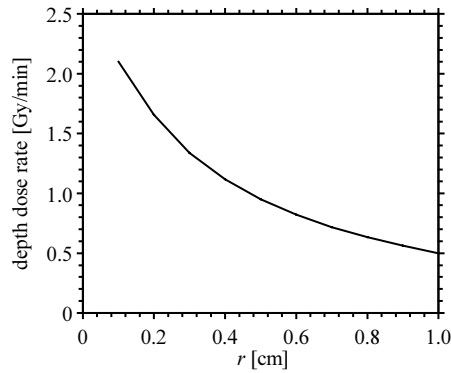


Figure 6.5 Depth-dose rate curve along the axis that connects the origin of the source plane O with r_t for a source applicator with area $A_{app} = 14.1 \text{ cm}^2$ and a point source with $E = 35 \text{ keV}$ and $A_{int} = 387.4 \text{ GBq}$, resulting in a value of 0.5 Gy/min at r_t .

Thirdly, it is even more interesting to consider the case $N = 56$, since then $A_{app} = 189.1 \text{ cm}^2$, which is in the calculations a practical value close to the maximum prescription plane area (200 cm^2). Increasing the applicator size amounts to a larger average distance between the source positions and r_t and as a consequence the values for A_{int} increase, to a value of $A_{int} = 1.51 \times 10^3 \text{ GBq}$ for $E = 35 \text{ keV}$. Other values are: $A_{int} = 113.3 \times 10^3$, 1.36×10^3 and $1.24 \times 10^3 \text{ GBq}$ for $E = 10, 20$ and 100 keV , respectively. The generalized result for $10 < E < 100 \text{ keV}$ is depicted in Figure 6.6.

Photons with $E = 10 \text{ keV}$ suffer strong absorption before reaching r_t in the prescription plane. As a consequence, dose deposition at r_t is almost entirely due to (few) central source positions around O . Since very little energy is deposited, A_{int} is very high.

Photons with $E = 25 \text{ keV}$ are absorbed (much) less and show a better match between their penetrative range and the (low) average distance between r_t and the nearest source positions (central source positions around O). Although there are still few of these source positions which are relevant for the dose at r_t , the energy deposition has increased considerably, resulting in a (much) lower value for A_{int} .

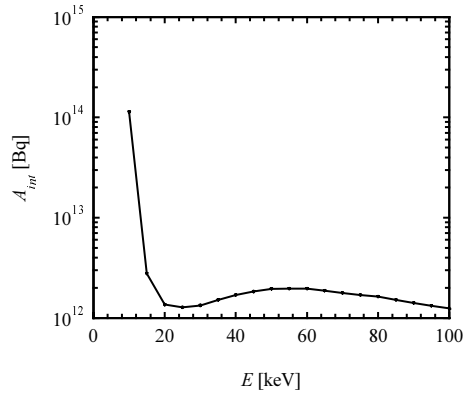


Figure 6.6 Required intermediate photon yield A_{int} in units [Bq] as a function of photon energy E that results in a value of 0.5 Gy/min at r_i for a source applicator with $N = 56$ and $A_{app} = 189.1 \text{ cm}^2$.

Photons with energies E in the range 25-50 keV are less effective; the energy deposition at r_i due to the nearest source positions has decreased and is not compensated by contributions from more remote source positions, despite the fact that these are larger in number. This also explains the minimum value for A_{int} .

Compensation is however the case for $E > 50 \text{ keV}$; the higher penetrative range of these photons results in predominant dose contributions at r_i from (a large number of) remote source positions. This explains the lower values for A_{int} .

6.5.2 Required intermediate photon yield (II)

Whereas up to this point only the dose deposition at r_i has been quantified, in this section we determine the dose distribution in the prescription plane.

In therapy, dose planning is generally performed by assigning source dwell times to the different positions in the source applicator that will yield the desired dose distribution in the prescription plane. As the photon energy increases, the dose deposition at any position in the prescription plane is determined by a larger number of source positions due to the higher penetrative range of the photons. As a consequence, the dose deposition in and around r_i will be higher than at the edges of the prescription plane.

Therefore, in order to achieve a uniform dose distribution in the prescription plane, dwell times for source positions nearby the edges of the prescription plane will have to be longer to compensate for the smaller accumulated dose deposition in these regions. In other words, equal dwell times for all source positions result in a convex dose profile in the prescription plane, whereas a homogeneous dose distribution (within a factor 2, see section 6.5.4) is what is generally being aimed at. Therefore dwell times for central positions in the source plane will have to be shorter than those at the edges. As a consequence, any realistic dwell time distribution for a source with intermediate activity A_{int} as calculated in section 6.5.1 would

result in dose rates that are lower than the required value of 0.5 Gy/min, for *all* positions in the prescription plane.

The values for A_{int} that result in an average dose rate of 0.5 Gy/min will therefore turn out to be higher than those predicted by the calculations of section 6.5.1. In order to arrive at a better estimate for A_{int} we could try to find the source dwell time distribution that results in a uniform dose deposition in the prescription plane.

We will instead apply a more straightforward approximation in order to get a better estimate for A_{int} . We determine the values for A_{int} for a point source emitting monoenergetic photon radiation with energy E , that results in an *average* dose rate of 0.5 Gy/min in the prescription plane for an applicator with $N = 56$, under the assumption that the source dwell time is equal for all source positions. In the calculations, the area of the prescription plane is equal to A_{app} , i.e. 189.1 cm^2 . The results are depicted in Figure 6.7 through Figure 6.9, where we show dose rate distributions in the prescription plane for photons with energies $E = 10, 20$ and 100 keV , respectively, together with isodose rate curves with indicated values in units [Gy/min]. In order to achieve average dose rates of 0.5 Gy/min, intermediate photon yields $A_{int} = 128.8 \times 10^3, 1.57 \times 10^3$ and $1.65 \times 10^3 \text{ GBq}$ for $E = 10, 20$ and 100 keV , respectively, are required. The generalized result for all photon energies $10 < E < 100 \text{ keV}$ is depicted as the dashed curve in Figure 6.10.

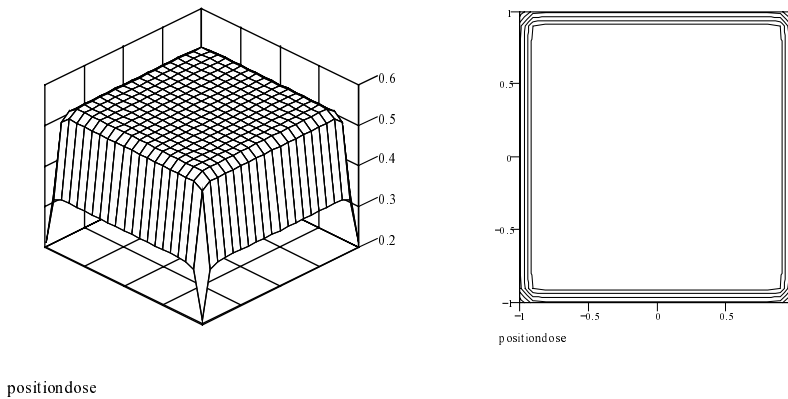


Figure 6.7 The dose rate distribution in a 189.1 cm^2 prescription plane with indicated values in units [Gy/min] that results from a point source emitting photons with $E = 10 \text{ keV}$, together with isodose rate curves. The required intermediate photon yield $A_{int} = 128.8 \times 10^3 \text{ GBq}$, resulting in an average dose rate of 0.5 Gy/min.

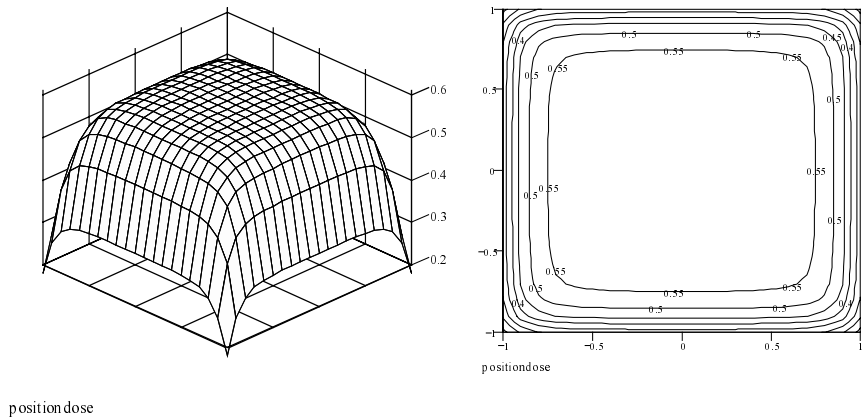


Figure 6.8 The dose rate distribution in a 189.1 cm^2 prescription plane that results from a point source emitting photons with $E = 20 \text{ keV}$, together with isodose rate curves with indicated dose rate values in units [Gy/min]. The required intermediate photon yield $A_{int} = 1.57 \times 10^3 \text{ GBq}$, resulting in an average dose rate of 0.5 Gy/min .

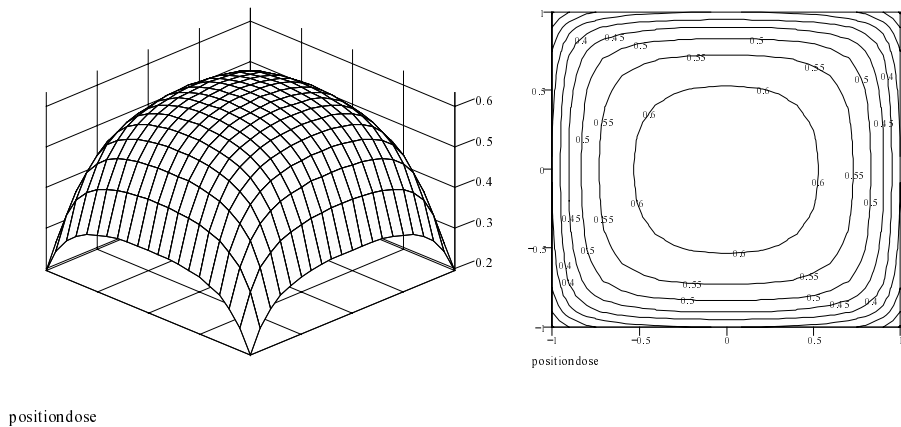


Figure 6.9 The dose rate distribution in a 189.1 cm^2 prescription plane that results from a point source emitting photons with $E = 100 \text{ keV}$, together with isodose rate curves with indicated dose rate values in units [Gy/min]. The required intermediate photon yield $A_{int} = 1.65 \times 10^3 \text{ GBq}$, resulting in an average dose rate of 0.5 Gy/min .

The values for A_{int} are indeed higher than those in Figure 6.6 (cf. section 6.5.1), by 13.7%, 15.4% and 33.1% for $E = 10, 20$ and 100 keV, respectively. The difference is most noticeable for the higher energies between $50 < E < 100$ keV as these result in more convex dose profiles in the prescription plane as was discussed above. For these energies, the accumulated dose rate at r_t is higher than the average value of 0.5 Gy/min, but dose rates decrease considerably in directions away from r_t , towards the edges of the prescription plane. As a consequence, values for A_{int} for $50 < E < 100$ keV are higher by 27% to 33% than those calculated in section 6.5.1. The shape of the curve that represents the energy dependence remains essentially the same as that of Figure 6.6, however.

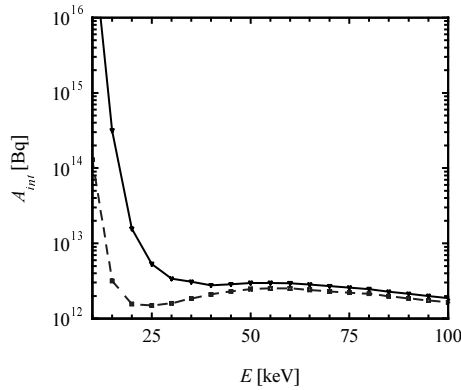


Figure 6.10 Intermediate photon yields A_{int} as a function of photon energy E , required in order to deliver an average dose rate of 0.5 Gy/min in a 189.1 cm^2 prescription plane at a depth of $r = 1$ cm in water, before (dashed) and after (solid) correction for the source capsule absorption.

6.5.3 Transversal homogeneity in the target

In therapy, a homogeneous dose distribution in the target volume is what is generally being aimed at, although dose-limiting healthy tissues adjacent to the target may necessitate a compromise.

Transversal homogeneity denotes the ratio between dose deposition in the target surface at 0.5 cm from the source plane and dose deposition in the prescription plane at 1 cm depth in water and should be < 2 . A single isotropic point source will never meet this restriction as the geometrical reduction in dose deposition between $r = 0.5$ and 1 cm is already a factor 4 (the decrease is proportional to $1/r^2$). As was explained in section 6.5.2, dose distributions in the target depend on the penetrative power of the photons.

This implies that the dose homogeneity in the target depends on both photon energy and the dimensions of the source applicator. In order to assess these dependencies, the ratio between dose deposition at $(x, y, r) = (0, 0, 0.5)$ and r_t has been calculated, assuming equal dwell times for all source positions.

Firstly, the influence of the applicator area A_{app} was quantified for photons with energy $E = 35$ keV. The result is shown in the picture on the left in Figure 6.11. The requirement on transversal homogeneity is met for $A_{app} > 14.1$ cm² ($N = 16$) for $E = 35$ keV. Since a real applicator will probably have an area that is larger than 14.1 cm² during therapy, transversal homogeneity in the target will not be a bottleneck for photons with $E = 35$ keV.

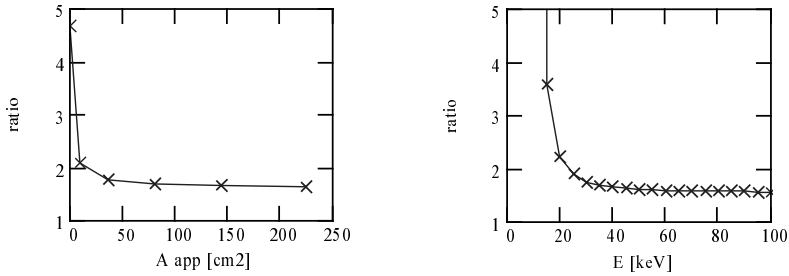


Figure 6.11 Ratio between dose deposition at $(x,y,r) = (0, 0, 0.5)$ and r_t , as a function of the applicator area A_{app} for photons with energy $E = 35$ keV (left) and as function of photon energy E for an applicator area $A_{app} = 189.1$ cm² (right).

Secondly, the picture on the right in Figure 6.11 shows the energy dependence of the ratio for $A_{app} = 189.1$ cm². For photons with energies $E < 25$ keV the requirement on transversal homogeneity in the target is not met due to strong absorption of the photons in the water before the prescription plane is reached. Photons with energies above 25 keV however meet the requirement on transversal homogeneity as the ratio drops below 2 and remains more or less constant as the photon energy increases up to 100 keV.

6.5.4 Lateral homogeneity in the prescription plane

The lateral homogeneity denotes the uniformity of the dose profile in the prescription plane itself and should be within a factor 2, just like the transversal homogeneity. As has been discussed in section 6.5.2, the dose profiles in the prescription plane depend on the source dwell time distribution, the photon energy E and the dimensions of the source applicator, i.e. A_{app} . The influence of the latter is reduced for lower photon energies as dose is deposited more locally and lateral dose profiles are more homogeneous, assuming equal dwell times (cf. Figure 6.7 through Figure 6.9).

For higher energies, lateral homogeneity must be achieved by choosing the optimal source dwell time distribution that results in a uniform dose distribution in the prescription plane. The latter is not always planar, but may have any other shape, depending on the accessible body cavity for the delivery of brachytherapy (in this study however, we only consider the planar case).

Based upon the above verification, the reduction in dose rate at $r = 1$ cm (indicated by the symbol X in Figure 6.12) due to absorption of the source capsule was assessed by simulations with the isotropic point source positioned at the centre of the microSelectron-HDR V2 stainless steel source capsule (indicated by the asterisk in Figure 6.12), for photons with energies $E < 100$ keV, at a pitch of 5 keV. For these energies, a comparison was made with analytical calculations of the dose rates from an isotropic point source in a homogeneous water medium.

The results are depicted in Figure 6.13. The energy dependence of the solid curve that describes the dose rate in absence of the source capsule, is approximately the reverse of that of Figure 6.6, for similar reasons as discussed in section 6.5.1. The dashed curve indicates that for photons with $E < 50$ keV, the attenuation of the source capsule is considerable, resulting in a large reduction in dose rate. The absorption of photons by the source capsule decreases as E increases up to 100 keV: for this energy, the relative decrease in dose rate at $r = 1$ cm is in the order of only $\sim 10\%$. Table 6.2 quantifies the source capsule absorption for different photon energies.

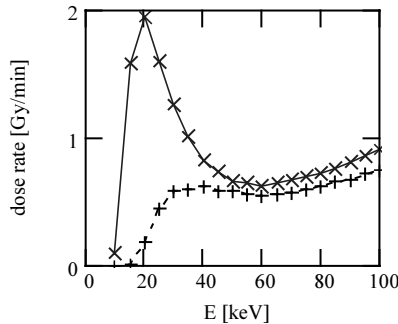


Figure 6.13 Dashed: simulated dose rate in units [Gy/min] at 1 cm depth in water from a single isotropic point source with an intermediate photon yield $A_{int} = 3.7 \times 10^{11}$ Bq as a function of the photon energy E in units [keV], with inclusion of the microSelectron-HDR V2 stainless steel source capsule in the simulated geometry. Solid: calculated dose rate at 1 cm depth from the same isotropic point source in water, in absence of the source capsule.

Table 6.2 The source capsule absorption, quantified as the relative decrease in dose rate at $r = 1$ cm, as a function of photon energy E .

E [keV]	source capsule absorption [%]
15	99
20	90
25	72
30	53
35	40
40	24
45	20
50	17
55	16
60	15
65	15
70	15
75	14
80	14
85	13
90	13
95	13
100	12

Although it is evident that the capsule absorption greatly hinders the use of low photon energies, it is the combination of specific activity of a radionuclide and source capsule absorption that is relevant in terms of feasibility for IOBT. The available volume of the source capsule is relatively small and necessitates a high specific activity of the IOBT source. If the capsule absorption exceeds 50%, less than half of the photons emitted by the source contributes to dose deposition in the target. Based upon this restriction, the lower limit for the energy E of an IOBT source is therefore estimated at ~ 30 keV.

6.5.6 Final values for the required intermediate photon yield

The values from Table 6.2 have been used to derive the solid curve in Figure 6.10 that describes the final values (i.e. corrected for source capsule absorption) for A_{int} as a function of photon energy E , required to deliver an average dose rate of 0.5 Gy/min in a 189.1 cm^2 prescription plane at a depth of 1 cm in water. These values are tabulated in Table 6.3.

Table 6.3 Final values (corrected for source capsule absorption) for A_{int} as a function of photon energy E for an average dose rate of 0.5 Gy/min in a 189.1 cm² prescription plane at 1 cm depth in water.

E [keV]	A_{int} [Bq]
10	1.29×10^{17}
15	3.17×10^{14}
20	1.57×10^{13}
25	5.35×10^{12}
30	3.41×10^{12}
35	3.08×10^{12}
40	2.78×10^{12}
45	2.88×10^{12}
50	2.99×10^{12}
55	2.99×10^{12}
60	2.97×10^{12}
65	2.83×10^{12}
70	2.71×10^{12}
75	2.57×10^{12}
80	2.48×10^{12}
85	2.28×10^{12}
90	2.14×10^{12}
95	2.00×10^{12}
100	1.87×10^{12}

6.6 Calculations on radiation safety

In order to ensure radiation safety during IOBT it is necessary to estimate the required radiation shielding that restricts the effective dose received by a member of the medical staff to an acceptable value.

In section 5.1.2, it was mentioned that the effective dose received by a member of the medical staff due to interventional procedures may vary between 2 and 25 μ Sv per treatment. Although these values apply to vascular brachytherapy, an allowable effective dose during IOBT should be in the same order of magnitude, viz. 1 to 10 μ Sv per treatment of 20 minutes.

As explained in section 5.1.3, the determination of radiation safety is based upon the air kerma rate that yields a conservative estimate for the effective dose received by a member of the medical staff.

6.6.1 Therapeutic energies below 100 keV

The photon radiation from the IOBT source is attenuated by the body of the patient, but, as will be shown, additional shielding is required in order to restrict the air kerma rate to an acceptable level. Lead is a commonly used shielding material during radiation therapy; lead aprons, shields, screens and glasses are commercially available and serve to protect the medical staff from overexposure.

Table 6.4 Required separate lead and water slab thicknesses d_{lead} and d_{water} in units [cm] that restrict the air kerma rate at $r = 1$ m to 3 $\mu\text{Gy/h}$ and 30 $\mu\text{Gy/h}$, respectively.

E [keV]	air kerma rate = 3 $\mu\text{Gy/h}$		air kerma rate = 30 $\mu\text{Gy/h}$	
	d_{lead} [cm]	d_{water} [cm]	d_{lead} [cm]	d_{water} [cm]
10	0.011	3.19	0.009	2.76
15	0.012	9.61	0.011	8.23
20	0.013	15.38	0.012	12.53
25	0.017	20.35	0.013	15.99
30	0.030	26.11	0.023	20.00
35	0.038	29.79	0.029	22.43
40	0.057	33.19	0.042	24.59
45	0.070	35.01	0.051	25.61
50	0.095	36.44	0.068	26.31
55	0.116	38.46	0.084	27.82
60	0.152	40.17	0.108	28.98
65	0.172	41.61	0.124	30.04
70	0.201	42.59	0.145	30.72
75	0.242	43.82	0.174	31.57
80	0.306	44.63	0.220	32.10
85	0.414	45.79	0.299	32.97
90	0.104	47.05	0.076	34.04
95	0.115	48.01	0.083	34.77
100	0.128	49.15	0.093	35.68

We therefore calculate (using equation 5.3) the required thicknesses d_{water} and d_{lead} for water and lead slabs that separately (i.e. in absence of the other medium) restrict the air kerma rate at a distance of $r = 1$ m to values of 3 and 30 $\mu\text{Gy/h}$, respectively. The values for d_{water} and d_{lead} apply to an isotropic point source with required intermediate photon yield A_{int} , before correction for source capsule absorption (the dashed curve in Figure 6.10). The results are presented in Table 6.4.

A lead apron that can be used by a member of the medical staff has a maximum thickness of about 0.5 mm. In addition to this, it may be possible to integrate a lead foil with the source applicator, if sterility of the latter during surgery can be guaranteed. This lead foil would probably not be thicker than ~ 1 mm in order to maintain a flexible applicator.

Therefore, taking ~ 1.5 mm of lead as the maximum amount of shielding that can be applied during treatment, the least restrictive air kerma rate of 30 $\mu\text{Gy/h}$ indicates an upper

limit for E of ~ 70 keV. The body of the patient may provide additional shielding, although several tens of centimeters of water are required for significant attenuation of the higher photon energies. Assuming that there *is* some additional attenuation in the patient's body for the higher photon energies, and given the fact that $d_{lead} < 1$ mm again for $E > 88$ keV (the lead K-shell binding energy), the upper limit for the photon energy E of an IOBT source is assigned a value of ~ 100 keV.

6.6.2 Shielding of energies above 100 keV

The previous section indicates that a potential radionuclide should not have a high radiation yield $y(i)$ for gamma and/or X-ray photons with $E > 100$ keV: although these photons contribute (significantly) to therapeutic dose delivery in the target, this does not compensate for the shielding difficulties they entail during IOBT.

We therefore calculate the so-called maximum allowed intermediate photon yield A_{all} that restrict the air kerma rate at $r = 1$ m distance to $30 \mu\text{Gy/h}$, for photons with $E > 100$ keV, emitted by an isotropic point source in water that is shielded by 1.5 mm of lead. The results are depicted in Figure 6.14 and tabulated in Table 6.5 (see next page).

The values can be used to determine whether the emission rate of high energy ($E > 100$ keV) photons by a potential IOBT source is acceptable. This will be illustrated in section 7.5 when we determine the shielding of high energy gamma radiation from ^{126}I .

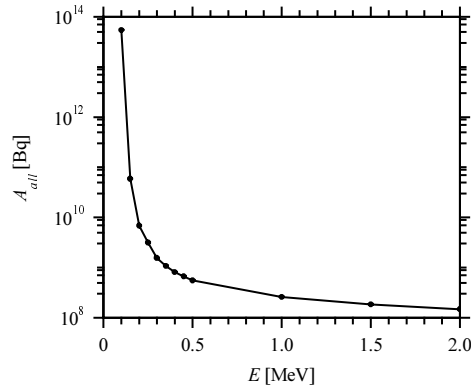


Figure 6.14 Maximum allowed intermediate photon yields A_{all} in units [Bq], that restrict the air kerma rate at $r = 1$ m distance to 30 , Gy/h for photons with energies $100 \text{ keV} < E < 2 \text{ MeV}$, emitted by an isotropic point source in water and shielded by 1.5 mm of lead.

Table 6.5 Maximum allowed intermediate photon yields A_{all} in units [Bq], that restrict the air kerma rate at $r = 1$ m distance to 30 , Gy/h for photons with energies $100 \text{ keV} < E < 2 \text{ MeV}$, emitted by an isotropic point source in water and shielded by 1.5 mm of lead.

E [MeV]	A_{all} [Bq]
0.10	5.44×10^{13}
0.15	5.92×10^{10}
0.20	6.85×10^9
0.25	3.18×10^9
0.30	1.56×10^9
0.35	1.07×10^9
0.40	8.14×10^8
0.45	6.66×10^8
0.50	5.55×10^8
1.00	2.59×10^8
1.50	1.85×10^8
2.00	1.48×10^8

7 Selection of radionuclides for application in IOBT

In Chapter 6 the useful therapeutic range of photon energies for an IOBT source was roughly estimated at 30-100 keV. A preliminary selection of potential radionuclides should therefore be based upon the presence of these energies in the emission spectrum.

Useful references for this selection are provided by Erdtmann and Soyka (1979) and Slater (1962), with tabulated radionuclide data for gamma and/or X-ray lines in order of increasing photon energy.

7.1 Outline for feasibility analysis

The selection of suitable radionuclides is pursued with a calculation of the maximum specific activity (the activity per unit mass) S_{max} in units [Bq/g], as discussed by Wilson (1966):

$$S_{max} = \lambda \times \frac{N_A}{M} \quad (7.1)$$

where $\lambda = (\ln 2)/t_{1/2}$ is the decay constant for the nuclide in units [s^{-1}], describing the fraction of nuclei that decays every second. The demand on the half-life of the radionuclide comes into play here: $t_{1/2}$ should be longer than 30 days for reasons of practical application of the source, as required by Nucletron (1997).

$N_A = 6.02 \times 10^{23} \text{ mol}^{-1}$ is Avogadro's number and M denotes the molar mass of the nucleus in units [g mol^{-1}]. With ρ as the mass density of the radionuclide in units [g cm^{-3}] and V_s as the available source volume ($\sim 1 \text{ mm}^3$, see section 6.5.5), the maximum activity A_c in units [Bq] that can be contained in the source capsule, assuming a 100% abundance of the radionuclide, is given by $A_c = \rho V_s S_{max}$.

7.1.1 Therapeutic requirements

Firstly, if a radionuclide emits a photon with radiation yield $y(i)$ and energy E in the useful therapeutic energy range (30-100 keV), the requirement

$$A \cdot y(i) \geq A_{int}(E) \quad (7.2)$$

must be met, with $A_{int}(E)$ as the required intermediate photon yield for energy E , corrected for absorption in the source capsule (see Table 6.3). Likewise, if the radionuclide emits n photons with energies $30 < E_i < 100$ keV ($i = 1 \dots n$), the above expression extends to:

$$\sum_{i=1}^n \frac{A_c \cdot y(i)}{A_{int}(E_i)} \geq 1 \quad (7.3)$$

Secondly, if the above requirement is met, the chemical composition of the source material comes into play; if the source consists of the therapeutic radionuclide together with a carrier (i.e. as a composite material), the atomic abundance of the radionuclide in the source will be reduced. The presence of other isotopes from the same element, either due to a natural abundance $< 100\%$, or e.g. produced during neutron activation, also reduces the atomic abundance of the therapeutic radionuclide. We denote the overall abundance of the latter by f_1 . The maximum activity that can be contained in the source capsule is then equal to $f_1 A_c$.

Thirdly, self-absorption of photons in the source material leads to a lower emission rate for the source which results in reduced dose deposition in the target. The self-absorption is quantified as the relative decrease in dose rate at $r = 1$ cm from the source centre and is denoted by f_2 . In section 7.4.1 we determine the self-absorption in an ^{125}I source.

Correction for overall abundance of the radionuclide and self-absorption in the source material are taken into account by calculating the effective activity

$$A_{eff}(E) = A_c \cdot f_1(1 - f_2(E)) \quad (7.4)$$

in units [Bq], of the source contained in the source capsule. The following requirement must then be met:

$$\sum_{i=1}^n \frac{A_{eff}(E_i) \cdot y(i)}{A_{int}(E_i)} \geq 1 \quad (7.5)$$

7.1.2 Shielding requirements

If the therapeutic requirements are met for a potential source, the feasibility of shielding high energy ($E > 100$ keV) photons must be determined. Absorption of these photons in the source capsule absorption is ignored in the calculations as the corresponding decrease in air kerma

rate is only 12% for $E = 100$ keV and less for higher photon energies (cf. Table 6.2). Self-absorption of these high energy photons is ignored as well (although this depends on the specific source material), resulting in an upper limit for the air kerma rate in the context of radiation safety.

The overall abundance of the radionuclide, emitting m photons with energies $E_i > 100$ keV ($i = 1 \dots m$) and radiation yields $y(i)$, is taken into account by multiplying the activity A_c by f_i (this also applies to photons with $E > 100$, emitted by a *non-therapeutic* radionuclide).

In section 6.6.2 we calculated the maximum allowed intermediate photon yields A_{all} in units [Bq], for photons with $E > 100$ keV, for an isotropic point source which can still be shielded sufficiently during treatment. Therefore, in order to decide whether the use of an IOBT source emitting photons with $E > 100$ keV conflicts with radiation safety requirements, we compare A_{all} with the photon yield from the anticipated source:

$$\sum_{i=1}^m \frac{A_c f_i \cdot y(i)}{A_{all}(E_i)} \leq 1 \quad (7.6)$$

7.2 Suitability of ^{125}I

Iodine-125 might be a suitable radionuclide for an IOBT source; this radionuclide, with a half-life $t_{1/2} = 60.14$ days, emits a gamma line with energy $E = 35.5$ keV and radiation yield $y(i) = 0.07$ (Bq x s) $^{-1}$ (data from Sowby et al. (1983)) and K X-rays with energies between 27 and 32 keV, resulting in an average photon energy $E_{mean} = 28.4$ keV. Nath et al. (1997) allege that, for depths up to 10 mm, even low-energy gamma emitters such as ^{125}I provide as good penetration in depth as (the commonly used in brachytherapy) ^{192}Ir . Nath et al. however also question whether the specific activity of ^{125}I would be high enough for a catheter-based system. In this context, we determine in the next sections whether the specific activity of ^{125}I is high enough for application in IOBT, by following the outline for feasibility analysis from section 7.1.

7.2.1 Maximum specific activity

With $\tau = 133.4 \times 10^{-9}$ s $^{-1}$ for ^{125}I , we calculate $S_{max} = 640.3 \times 10^{12}$ Bq g $^{-1}$. Since $V_s = 1.2$ mm 3 (see Figure 6.12) and $\rho = 4.93$ g cm $^{-3}$, it follows that $A_c = 3.79 \times 10^{12}$ Bq, and therefore $\Sigma = (A_c \cdot y(i) / A_{int}(E_i)) = 1.17$, with values for E_i rounded off to values in Table 6.3.

It is anticipated that the requirement for the effective source activity A_{eff} from equation (7.5) is not met; with the overall radionuclide abundance and self-absorption yet to be taken into account, there is only a margin of 17% in the photon yield. We will however continue the analysis for ^{125}I in order to illustrate the outline from section 7.1. Therefore, the issues of chemical composition of the source material and production of ^{125}I now come into play.

7.3 Production of ^{125}I

^{125}I can be produced by means of (n,γ) neutron activation of ^{124}Xe . The isotopes which occur in the relevant neutron activation and decay processes are depicted in Figure 7.1.

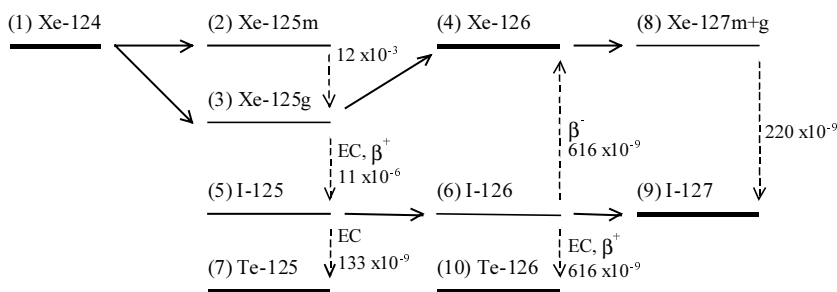


Figure 7.1 Relevant neutron activation and decay processes in the production of ^{125}I . Neutron activation processes are indicated by solid arrows, decay processes by dashed downwards and upwards arrows. Stable isotopes are depicted with thick solid lines, metastable and ground states of isotopes are indicated by m and g. Decay processes have been quantified by indicated values for $\lambda_{i \rightarrow j} = (\ln 2)/t_{1/2}$ in units $[\text{s}^{-1}]$.

When irradiated, ^{124}Xe (usually enriched, since the natural isotopic abundance is only 0.096%) converts into ^{125}Xe (in metastable and ground state), which decays with a half-life of $t_{1/2} = 17.3$ hrs to ^{125}I , which subsequently decays via electron capture to the stable ^{125}Te . Neutron activation processes (n,γ) are depicted in Figure 7.1 by solid arrows and decay processes by dashed arrows. Stable isotopes are depicted with thick solid lines, while metastable and ground states of isotopes are indicated by m and g, respectively.

The ^{125}I yield is given by the solution to the set of coupled differential equations that describes the system, as discussed in the analysis of neutron activation by Erdtmann (1976). The latter analysis does however not include secondary neutron activation (neutron capture by primary activation products). Since the secondary neutron activation processes $\text{Xe-125g } (n,\gamma) \rightarrow \text{Xe-126}$, $\text{I-125 } (n,\gamma) \rightarrow \text{I-126}$ and $\text{I-126 } (n,\gamma) \rightarrow \text{I-127}$ influence the I-125 yield, another approach was chosen which is discussed in the next section.

7.3.1 Compartment model algorithm

An algorithm presented by Blaauw (1993a) offers a numerical solution to the set of coupled differential equations that describes a system of neutron activation and decay processes. It is used to treat a system with various isotopes as a collection of compartments, each of which contains the number of atoms of an isotope at time t .

The input for the computer program that calculates the dynamic contents of the compartments consists of the number of atoms at $t = 0$ and the transfer rates between

7.3.2 Neutron activation of ^{124}Xe

A first calculation was performed with 100 ^{124}Xe atoms present at $t = 0$ and determine the relative amount of ^{125}I , ^{126}I and ^{127}I , where it is assumed that the iodine can later on be separated chemically from the other (Te and Xe) isotopes. The result is depicted in Figure 7.2.

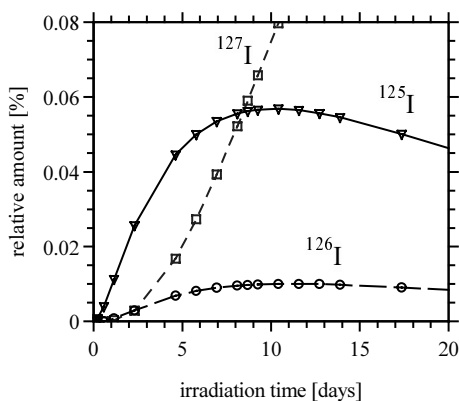


Figure 7.2 The relative amount in the iodine mixture for ^{125}I (solid, ∇), ^{126}I (dashed, \circ) and ^{127}I (dashed, \square) atoms after irradiation of 100 ^{124}Xe atoms, present at $t = 0$, with neutron flux values $\phi_{th} = 2 \times 10^{15}$ neutrons $\text{s}^{-1} \text{cm}^{-2}$, $\phi_{epi} = 5 \times 10^{13}$ neutrons $\text{s}^{-1} \text{cm}^{-2}$ and $\phi_j = 5 \times 10^{14}$ neutrons $\text{s}^{-1} \text{cm}^{-2}$.

After 10.5 days of irradiation and before any chemical separation has taken place, a maximum relative ^{125}I atom fraction of 5.7% is achieved, i.e. a contribution of 38.8% for ^{125}I in the iodine mixture, together with relative atom fractions of 6.8% and 54.4% in the iodine mixture for ^{126}I and ^{127}I , respectively. The value of 38.8% implies that the overall abundance of ^{125}I in a compound source material, or even in a carrier-free iodine source, is too low in order to meet the therapeutic requirement from equation (7.4); it follows that $f_I \Sigma (A_c \gamma(i) / A_{int}(E_i)) = 0.45$.

Besides the necessity for a higher ^{125}I abundance, the iodine mixture must also contain as little ^{126}I as possible, since the latter radionuclide ^{126}I , with a half-life $t_{1/2} = 13.02$ days, emits high energy photons that are undesirable for IOBT purposes (see section 6.6.2). The decay modes are electron capture, β^- and β^+ emission, the latter resulting in $E = 511$ keV annihilation gamma photons with a radiation yield $\gamma(i) = 6.66 \times 10^{-2}$ ($\text{Bq} \times \text{s}$) $^{-1}$. Table 7.2 lists the gamma lines emitted by ^{126}I with corresponding radiation yields $\gamma(i)$, taken from Sowby et al. (1983).

Table 7.2 Gamma lines emitted by ^{126}I with corresponding radiation yields $y(i)$.

E [keV]	$y(i)$ [(Bq x s) $^{-1}$]
389	3.41×10^{-1}
491	2.85×10^{-2}
511	6.66×10^{-2}
666	3.31×10^{-1}
754	4.16×10^{-2}
1420	2.95×10^{-3}

If irradiation of ^{124}Xe is performed during several hours (instead of days) with neutron fluxes that are lower than those of the HFIR by two orders of magnitude, i.e. $\phi_{th} = 2 \times 10^{13}$ neutrons $\text{s}^{-1} \text{cm}^{-2}$, $\phi_{epi} = 5 \times 10^{11}$ neutrons $\text{s}^{-1} \text{cm}^{-2}$ and $\phi_f = 5 \times 10^{12}$ neutrons $\text{s}^{-1} \text{cm}^{-2}$, calculations show that the iodine mixture becomes more suitable: after irradiation during 3 hours, the fraction of ^{126}I atoms and ^{127}I atoms in the iodine mixture is only 8×10^{-5} and 5×10^{-9} , respectively, and thus the abundance of ^{125}I is practically 100%. Further optimization on the ratio of neutron fluxes is likely to yield an even lower abundance of ^{126}I in the iodine mixture. Therefore, these findings are in agreement with data from Amersham (1999), where it is stated that “the ^{126}I content (in carrier-free ^{125}I) is normally less than $0.005\% = 5 \times 10^{-5}$ ”.

The short irradiation time can be achieved by using a loop for the ^{124}Xe supply, while extracting the iodine in a continuous process or in batches. When irradiation continues for a longer time period in the order of days, the iodine mixture gradually becomes less suitable, predominantly as a result of increasing ^{127}I abundance (as is the case for irradiation with HFIR neutron fluxes, see Figure 7.2).

7.4 ^{125}I photon yield in an IOBT source

The ^{125}I radionuclide can thus be obtained with high purity by means of neutron activation of ^{124}Xe . Its overall abundance in the source material f_i will however be $< 100\%$ and depends not only on neutron activation conditions, but also on the quality of the chemical purification of the iodine. But f_i will in particular decrease because a carrier material must be used instead of pure iodine: the latter has a melting point of 113.5°C (data from Weast et al. (1980)), whereas the restriction by Nucletron (1997) states that the melting point of the source material should be higher than 600°C .

7.4.1 Influence of a carrier on ^{125}I abundance and self-absorption

Sodium iodide (NaI), with a molar mass $M = 149.9 \text{ g mol}^{-1}$ and mass density $\rho = 3.67 \text{ g cm}^{-3}$, is a well-known iodine compound with a melting point of 661°C . Sodium has the advantage of a relatively low atomic number ($Z = 11$), which implies low attenuation of the ^{125}I photons with $E \sim 30 \text{ keV}$. The small Na atom also enables a large amount of iodine atoms in the

available source volume. The value for f_1 is given by the ratio of the number of atoms per unit volume in NaI and pure ^{125}I , which is proportional to ϕ/M . With a relative atomic weight of 126.9 for iodine, this ratio is thus given by $f_1 = (3.67/149.9) / (4.93/126.9) = 0.63$.

The carrier also influences self-absorption in the source material. The latter was assessed by means of EGS4 simulations; f_2 is quantified as the relative decrease in dose at the target distance of $r = 1$ cm from the source centre, using the geometrical model of the new design of the microSelectron-HDR V2 source capsule (see section 6.5.5 and Figure 6.12). The used EGS4 input values were discussed in section 6.5.5.

Dose distributions about a source emitting photons with $E = 35$ keV (the energy of the gamma line from ^{125}I) were compared for three cases: (a) an isotropic point source at the centre of the source volume, that is filled with water, (b) the source volume filled with radioactive NaI, and (c) the source volume filled with radioactive pure iodine. Results for radial depth-dose curves are shown in Figure 7.3.

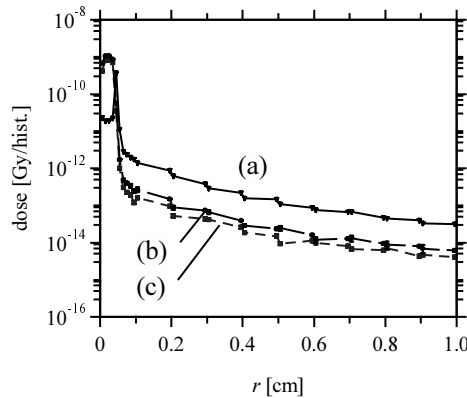


Figure 7.3 Radial depth-dose curves for a source, emitting photons with $E = 35$ keV, from EGS4 simulations, for three cases: from top to bottom, (a) an isotropic point source at the centre of the source volume, that is filled with water, (b) the source volume filled with radioactive sodium iodide, and (c) the source volume filled with radioactive pure iodine.

The curves (b) and (c) show high dose deposition up to $r = 0.375$ mm which corresponds to strong photon absorption in the sodium iodide and pure iodine, respectively, and the walls of the source capsule. As a consequence, these curves are considerably lower in the therapeutic region than curve (a), by about 80% and 90%, respectively. So, although there is less self-absorption in NaI than in pure iodine, the resulting decrease in therapeutic dose is (very) high and a value f_2 ($E = 35$ keV) = 0.8 is derived.

7.4.2 Feasibility of ^{125}I as an IOBT source

The therapeutic requirement from equation (7.5) can now be quantified for ^{125}I , with NaI as source material: the effective source activity $A_{eff}(E) = A_c \cdot f_1 (1 - f_2) = 3.79 \times 10^{12} \times 0.63 \times (1 -$

$0.8) = 0.48 \times 10^{12}$ Bq. As a consequence, $\Sigma(A_{eff} \gamma(i) / A_{int}(E_i)) = 0.15$, which is significantly lower than 1. The final conclusion is that ^{125}I does *not* meet the therapeutic requirement in equation (7.5) for an IOBT source. We continue the feasibility analysis by assessing whether the abundance of ^{126}I in NaI is acceptable, i.e. we determine the shielding possibilities for the high energy ($E > 100$ keV) photons.

7.5 Shielding of photons from ^{126}I

The maximum specific activity of ^{126}I is given by $S_{max} = 2.967 \times 10^{15}$ Bq g $^{-1}$, with $\lambda = 616 \times 10^{-9}$ s $^{-1}$ and $M = 125$ g mol $^{-1}$. With $V_s = 1.2$ mm 3 and $\rho = 4.93$ g cm $^{-3}$, it follows that $A_c = 17.55 \times 10^{12}$ Bq for ^{126}I . It is known from section 7.3.2 that the minimum ^{126}I content in ^{125}I can be as low as 5×10^{-5} , and together with the 63% abundance of iodine in NaI, it follows that $f_I = 0.63 \times 5 \times 10^{-5} = 3.2 \times 10^{-5}$ for ^{126}I . By interpolating the data $A_{all}(E)$ for the energies of the gamma photons from ^{126}I , it follows that $\Sigma(\gamma(i) / A_{all}(E_i)) = 1.46 \times 10^{-9}$ Bq $^{-1}$, and $f_I A_c \Sigma(\gamma(i) / A_{all}(E_i)) = 0.82 < 1$. The ^{126}I in ^{125}I is acceptable, as the 18% margin will continue to increase after irradiation has been terminated, due to the difference in half-life between ^{126}I and ^{125}I ($t_{1/2} = 13.02$ and 60.14 days, respectively).

Study III , Chapters 8 - 10

**Design of an X-ray setup for a
multiphase flow metering device**

Multiphase flow metering based on photon absorption

In Chapters 8 through 10 we present results from the third study in this thesis, on a new application of radiation in the field of industrial monitoring. The study was performed by request of and in cooperation with Shell International Exploration and Production B.V., Rijswijk, The Netherlands (hereafter: Shell), and in cooperation with Daniel Europe Ltd., Larbert, Stirlingshire, Scotland (hereafter: Daniel Europe Ltd). In addition, financial support from BTS through the Ministry of Economic Affairs (Ministerie van Economische Zaken) has been obtained.

8.1 Introduction

The challenge in the joint project was to design a multiphase flow metering (hereafter: MPFM) device that measures the composition of oil/water/gas mixtures flowing through an oil pipeline, based upon the physical principle of photon absorption. The device should contain an X-ray tube instead of a radioactive source and should also be able to perform an integrated determination of water salinity.

In this chapter we discuss a) the theory of multiphase flow composition metering based on photon absorption, (b) the technique of the device that is used at present and c) the requirements on the X-ray MPFM device. Results from simulations are presented, performed by Bom et al. (2000) on the sensitivity and accuracy aspects of the different MPFM principles (with and without integrated determination of water salinity, see section 8.4.1). These results are used in Chapters 9 and 10 for the modelling of different types of X-ray setups in order to assess the optimal design.

8.2 The Dual Energy Gamma Ray Absorption principle

The transmission of a narrow, parallel beam of photons with energy E through an with thickness t (path length of the radiation) is described by Knoll (1967) as:

$$I(E) = I_0 \exp(-\mu(\rho, E)t) \quad (8)$$

with I_0 and I the photon intensities before and after absorption, respectively, and μ linear attenuation coefficient in units [cm^{-1}], depending on the mass density ρ and the energy E . The dependency on ρ is eliminated by using the mass attenuation coefficient in units [$\text{cm}^2 \text{g}^{-1}$].

Likewise, if transmission takes place through a pipe containing a mixture of oil, gas, the intensity $I(E_i)$ is given by:

$$I(E_i) = I_v(E_i) \exp\left(-\left[\left(\frac{\mu}{\rho}\right)_o(E_i)\right] \rho_o \alpha_o + \left[\left(\frac{\mu}{\rho}\right)_w(E_i)\right] \rho_w \alpha_w + \left[\left(\frac{\mu}{\rho}\right)_g(E_i)\right] \rho_g \alpha_g\right) \cdot t \quad (8)$$

where $I_v(E_i)$ is the photon intensity after attenuation in the evacuated pipe, and α and ρ are the volume fractions and mass densities of the mixture components. The subscripts o , w and g refer to oil, water and gas, respectively.

The technique of the multiphase composition meter that is currently being used is called Dual Energy Gamma Ray Absorption (hereafter DEGRA) as two different

as the intensity for energy E_i after attenuation in a pipe that is completely filled with oil ($x_o = 1$). Similar equations hold for water and gas, these matrix elements being derived from calibration measurements. Once these are known, from the intensities $I(E_1)$ and $I(E_2)$ the three fractions are derived, provided the matrix is non-singular.

8.3 The DEGRA meter

Individual oil, water and gas volume fractions determined by DEGRA are combined with measurements of pressure, temperature and total fluid mass or volume flow rate. Combining volume fractions and volume flow rate results in the individual oil, water and gas flow rates.

The previously developed DEGRA composition meter has been tested in several field trials, e.g. discussed by Scheers (1995) and Slijkerman (1995). It makes use of an ^{241}Am source emitting X-rays with energies $E = 13.9, 17.8$ and 20.8 keV, and gamma rays with $E = 26.3$ and 59.5 keV, with relative intensities 0.18, 0.26, 0.06, 0.03 and 0.47 respectively. Although the use of only 2 energies would suffice, as discussed in section 8.2, all energies are included in the spectral analysis in order to derive the multiphase flow composition. Van Santen et al. (1995) discuss the selection of photon energies for DEGRA. A schematic picture of the set-up of the DEGRA composition meter is presented in Figure 8.1.

The optimum fluid path length for measurement of the oil, water and gas fractions with the ^{241}Am source is in the order of 15-20 mm. However an inner diameter of 15 mm for pipelines in the field would be too small to handle the production, as discussed by Scheers (1995). Therefore, a concentric venturi is used in the design (allowing the absorption path length to be selected independently), with a conical body containing the ^{241}Am source in the centre of the flow. In order to maintain acceptable transmission for the lowest energies, two concentric low radiation absorption cylinders, each having a 2 mm wall thickness, have been used as transparent windows, as discussed by Scheers (1994). The composition meter set-up furthermore consists of a dual area Si solid state detector with a thickness of 300 μm and an area of 100 mm^2 for the isolated 59.5 keV gamma peak and an area of 14 mm^2 with higher energy resolution for the lower energy peaks.

The DEGRA meter has been commercialised through a license agreement by Daniel Europe ltd. For more information: <http://www.daniel.co.uk/megra/default.html>.

8.4 X-ray composition meter requirements

Because of the reasons mentioned in section 1.3, Shell aims at development of a MPFM device with an X-ray tube instead of a radioactive source. A number of requirements on the X-ray composition meter is mentioned here, whereas an elaborate discussion is given by Hoppenbrouwers (1996).

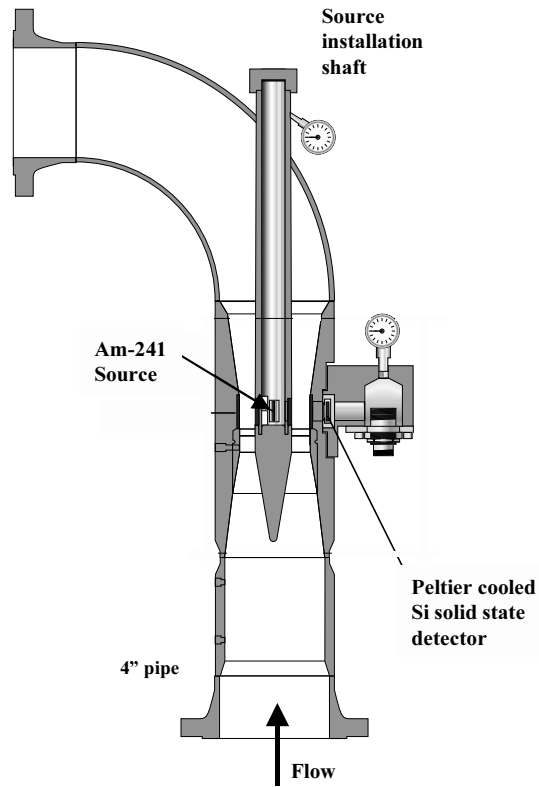


Figure 8.1 Schematic drawing of the set-up of the developed DEGRA composition meter. A concentric venturi is used in the design, with a conical body containing the ^{241}Am source in the centre of the flow. In order to maintain acceptable transmission for the lowest energies, two concentric low radiation absorption cylinders each having a 2 mm wall thickness, have been used as transparent windows.

The X-ray tube in the MPFM composition meter should be operated at a voltage ≤ 100 kV corresponding licensing requirements are far more relaxed compared to higher voltages.

Volume Fraction (hereafter: GVF) environment up to 20-30%, where the multiphase mixture can be approximated with a homogeneous flow model, i.e. assuming no *velocity slip* between the gas and liquid phases. The flow composition may vary rapidly both in time and space, depending on the specific flow regime, as discussed by Hoppenbrouwers (1996). Additional mixing devices in the flow system may therefore be needed to remove the velocity slip and guarantee the homogeneity of the oil/water/gas mixture. The multiphase flow temperature varies typically between 20 and 80 °C, the pressure varies between 0.1 and 10 MPa, and liquid flow rates are in the order of $2,000 \text{ m}^3 \text{ day}^{-1}$ with a GVF of maximum 25-30%, as discussed by Hoppenbrouwers (1996).

8.4.1 Salinity

The water component in the multiphase flow either originates from the oil reservoir itself or is injected into the latter with the purpose of improving the oil extraction from the field. The production water generally contains salts which influence the composition measurement by increased absorption of photons. The salt is either from the underground rocks or present in the injected water. The salinity (i.e. the salt concentration in the water) in the water injected into the reservoir can change over time and the salt concentration can furthermore be different from well to well. The salinity of the production water is therefore not necessarily constant and may have values up to saturation at approximately 300 kg m^{-3} . The salt in the production wells mainly consists of NaCl, with other contributions within a few percent from Ca, Mg, K and SO_4 . Traces of heavy metals like Ba, Sr and Fe are found in production water as well, as discussed by Hoppenbrouwers (1996).

Bom et al. (2000) describe how the mass density of the saline water increases linearly with salt concentration:

$$\rho_{sw} = \rho_w + R \cdot S \quad (8.5)$$

where S represents *salinity*, i.e. the partial density of salt in the saline water in units $[\text{kg m}^{-3}]$. The rate of increase of mass density R is different for every kind of salt and is in the range $[0.6 - 0.9]$. The subscripts w and sw refer to fresh water and saline water, respectively.

8.5 Feasibility of integrated salinity determination

Bom (1999, et al. 2000) reported on the feasibility of an integrated determination of water salinity by the composition meter. It will be now discussed in brief.

8.5.1 The Multiple Energy X-ray Absorption principle

An extension to the DEGRA technique is the attenuation measurement of photons at an additional third energy in order to derive water salinity. However, since the salts are dissolved in the production water and as such do not represent a separate volume fraction, equation (8.3)

must be modified to include salinity. Bom et al. (2000) discuss how the linear attenuation coefficient of saline water at energy E_i can be calculated as:

$$\mu_{sw}(\rho_{sw}, E_i) = \mu_w(\rho_w, E_i) + \left[\left(\frac{\mu}{\rho} \right)_{s,i} - (1-R) \left(\frac{\mu}{\rho} \right)_{w,i} \right] \cdot S \quad (8.6)$$

The subscript s refers to salt. The set of equations that describes the so-called Multiple Energy X-ray Absorption (hereafter: MEXA) concept then becomes:

$$\begin{bmatrix} \mu_{o,1} & \mu_{g,1} & \mu_{w,1} \\ \mu_{o,2} & \mu_{g,2} & \mu_{w,2} \\ \mu_{o,3} & \mu_{g,3} & \mu_{w,3} \\ 1 & 1 & 1 \end{bmatrix} \begin{bmatrix} \left[\left(\frac{\mu}{\rho} \right)_{s,1} - (1-R) \left(\frac{\mu}{\rho} \right)_{w,1} \right] \\ \left[\left(\frac{\mu}{\rho} \right)_{s,2} - (1-R) \left(\frac{\mu}{\rho} \right)_{w,2} \right] \\ \left[\left(\frac{\mu}{\rho} \right)_{s,3} - (1-R) \left(\frac{\mu}{\rho} \right)_{w,3} \right] \\ 0 \end{bmatrix} \cdot \begin{pmatrix} \alpha_o \\ \alpha_g \\ \alpha_{sw} \\ S \cdot \alpha_{sw} \end{pmatrix} = \begin{pmatrix} -\frac{1}{t} \ln \frac{I}{I_v}(E_1) \\ -\frac{1}{t} \ln \frac{I}{I_v}(E_2) \\ -\frac{1}{t} \ln \frac{I}{I_v}(E_3) \\ 1 \end{pmatrix} \quad (8.7)$$

where $\alpha_{o,i} = \alpha_o(\rho_o, E_i)$ denotes the linear attenuation coefficient of oil at energy E_i . Similar equations hold for water and gas. The attenuation coefficients in the matrix are derived from calibration measurements and the last equation describes that the pipe is completely filled with oil, saline water and gas: $\alpha_o + \alpha_{sw} + \alpha_g = 1$. However, since the vector with the volume fractions contains the product $S \cdot \alpha_{sw}$, the set of equations is not linear. This has important consequences for the applicability of the MEXA concept, as is explained in section 8.5.4.

8.5.2 Parametrization of photon-matter interaction

For reasons of throughput in oil production, the required flow rates dictate a minimum radiation path length t in the multiphase flow that was anticipated to be in the order of 4 cm, as argued by Frieling (1999).

This restriction implies a lower limit for the useful photon energy of ~ 20 keV: the absorption of photons with energies below this value becomes very strong and as a consequence, the detector should handle a very large range of count rates; in other words, the difference in count rate between a) dense flow mixtures with a large fraction of saline water and b) more transparent mixtures with higher gas fractions becomes very large. This makes it

$$\mu = \sigma + \tau \quad (8.8)$$

In Figure 8.2, linear attenuation coefficients are shown for the different materials that attenuate photons in a MPFM device, for photoelectric and Compton effect, using data from the well established GEANT package, for which we refer to Brun and Carminati (1994). In the figure it is evident that both of these effects each have their own energy dependence; the latter is functionally nearly identical for all materials involved. All curves in Figure 8.2 relating to the same type of photon-matter interaction have nearly the same shape and are simply scaled in magnitude (along the y-axis) depending upon the type of material.

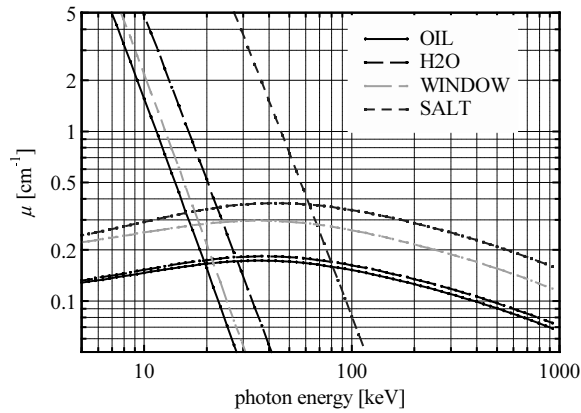


Figure 8.2 Linear attenuation coefficients for different materials that attenuate photons in a device, for photoelectric (straight) and Compton effect (curved), using data from the well established GEANT package. The legend text WINDOW refers to the low radiation absorption cylinders in the pipe construction. Curves relating to the same type of photon-matter interaction have nearly the same shape and are simply scaled in magnitude (along the y-axis) depending upon the type of material.

8.5.3 Analytical solution

The analytical solution to the parametrized system is discussed by Bom (1999), presenting elaborated expressions for C_p and C_c and where, by substituting (8.9) into (8.7), the first three equations reduce to the following expression for the attenuation of energy E_i by a pipe filled with oil, saline water and gas:

$$-\ln \frac{I(E_i)}{I_0} = P\pi(E_i) + Q\gamma(E_i) \quad (8.10)$$

The left-hand term describes the attenuation as a function of energy. P and Q are elaborate expressions containing, besides the unknown fractions x_o , x_w , x_s and x_g , only 'known' terms such as C_p and C_c coefficients, mass densities etc. The important conclusion is that the number of relevant parameters which can be determined from X-ray absorption is related to the number of underlying physical processes and *not* to the number of energies E_i at which absorption is measured.

Since only photoelectric absorption and Compton scattering play a part in the attenuation of photons, two equations are available for the parameters. Together with the third equation that states that the pipe is completely filled, only three of the four fractions (oil, saline water and gas) can be determined. Therefore, increasing the number of energies can give more accurate results in the analysis, as is discussed in section 8.5.4, however it does not allow for more fractions to be derived. This means that when oil, water and gas fractions need to be determined, the salinity can *not* be derived and should be assessed by an independent measurement.

8.5.4 Sensitivity of MEXA analysis (I)

The key assumption made in obtaining the above results is in equation (8.7), stating that the energy dependence of the absorption is independent of the material (atomic number). There are however very small influences of the material on the energy dependence functions $\tau(E_i)$ and $\gamma(E_i)$ for real attenuation coefficients. This means that integrated salinity determination might in principle still be possible, but that, because deviations are very small, intensities have to be determined with extremely high accuracy. This is in agreement with an analysis by Scheers and Slijkerman (1996), from which we quote: "It can be shown that the inverse of the matrix ... is poorly conditioned such that small measurement errors in I_m (intensity) may lead to large errors in the measured phase fractions and salinity."

uncertainty of 3×10^{-4} . This quantitative sensitivity has also been confirmed by independent research by Miller (1999b), who performed analytical calculations on MEXA.

The use of additional energies, especially those with $E < 20$ keV, relaxes the allowed uncertainty to values higher than 1×10^{-4} , as discussed by Bom et al. (2000) for the analysis of a flow mixture with oil, water, gas fractions and salinity of respectively 0.3, 0.6, 0.1 and 100 kg/m^3 ; when composition analysis is performed for a radiation path length $t = 4$ cm and with *four* different energies, the lowest of which is $E = 17$ keV, a maximum allowed uncertainty of 4×10^{-4} in one of the line intensities results in an oil fraction error of 1%. The energies were optimized to obtain the most accurate composition analysis. However, when *six* energies are used, the lowest of which is $E = 17$ keV, this uncertainty becomes 8×10^{-4} . If the lowest of *six* energies is chosen $E = 15$ keV, and the radiation path length is assigned a value $t = 3$ cm in order to achieve acceptable transmission for this energy, the uncertainty becomes 1.2×10^{-3} . Use of a minimum radiation path length $t < 4$ cm would therefore be preferable, however this is not feasible, as discussed in section 8.5.2.

8.5.5 Conclusions for the feasibility

In general, the mentioned uncertainty comprises a statistical and a systematic part. The statistical error originates from counting statistics, while the systematic error is caused by uncertainties and/or fluctuations in the system response function and the X-ray spectrum shape. Of course both of these errors must meet the criterion stated above. But while the statistical uncertainty can be made arbitrarily small by increasing the measurement time, this is not the case for systematic uncertainties.

Up to now these systematic errors are not considered in practical applications outside the laboratory. In a real X-ray instrument, these include phenomena like aging, high voltage stability, drift, temperature, geometry dependent effects and any systematic errors that are made during spectrum analysis (e.g. background subtraction from peak intensities). Systematic errors will therefore be the limiting factor and it is not believed that unattended stand-alone field systems can attain the required accuracy under rough working conditions outside the laboratory. It was therefore decided to abstain from optimizing the design of the MPFM device for integrated determination of water salinity.

8.6 Optimum X-ray spectra for MEXA

In an MPFM device based on X-ray technology, the X-ray energies as well as their number can within limits be chosen freely, which is a major advantage over a radioactive source with its fixed photon energies. Two energies are sufficient in order to determine the composition of the multiphase flow since salinity is no longer considered a variable to be solved, but inclusion of additional energies in the analysis may lead to more accurate results (which is also the case for integrated determination of salinity, see section 8.5.4). This optimization of

X-ray energies for MEXA was studied by Bom and reported in detail by Bom and Cla (2000) and will now be discussed in brief.

8.6.1 Analysis

When water salinity is known, the linear attenuation coefficient $\mu_{sw}(\rho_{sw}, E)$ and mass density ρ_{sw} for saline water can be calculated, as discussed by Bom (1999). The equations in (8.7) reduced to a 3x3 matrix describing a linear system with components oil, saline water and gas for which the attenuation of energy E_i can be written as follows:

$$\ln \frac{I_i}{I_0} = (\mu_o(\rho_o, E_i) - \mu_g(\rho_g, E_i)) \cdot \alpha_o + (\mu_{sw}(\rho_{sw}, E_i) - \mu_g(\rho_g, E_i)) \cdot \alpha_{sw} + \mu_g(\rho_g, E_i) \cdot \alpha_g \quad (8.11)$$

This system was solved with two and three energies E_i for the two unknowns α_o and α_{sw} , and α_g which can be determined by the equation $\alpha_o + \alpha_{sw} + \alpha_g = 1$.

8.6.2 Monoenergetic X-rays

An important similarity between MEXA analysis with and without integrated salinity determination is the sensitivity to the correct photon intensities. Bom et al. (1998) conclude that it is therefore very important that *monoenergetic* X-rays are used in MEXA (instead of energy bands or the entire spectrum), as their intensities are much easier to derive from measured spectra.

Monoenergetic photons in principle enable detection with high count rates in scintillation detectors in pure counting mode, up to 10^7 counts s^{-1} , which is possible because no energy resolution is required and the detector signal does not have to be integrated. These high count rates result in small statistical fluctuations in detected intensities (0.03%), which is essential for correct composition measurement (see section 8.5.4).

If energy bands are to be used, these must be extracted from the bremsstrahlung spectrum

fitting the entire spectrum. These are complex procedures that again require the X-ray spectrum and the detector response function to be accurately known and stable during operation, which will cause different systematic errors.

8.6.3 Sensitivity of MEXA analysis (II)

The correct multiphase flow fractions are derived from the set of equations (8.11) if the intensities and attenuation coefficients are known with infinite accuracy (no error). In reality however, this is not the case since: (1) intensities are characterized by a statistical uncertainty due to the nature of radiation processes, (2) there is a systematic uncertainty caused by the way the peak intensities are extracted from the X-ray spectrum and (3) for the components in the fluid there are uncertainties in the properties ρ and α .

The sensitivity of MEXA analysis was quantified by the *oil fraction error*, defined as the deviation between the derived fraction and the true value, when spectrum peak intensities are disturbed by their statistical error. The oil fraction error is calculated as the square root of the sum of squares of the errors resulting from the disturbance of every single peak intensity in turn.

The source spectrum is assumed to consist of two or three distinct energy peaks (the highest of the three energies fixed at 70 keV) on a low (20% of the total intensity), constant background up to 100 keV, and is used in a simulation model that includes a detailed construction of the detected spectrum in a 500 μm thick Si detector (see section 10.5.2). The derived peak intensities are used for the MEXA analysis. This is discussed in detail by Bom and Clarijs (2000). The important conclusion from this study is that the two-energies case is preferable since the oil fraction errors are significantly lower than in the three-energies case. The three-energies scenario furthermore effectively reduces to the two-energies case with increasing absorption, as the middle of the three energies tends to approach the lowest energy. Apparently, the use of three energies does not provide enough *extra* absorption-specific information to compensate the larger uncertainties in the detected spectrum. Only inclusion of a very low third energy (< 20 keV) is advantageous as absorption coefficients curves diverge from one another with decreasing energy, but this value is outside the energy range 20-60 keV to be used (see section 8.5.2).

8.6.4 Optimum set of energies

Finally, the optimum set of energies is defined as those energies for which the oil fraction error is minimal, over the range of all relevant energy sets, oil-, water-, and gas fractions and salinity. At this optimum, the system is least sensitive to line intensity deviations. It is in this

at 50 keV, cf. section 10.5.2. The intensities are 1.2×10^5 photons s^{-1} for 21 keV and 1.2×10^6 photons s^{-1} for 49 keV. These values are chosen such that the total intensity of the detected spectrum is limited to 10^5 counts s^{-1} , which is considered the maximum count rate of the full spectrum that can be handled. The continuum background in the spectra should be as low as possible. With a count rate of 10^5 counts s^{-1} , the corresponding relative oil fraction error is then within 3.1%, depending on the specific multiphase flow composition, as discussed by Bom and Clarijs (2000). In general, disturbance of the line intensities with 1% of the peak contents results in an oil fraction error of 1-2%, which is considered acceptable, as discussed in section 8.4.

These optimum energy values have been used in the prototype design of the MPFM device, as is discussed in section 10.5. In the next two chapters however, we also present results from studies on X-ray spectra with peaks at *different* energies, as these spectra were generated for MEXA analysis with integrated determination of salinity, the feasibility of which was still a subject of study at that time (see section 8.5.5).

9 Transmission Secondary Fluorescence X-ray Spectra

Having specified the ideal X-ray spectra for MEXA, the different types of X-ray set-ups in order to try to generate these spectra are now discussed. These have been studied by means of EGS4 simulations. The simulation models of the X-ray tube are presented, along with specific features of the EGS4 code that are essential for generating realistic X-ray spectra. In this chapter we address the first, so-called Transmission Secondary Fluorescence X-ray set-up; the optimized spectrum is determined with simulations and a comparison with measurements is made. We first explain the physical principle and the type of X-ray set-up that is anticipated to yield suitable spectra.

9.1 Rationale of the Transmission Secondary Fluorescence X-ray set-up

9.1.1 The primary X-ray spectrum

In section 8.6 we concluded that successful MPFM requires X-ray spectra that consist of monoenergetic peaks on a low continuum background. A typical X-ray spectrum, depicted in Figure 9.1, is generated when electrons are incident on a heavy target material. This spectrum is the result of an EGS4 simulation of 120 keV electrons incident on a tungsten target in a side-window X-ray tube.

The main contribution in the spectrum is a continuous distribution, the so-called bremsstrahlung (see section 9.2.2) that is emitted when electrons are decelerated in the anode. The decrease of intensity at the low energy side is caused by absorption of the bremsstrahlung in the target itself. Besides the bremsstrahlung continuum, the spectrum contains the tungsten characteristic X-ray peaks that correspond to differences in binding energy for the various atomic shells (K, L, M, etc.). In Table 9.1 K binding energies and characteristic radiation energies for the different elements are presented, that have been used in the EGS4 simulations. These are taken from Lederer et al. (1978), to which we refer for more information on characteristic X-rays and the conventional nomenclature used.

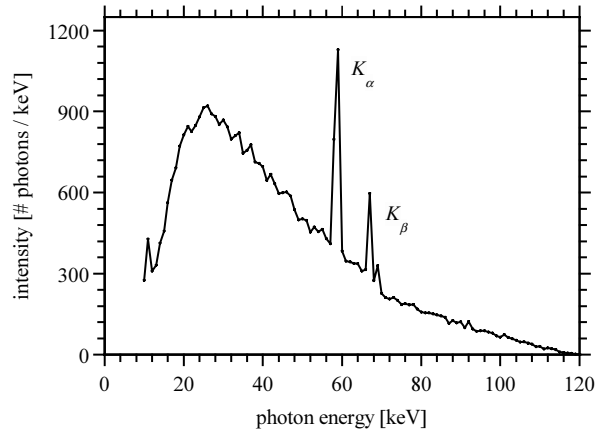


Figure 9.1 The result from an EGS4 simulation for the X-ray spectrum of 120 keV electrons incident on a tungsten target in a side-window X-ray tube.

Based upon the conclusions from section 8.5.4, a typical X-ray spectrum as depicted in Figure 9.1 is not suitable for MPFM. The contribution of the bremsstrahlung continuum is much too high and the intensity of the tungsten fluorescence peaks is only a few percent of that of the total spectrum (~5% for the integrated K_{α} fluorescence intensity).

Table 9.1 K binding energy and characteristic radiation energies for the different elements used in the simulations.

Z	Element	K binding energy [keV]	$K_{\alpha 2}$ [keV]	$K_{\alpha 1}$ [keV]	$K'_{\beta 1}$ [keV]	$K'_{\beta 2}$ [keV]
4	Be	0.112	-	0.108	-	-
13	Al	1.56	1.49	1.49	1.56	-
14	Si	1.8	1.7	1.7	1.8	-
28	Ni	8.33	7.46	7.48	8.26	-
30	Zn	9.7	8.6	8.6	9.6	9.6
40	Zr	18.0	15.7	15.8	17.7	18.0
42	Mo	20.0	17.4	17.5	19.6	20.0
47	Ag	25.5	22.0	22.2	24.9	25.5
48	Cd	26.7	23.0	23.2	26.1	26.6
52	Te	31.8	27.2	27.5	31.0	31.7
62	Sm	46.8	39.5	40.1	45.4	46.6
74	W	69.5	58.0	59.3	67.2	69.1
79	Au	80.7	67.0	68.8	78.0	80.1

9.1.2 Rationale of secondary fluorescence

The aim was to design an alternative X-ray set-up that yields spectra with the main intensity contribution consisting of fluorescence peaks and an effective reduction of bremsstrahlung continuum, i.e. a high peak/continuum ratio.

This can be achieved by conversion of the bremsstrahlung continuum into secondary fluorescence radiation via the principle of photo-ionization. In this process, an atomic electron is removed from an inner shell after impact with a bremsstrahlung photon. After the vacancy is filled by an electron from an outer shell, either an Auger electron or a fluorescence photon is emitted, the latter with an energy equal to the difference in binding energy between the two shells. The probability for X-ray emission is given by the fluorescence yield ω_K (for K fluorescence photons). In this context, fluorescence X-rays $K_{\alpha 1}$, $K_{\alpha 2}$, $K_{\beta 1}$ and $K_{\beta 2}$, corresponding to transitions between shells $K - L_3$, $K - L_2$, $K - M_3$, $K - N_{2+3}$ respectively, are considered since only these are emitted with significant intensity, as discussed by Lederer et al. (1978). The other process that leads to emission of fluorescence radiation is electron impact ionization, which is discussed in section 9.2.3.

9.1.3 Rationale of an end-window X-ray tube

In the Transmission Secondary Fluorescence X-ray (hereafter: TSFX) set-up, depicted in Figure 9.2, secondary foils are irradiated with the primary (i.e. emitted by the anode) X-ray continuum, effectively absorbing the bremsstrahlung and converting it into secondary fluorescence radiation via photo-ionization.

The efficiency for creation of bremsstrahlung is very low, in the order of 1% for 100 keV electrons incident on a tungsten target (see section 9.2.3). In order to restrict the geometrical loss, the foils must be irradiated from as close a distance as possible. Such a compact geometry is easier to achieve with an end-window (or transmission type) X-ray tube; the secondary fluorescence foils can then be attached to the end-window of the tube that is integrated with the anode, thus ensuring effective irradiation, whereas in a side-window (or reflection type) X-ray tube, the anode and exit window are not integrated, resulting in a separation in the order of centimeters (see section 9.6.1).

9.2 Simulation of a TSFX set-up

A schematic picture of a TSFX set-up is presented in Figure 9.2. The anode or target (indicated by 1) on the left side is bombarded with electrons that are accelerated in the X-ray tube. The generated bremsstrahlung continuum is absorbed by the foils (indicated by 2) and converted (via photo-ionization) into fluorescence radiation that is emitted isotropically by nature. Part of this fluorescence radiation escapes the foils in the direction of the oil pipe that contains the multiphase flow (indicated by 4), is transmitted through its low radiation

absorption window (indicated by 5) and detected in the detector system on the right side (indicated by 6).

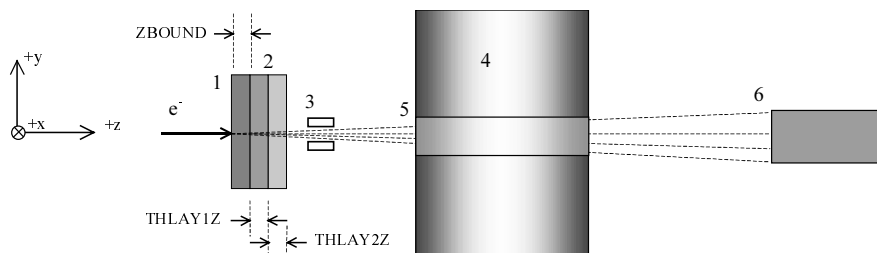


Figure 9.2 Schematic side view picture of a TSFX set-up. Components: anode (1), secondary foil materials (2), collimators (3), oil pipe and multiphase flow (4), low radiation absorption window (5) and detector system (6).

The only components that have been implemented in the EGS4 simulations are the anode and the two foil materials, while the other components (oil pipe, low radiation absorption windows and detector) were included in the simulations performed by Bom (see section 8.6.3), who determined the optimum X-ray spectra for MEXA.

A prototype design will furthermore consist of collimators (indicated by 3) that reduce scattering and ensure a narrow beam geometry, but these were not implemented in the simulation model. Beryllium windows in the X-ray tube or detector system were also not included in the simulations as these do not significantly influence the shape and intensity of the spectra: the attenuation of a Be window thickness of 1 mm is in the order of a few % for energies in the range 20-60 keV.

We furthermore assigned the following input values to the radiation transport parameters in the simulation program: ESTEPE=0.05, ECUT=0.521 MeV, PCUT=0.010 MeV, UE=0.611 MeV, UP=0.1 MeV*. We refer to section 2.6 for more information about these parameters.

9.2.1 The anode

In a TSFX spectrum, the monoenergetic peak with the highest energy originates from fluorescence in the anode. By nature, fluorescence radiation is emitted as a complex of lines (i.e. $K_{\alpha 1}$, $K_{\alpha 2}$, etc.) with different energies. The anode and foil materials have therefore been selected on the $K_{\alpha 1}$ fluorescence energy (K fluorescence line with the highest yield), that should be close to the optimum values, that were determined by Bom (see section 8.6.4).

Since initial studies with the TSFX set-up were aimed at obtaining spectra with three monoenergetic peaks at 60, 40 and 20 keV, a tungsten anode was chosen, with $K_{\alpha 1} = 59.3$ keV (see Table 9.1). Tungsten is a common choice for an X-ray target, as it has not only a high

* We mention and quantify these specific parameters primarily for those EGS4 experts that are interested in performing similar simulations.

atomic number ($Z = 74$), but a very high melting point (3695 K) as well. The transmission anode in the simulations is characterized by a focal spot with an area of $\sim 1 \text{ mm}^2$ and a thickness of $ZBOUND = 10 \text{ }\mu\text{m}$, sufficient for absorbing 100 keV incident electrons, and at the same time this low value minimizes absorption of the primary X-rays in the anode.

9.2.2 Simulation of bremsstrahlung

When electrons impact on a heavy target material, most of their energy is dissipated into heat and only about 1% is converted into bremsstrahlung. Straightforward generation of bremsstrahlung in EGS4 would therefore necessitate simulation of a very high number of incident electrons and a correspondingly large amount of CPU time. We therefore used a variance reduction technique in order to gain efficiency and ‘speed up’ the simulations.

With this so-called bremsstrahlung splitting technique, the normal electron transport is performed until the point where bremsstrahlung interaction is sampled. Then, instead of creating just one bremsstrahlung photon, an integer number of $NBR SPL$ photons are created with a ‘weight’ $WT = 1/NBR SPL$ relative to the electron’s weight. Both the energy and angular distribution are sampled $NBR SPL$ times and the $NBR SPL$ photons are placed on the particle stack, awaiting individual transportation. In the AUSGAB routine in EGS4 the output X-ray spectra are generated and the weight $1/NBR SPL$ is taken into account, yielding correct normalized intensities. This technique results in X-ray spectra with smaller statistical fluctuations and, unless $NBR SPL$ is assigned a value that is too high, the physics of bremsstrahlung generation are not violated. We used splitting factors with values up to $NBR SPL = 400$ and verified consistency with the default algorithm for bremsstrahlung in EGS4.

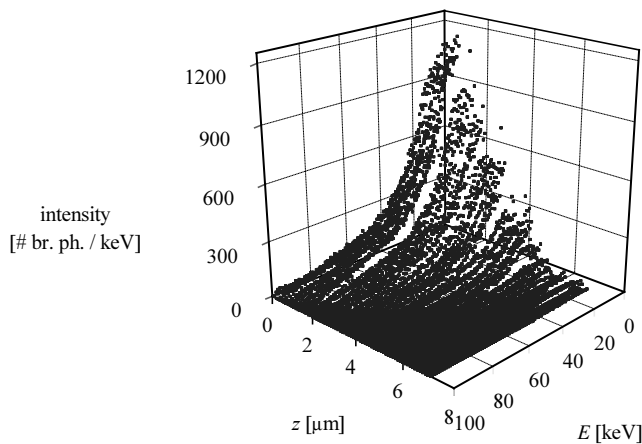


Figure 9.3 Results from EGS4 simulations for the sampling of the energy distribution of bremsstrahlung, for 100 keV electrons as a function of the depth z in a tungsten anode with thickness $ZBOUND = 10 \text{ }\mu\text{m}$. The anode was divided into different z -bins with a thickness of $1.5 \text{ }\mu\text{m}$ in order to facilitate the sampling procedure.

Results from EGS4 simulations on the sampling of bremsstrahlung photons are illustrated in Figure 9.3 for 100 keV electrons, as a function of the depth z in a tungsten anode with ZBOUND = 10 μm . The anode was divided into different z -bins with a thickness of 1.5 μm in order to facilitate the sampling procedure. Simulations indicate that bremsstrahlung photons are created up to a depth of $z \sim 7 \mu\text{m}$, in agreement with an analytical expression from Bos et al. (2000), that predicts an electron range $R = (1/\phi) \times 0.412 \times E^{1.265 - 0.0954 \times \ln E} = 7 \mu\text{m}$, with $\phi = 19.3 \text{ g cm}^{-3}$ and $E = 0.1 \text{ MeV}$.

From the energy distribution we see that bremsstrahlung photons are sampled up to the maximum energy of 100 keV in the first few μm , but as the electrons penetrate at larger depths, they lose more of their initial energy and the maximum bremsstrahlung energy becomes correspondingly lower. The energy distribution in Figure 9.1 is the integrated result for all the generated bremsstrahlung emerging from the anode, after absorption in the latter.

The absorption of X-rays in the anode furthermore depends on the angular distribution of the bremsstrahlung photons. In the current version of EGS4 (4.3), the so-called 2BS Koch and Motz angular distribution is used as discussed by Bielajew et al. (1989). The angular distribution behind the anode is eventually determined by multiple scattering of the incident electrons in the anode. As the electrons slow down, correlation with the incident direction is lost and their radiation paths show strong curvature, a process known as ‘straggling’. As a result, bremsstrahlung is emitted in all directions.

The result from simulations on the angular distribution of the radiation emitted at the backside of the anode is depicted in Figure 9.4.

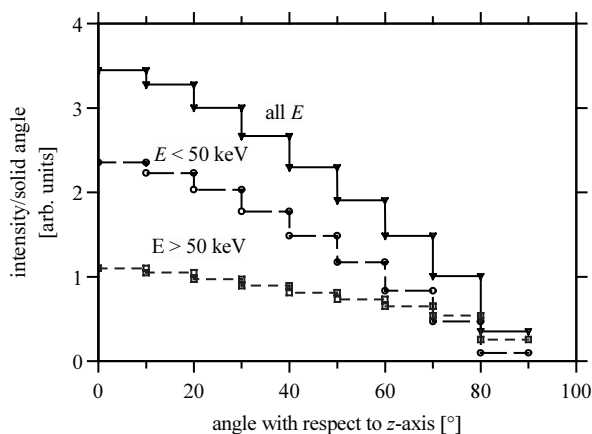


Figure 9.4 Distribution of photons emerging from the backside of the anode, as a function of the angle with respect to the $+z$ -axis (forward direction), per solid angle. The distribution is shown for all energies E integrated (upper curve), energies $E < 50 \text{ keV}$ integrated (middle curve) and energies $E > 50 \text{ keV}$ integrated (lower curve), illustrating the influence of absorption in the anode.

It shows the photon intensity emerging from the backside of the anode, per solid angle, as a function of the angle with respect to the $+z$ -axis (forward direction). The distribution is also

shown for the case the photon energy is restricted to the intervals 0-50 keV and 50-100 keV, respectively, illustrating the influence of absorption in the anode.

The distribution is peaked in the forward direction, especially for $E < 50$ keV, where absorption in the anode is stronger. Nevertheless, only at large angles (> 70 degrees) with respect to the forward direction, the flux of photons with $E > 50$ keV is higher than for photons with $E < 50$ keV.

9.2.3 Electron impact ionization in EGS4

In the process of electron impact ionization (hereafter: EII), inner shell atomic electrons are removed from the atom after direct impact with an incident electron. In photo-ionization the shell vacancy is created by an incident photon. For electrons with $E = 100$ keV that are brought to stop in a thick tungsten target with $Z = 74$, Attix (1986) mentions a value in the order of 1% for the ratio of radiative to total stopping powers; this implies that 1% of the beam energy is converted into bremsstrahlung and about 99% is spent in collision interactions that cause excitation and electron impact ionization in the target.

Although less than 1% of these collisions generates fluorescence X-rays (the rest heats the target), the net contribution is in the same order of magnitude as that of fluorescence caused by photo-ionization. Since we are especially interested in the fluorescence yield, it is important that EII is implemented correctly in EGS4. Namito (2000) provided patches for inclusion of the EII effect in the PEGS4 routine that generates the radiation-matter interaction data, prior to the official implementation of EII in EGS4.

Simulations indicate that inclusion of EII in EGS4 results in an increase of the integrated K fluorescence intensity emitted by the anode by $\sim 30\%$, so indeed this is a significant effect.

9.2.4 The secondary fluorescence foils

The foil materials samarium and silver have been selected upon the K_{α} fluorescence energies, 40.1 keV and 22.2 keV, respectively (see Table 9.1), close to the initial optimum values 40 and 20 keV. The Sm and Ag foils in Figure 9.2 are positioned in order of decreasing atomic number ($Z = 62$ and 47, respectively). This geometry ensures that fluorescence radiation with lower energies, emitted in the direction of the oil pipe and detector, does not suffer absorption in an intermediate material with higher atomic number.

The variables THLAYIZ and THLAY2Z denote the thicknesses of the Sm and Ag foils, the values of which are determined by two conflicting requirements: (a) the foil must be thick enough in order to sufficiently absorb the primary bremsstrahlung that generates the secondary fluorescence, and (b) it should be thin enough in order to reduce the attenuation of the generated fluorescence radiation.

In addition to this, fluorescence radiation originating from the tungsten anode and the Sm foil suffers intermediate absorption in the Sm and Ag foils (part of which once again converts into fluorescence radiation).

Simulations were performed in order to quantify the interplay of the above processes, using foil thicknesses based upon the half value layer thickness $d_{1/2} = \ln 2 / \mu(E)$ in units [cm], for photons with energy E just above the K binding energy, and with μ as the linear attenuation coefficient in units [cm⁻¹]. This value for $\mu(E)$ was chosen as the fluorescence is most efficient for this E . For Sm, $d_{1/2} > 50 \mu\text{m}$ for $E > 46.6 \text{ keV}$, and for Ag, $d_{1/2} > 20 \mu\text{m}$ for $E > 25.5 \text{ keV}$. The range of foil thicknesses used in the simulations was therefore THLAYIZ $> 50 \mu\text{m}$ and THLAY2Z $> 20 \mu\text{m}$.

The dimensions of the foils (and the anode) in x - and y -directions are 1 cm, i.e. larger than those of the detector ($5 \times 5 \text{ mm}^2$, see section 10.5.2). However, the dimensions of the irradiated part of the foils are effectively only within 1 mm in x - and y -direction from the centre of the foils.

9.2.5 Calculation of normalized intensities

The distance between the X-ray tube (and foils) and the position of the detector system was anticipated to be in the order of $\sim 20 \text{ cm}$ (at maximum). Therefore, rather than including the detector at its anticipated position in the simulation code, which requires large amounts of CPU time in order to record spectra with acceptable statistical fluctuations, we used a different method in order to normalize spectral intensities: all photons escaping the foils with an angle $< 10^\circ$ with respect to the forward direction ($+z$ -axis) are recorded, after which a correction is performed for the real solid angle between foil position and detector. For a detector with area $5 \times 5 \text{ mm}^2$ at 20 cm distance, a correction factor 6.4×10^{-3} is thus derived. It has been verified that the angular distribution within this 10° angle is constant within 5%.

Since the use of any mechanical cooling devices was discouraged (see section 8.4), low power consumption is a requirement for the X-ray tube; if we assume a value of 50 W, and given the fact that the tube is operated at a voltage of 100 kV, this corresponds to a tube current of 0.5 mA, or 3.12×10^{15} electrons per second. The simulated number of electrons is scaled to this value.

Finally, correction for bremsstrahlung splitting is taken into account (see section 9.2.2), yielding normalized spectral intensities, that are quantified in the figures by the number of photons per second that strike the $5 \times 5 \text{ mm}^2$ detector surface at a distance 20 cm from the foils, for an X-ray tube operated at 50 W (0.5 mA/ 100 kV).

9.3 Initial results from simulations

In Figure 9.5 we present results from simulation runs on a TSFX set-up with various combinations of Sm and Ag foil thicknesses. A tungsten anode with a thickness of ZBOUND = $10 \mu\text{m}$ was used and 5×10^6 incident electrons were simulated in order to record the spectra. The different values for THLAYIZ and THLAY2Z are indicated in the figure. The spectra are recorded in energy bins of 1 keV, the corresponding intensities of which are connected by the

curves in the graph, rather than depicted as a histogram. This explains why fluorescence lines show up as peaks.

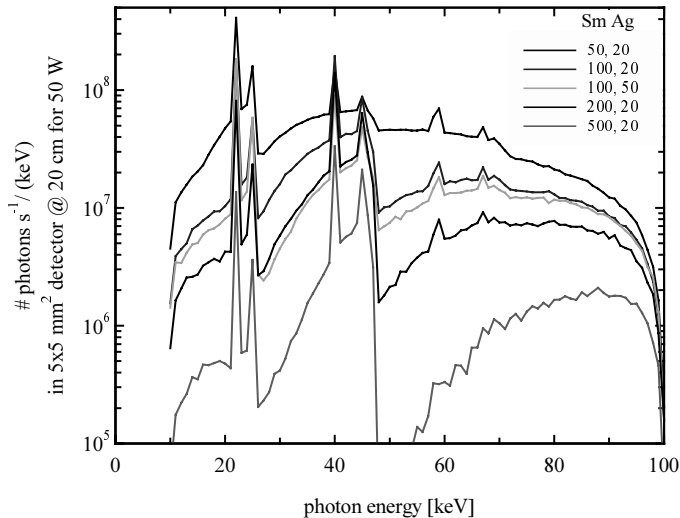


Figure 9.5 Results from simulation runs on various combinations of Sm and Ag foil thicknesses. ZBOUND = 10 μ m and 5×10^6 incident electrons were simulated to record the spectra. The different values for THLAYIZ and THLAY2Z are indicated in the figure, for Sm and Ag respectively, in units [μ m].

The different K fluorescence peaks can be distinguished, however the continuum background contribution is still considerable. Consequently, multi-channel pulse height selection is required; it is not possible to operate in a simple direct counting mode. The maximum count rate of the full spectrum that can be handled is in the order of 10^5 counts s^{-1} (100 kHz) and proved to be sufficient for MEXA analysis (see section 8.6.4). Since the integrated spectral intensities in Figure 9.5 are in the order of $10^8 \sim 10^9$ photons s^{-1} , and taking into account that typical transmission for 20 keV in the oil pipe and multiphase flow is in the order of 10% (depending on multiphase composition), it is evident that photon yields that can be realized with a TSFX set-up are considerably higher than those required.

The intensity of the tungsten peaks is only little higher than that of the background. It is clear that the photo-ionization that generates fluorescence in a ZBOUND = 10 μ m thick anode is not sufficient in order to achieve a high peak/continuum ratio. A thicker anode will lead to increased conversion of the primary X-ray continuum (the part with energies above the tungsten K-binding energy) into fluorescence, resulting in a higher peak/continuum ratio. Due to enhanced absorption, all photon intensities will decrease but, as explained above, this is acceptable.

Increasing the Sm foil thickness THLAYIZ from 50 up to 100 μ m results in higher Sm fluorescence intensity and ditto peak/continuum ratio. A further increase up to 200 μ m leads to a lower Sm fluorescence yield, however the Sm peak/continuum ratio continues to increase,

leaving tungsten and Ag peak/continuum ratios almost unchanged. A thickness of 500 μm results in strong reduction of intensity for all energies.

Increasing the Ag foil thickness THLAY2Z from 20 up to 50 μm results in higher Ag fluorescence intensity and ditto peak/continuum ratio, although all other intensities are slightly reduced. A further increase up to 100 μm does not significantly influence any peak/continuum ratio, but results in lower intensities for all energies (not illustrated).

The results from these initial simulations have been used for further optimization of the TSFX spectrum, which will be discussed in section 9.5. But first we present calculations that are used to verify the order of magnitude of the simulated fluorescence intensities.

9.4 Quantitative verification

More detailed simulations were performed for the TSFX set-up with THLAYIZ = 100 μm and THLAY2Z = 50 μm , in which spectral intensities were recorded at the interfaces of the anode and the Sm and Ag foils. The following calculations are based upon these simulations.

9.4.1 Bremsstrahlung intensity

The integrated bremsstrahlung intensity was calculated based upon the simulated spectra for all photons emerging from the anode in the +z-direction, i.e. with angles between 0 and 90 degrees with respect to this axis. We find a number of 7.8×10^{-3} photons per incident electron after taking into account the average absorption of photons in the anode, i.e. the expected order of magnitude for the efficiency of X-ray generation.

Bertin (1978) discusses another means of verification: an estimate for the integrated bremsstrahlung intensity from an X-ray tube, known as the Beatty formula: $I_{int} = (1.4 \times 10^{-9}) Z i V^2$, with I_{int} the integrated bremsstrahlung intensity in units [W], i the tube current in units [A] and V the tube voltage in units [V]. Although this formula probably applies to a side-window X-ray tube, results are in the same order of magnitude: the Beatty formula predicts $I_{int} = 0.52$ W for an X-ray tube operated at 0.5 mA/100 kV, whereas from simulations we derive a value of 0.16 W.

Attix (1986) presents an approximate equation for the radiant energy of the unfiltered bremsstrahlung in a thick target: $R \cong 1.6 \times 10^{-16} N_e Z T_o^2$ in units [J], with N_e the number of incident electrons, and T_o the incident electron energy in units [MeV]. It follows that $R = 1.2 \times 10^{-16}$ J per incident electron, which corresponds to a value of 0.37 W for a tube current of 0.5 mA. Taking into account that the value 0.16 W from simulations is based upon emitted (filtered) bremsstrahlung, the agreement is reasonable.

9.4.2 Sm K_α fluorescence intensity

From the simulated spectrum of all photons emerging from the anode and entering the Sm foil in the +z-direction, we only consider those photons that contribute to Sm fluorescence, i.e. photons with $E \geq 47$ keV (Sm K-binding energy). For this part of the spectrum, the number of photons that interact in the 100 μm Sm foil via the photoelectric effect is calculated; a number of 4.75×10^{12} photons/s for a number of 3.12×10^{15} incident electrons/s (with the X-ray tube operated at 0.5 mA/100 kV).

The probability of subsequent K-fluorescence emission is given by the fluorescence yield ω_K (see section 9.1.2). For Sm, $\omega_K = 0.93$ (data from Lederer et al. (1978)) and with a relative intensity of 80% for K_α lines, a number of 3.53×10^{12} K_α fluorescence photons with $E = 40$ keV is generated in the Sm foil. Since these are emitted isotropically, a correction factor of 4.82×10^{-5} for the real solid angle between foil and detector area is applied, resulting in a number of 1.70×10^8 K_α fluorescence photons that is set in motion in the direction of the detector.

Since fluorescence is generated throughout the Sm foil, the average attenuation of these photons is approximated by calculating the absorption in a 50 μm Sm layer, from which we derive a transmission $T = 79\%$. Furthermore, these photons suffer absorption in the 50 μm Ag foil, corresponding to $T = 58\%$. As a consequence, the intensity of K_α fluorescence photons that escapes the foils in the direction of the detector with area $5 \times 5 \text{ mm}^2$ at 20 cm distance, is 7.80×10^7 photons/s. Direct results from simulations, as shown in Figure 9.5, yield an intensity of 8.81×10^7 photons/s, a value that is higher by only 13%.

9.4.3 Ag K_α fluorescence intensity

Simulations were performed in order to calculate the number of photons transmitted by the Sm foil and entering the Ag foil in the +z-direction with $E \geq 26$ keV (Ag K-binding energy). The fraction of these photons that interact in the 50 μm Ag foil via the photoelectric effect is calculated; a number of 3.69×10^{12} photons/s for 0.5 mA tube current.

With $\omega_K = 0.83$ and a relative intensity of 83% for K_α lines from Ag, a number of 2.54×10^{12} K_α fluorescence photons with $E = 22$ keV is generated in the Ag foil. The same correction factor of 4.82×10^{-5} for the real solid angle between foil and detector area is applied, resulting in a number of 1.23×10^8 K_α fluorescence photons that is set in motion in the direction of the detector.

This fluorescence being generated throughout the Ag foil, the average attenuation is approximated by taking the absorption in a 25 μm Ag layer, from which we derive a transmission $T = 79\%$. As a consequence, the intensity of K_α fluorescence photons that escape the foils in the direction of the detector with area $5 \times 5 \text{ mm}^2$ at 20 cm distance, is 9.68×10^7 photons/s. Direct results from simulations, as shown in Figure 9.5, yields an intensity of 1.83×10^8 photons/s, a value that is higher by 89%.

Compton scattering in the foils is a qualitative explanation for the observed difference; Compton scattering of the primary X-ray continuum results in an increased contribution of lower energy photons that are scattered over larger angles with respect to the forward direction. Comparing values for σ/ρ and taking into account that the probability for Compton scattering σ is proportional to the mass density ρ , ($\rho = 10.5$ and 7.53 g cm^{-3} for Ag and Sm, respectively), we find that σ is $\sim 50\%$ higher for Ag than for Sm, for $E \geq 26 \text{ keV}$ (Ag K-binding energy). This means that, especially in the Ag, the angular distribution of photons is less peaked in the forward direction and part of the Compton scattered photons travel in directions more parallel to the foil planes.

As a result, the probability of photons interacting via the photoelectric effect also increases and so does the emission of secondary fluorescence. Whereas directional dependence of Compton scattered photons is of course included in the simulations, the calculations are based upon the energy spectrum that enters the Ag foil in the $+z$ -direction, however the angular distribution for these photons is not considered.

9.5 The optimized TSFX spectrum

In agreement with the analysis of initial TSFX spectra in section 9.3, further simulations of the TSFX set-up have resulted in optimum anode and foil thicknesses 100, 200 and 50 μm for tungsten, Sm and Ag, respectively. The corresponding spectrum is shown in Figure 9.6.

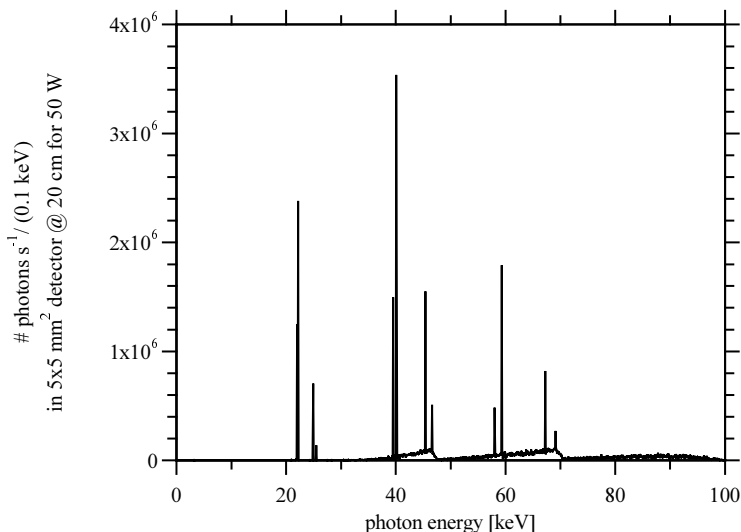


Figure 9.6 Optimized TSFX spectrum from simulations, resulting in optimum foil thicknesses ZBOUND = 100 μm , THLAY1Z = 200 μm and THLAY2Z = 50 μm for W, Sm and Ag, respectively.

An effective tungsten thickness of 100 μm can be achieved by placing an additional 90 μm thick tungsten foil in front of the Sm foil. The user code for the simulations was modified as to record the output spectra in energy bins of 0.1 keV, enabling distinction of the separate K X-ray lines.

The continuum background contribution has decreased considerably with fluorescence peak/continuum ratios now varying between 10 and 100 (even higher for Sm K_{α}). The principle of photo-ionization followed by emission of fluorescence is clearly illustrated by the discontinuities in the background continuum at the K-edges of tungsten and Sm.

Especially tungsten fluorescence has increased considerably compared with Figure 9.5, as a results of enhanced photo-ionization in the 100 μm thick layer. This has also caused all intensities to decrease, but the integrated intensity of 3.81×10^7 photons/s is still higher by more than 2 orders of magnitude than the applicable maximum count rate of 10^5 counts s^{-1} .

9.5.1 MPFM with the optimized TSFX spectrum

At the time the optimized TSFX spectrum was applied in MEXA analysis, integrated determination of salinity was still the aim of the project. Bom concluded from the analysis with the optimized TSFX spectrum that the background continuum contribution in the spectrum hinders the determination of X-ray line intensities with a required accuracy of about $\sim 1 \times 10^{-4}$. Small deviations in detected intensities result in large errors in the component fractions, as was explained in section 8.5.4.

It was therefore decided to study a second, so-called Reflection Secondary Fluorescence X-ray set-up, that should provide spectra with higher peak/continuum ratios. This type of X-ray set-up is discussed in Chapter 10.

9.6 Comparison with measurements

So far, optimization of the TSFX set-up is based upon simulations. An experimental verification of the TSFX simulations was performed by Reimerink (1999). Since an end-window X-ray tube was not available at the time of measurements, the comparison with simulations is based upon the use of a side-window X-ray tube that was available at Shell. Since the technique of accurate measurements of X-ray spectra is described elsewhere in great detail, e.g. by Knoll (1967), here we concentrate on summarizing the experimental conditions and the results.

9.6.1 Experimental set-up

Reimerink (1999) used the following equipment in the measurements (the numbers between brackets refer to the items in Figure 9.7):

- (1) Baltograph CLD 160 side-window X-ray tube (limited to 100 kV, maximum tube current of 4 mA at 100 kV), purchased from Balteau X-ray, Herve, Belgium, consisting of CRX 100/15 tube and TSD 100/0 tube housing, (2) 1.5 mm thick tungsten target (with 20 degrees target angle and a focal spot size of $0.6 \times 0.6 \text{ mm}^2$) and (3) a Be exit window ($\varnothing 15 \text{ mm}$, 900 μm thickness).
- (4) Amptek XR-100T-CdZnTe detector ($3 \times 3 \text{ mm}^2$ area, 2 mm thickness, operated at 400 V) with preamplifier.
- Canberra 2026xx shaping amplifier, modified for 0.125 μs shaping time.
- Canberra 8715 AD converter.
- Canberra Accuspec B multi-channel analyzer.

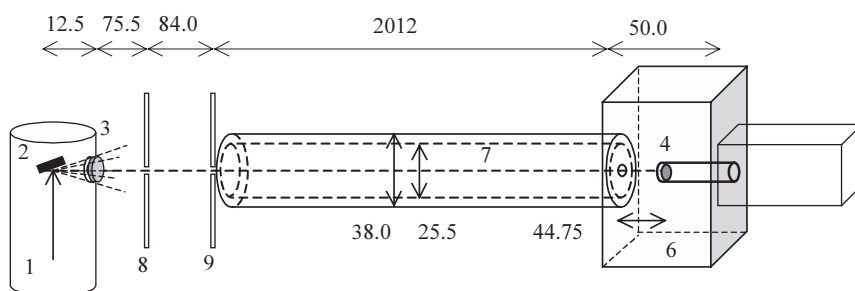


Figure 9.7 The experimental set-up that was used in the TSFX measurements, comprising the side-window X-ray tube (1), the tungsten target (2), the secondary fluorescence foils, placed directly behind the Be exit window (3), the detector (4), that is placed in a lead box (6), a stainless steel tube (7) that shields the path between X-ray tube and detector and 2 lead collimators (8) and (9) that are placed between the X-ray tube and the stainless steel tube in order to prevent direct irradiation of the latter and reduce contributions from scattering. Dimensions are given in units [mm].

The experimental set-up is shown in Figure 9.7. The secondary fluorescence foils (3) with a diameter of 20.0 mm are placed directly behind the Be exit window (3) of the X-ray tube with a diameter of 22.0 mm, at a distance of 12.5 mm from the tungsten target. The detector (4) is placed in a lead box (6) with a lead collimator with 1.0 mm aperture diameter in front of it, that determines the effective area of the detector, resulting in a solid angle of $0.157 \times 10^{-6} \text{ sr}$ between X-ray target and detector (target to detector distance is 2235 mm).

The set-up included a stainless steel tube (7), with inner and outer diameters 30.0 and 38.0 mm, respectively, that shields the path between X-ray tube and detector. A polypropylene tube with inner and outer diameters 21.5 and 25.5 mm, respectively, was placed inside in order to absorb the fluorescence radiation from the stainless steel tube. Two 3 mm thick lead collimators (8) and (9) with aperture diameters 2.0 and 20.0 mm, respectively, are placed between the X-ray tube and the stainless steel tube in order to prevent direct irradiation of the latter and reduce contributions from scattering. The apertures of these

collimators can be precisely centred around the geometrical axis of the set-up as they are adjustable in both horizontal and vertical direction.

9.6.2 Simulation of the experimental set-up

An approximation of the experimental set-up was made by using a simplified simulation model that only includes the X-ray target and the secondary fluorescence foils. The simulated geometry is illustrated in Figure 9.8.

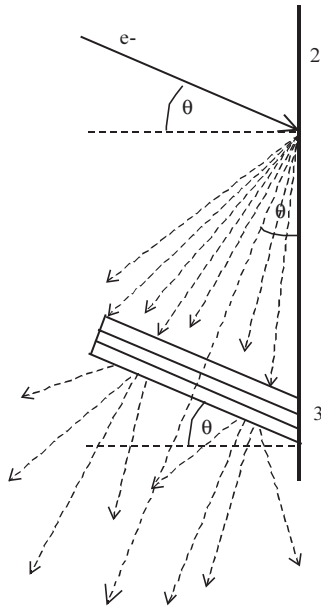


Figure 9.8 Simplified simulation model of the TSFX set-up, including the X-ray target (2) and the secondary fluorescence foils (3).

Incident electrons hit a 1.5 mm thick tungsten target (2) with a target angle $\theta = 20^\circ$ and a focal spot size of $0.6 \times 0.6 \text{ mm}^2$. The generated X-rays that are emitted in a cone with half top angle $\theta = 20^\circ$ irradiate the secondary fluorescence foils (3) at a central distance of 12.5 mm from the focal spot.

The beryllium exit window from the X-ray tube is not included in the simulation model, for reasons mentioned in section 9.2. The fluorescence radiation emitted by the foils and the transmitted primary X-ray continuum that emerges from the anode with angles $< 10^\circ$ with respect to the central axis of emission (indicated by the bold arrow) is recorded.

We verified that the angular distribution of the spectrum within this 10° angle is constant within 5% (cf. section 9.2.5). Corrections to the simulated spectra are applied for the foil area that is 'seen' by the detector and the real solid angle between foil position and effective detector area in the measurements.

9.6.3 Data processing

With the X-ray tube operated at 0.3 mA/100 kV, the spectra have been recorded by the multi-channel analyzer in 2048 channels of 0.0625 keV (i.e. the energy range 0 – 128 keV). The data were corrected for pile-up, dead time and accumulated in 1 keV energy bins to allow direct comparison with simulations (that record output spectra in energy bins of 0.1 keV).

The simulated number of incident electrons is scaled to the tube current, integrated over the ‘elapsed live time’ (approximately 100 seconds) in the measurements and therefore the comparison is made for the number of counts recorded during measurements. Simulated data are convoluted with a Gaussian shaped energy resolution function with 1.5 keV FWHM. The energy resolution was assessed by Reimerink (1999), who performed measurements on the same experimental set-up from Figure 9.7, but with the X-ray tube replaced by an ^{241}Am source.

The simulation model does not account for scattering and fluorescence other than from the target and secondary fluorescence foils, i.e. radiation emerging from copper in the X-ray tube head, silver in the detector, the stainless steel and polypropylene tubes in the set-up, lead collimators and shielding is not considered in the comparison with simulations. The same applies to escape peaks from the detector materials Cd, Zn and Te and to charge collection tails from energy peaks, all of which occur in measured spectra.

Given all these approximations, a rough comparison between measurements and simulations is what is being aimed at. Experimental verification of the TSFX simulations should therefore mainly be judged by the order of magnitude of the spectral intensities, rather than by detailed spectrum shapes. Quantitative agreement within a factor 2 is considered acceptable.

9.6.4 Results

Results are presented in Figure 9.9, for simulated and measured spectra, for the unattenuated primary X-ray spectrum and for set-ups that include different secondary fluorescence foils, the thicknesses of which are indicated in the graphs.

Most important, simulated and measured intensities are in the same order of magnitude, mostly within a factor 2. Detailed spectrum shapes are however quite different. Although the various fluorescence peaks occur in both the measured and simulated spectra, the latter generally show higher intensities. This is partly due to imperfect charge collection in measurements, that, especially for higher energies, causes part of the peak intensities to be ‘smeared’ to lower energies. The uncertainty in the measured intensities is mainly determined by the error in the position of the foils relative to the X-ray target and the detector. Reimerink (1999) concluded that an estimated error of 2 mm in these distances results in a variation of 16% in measured fluorescence intensities.

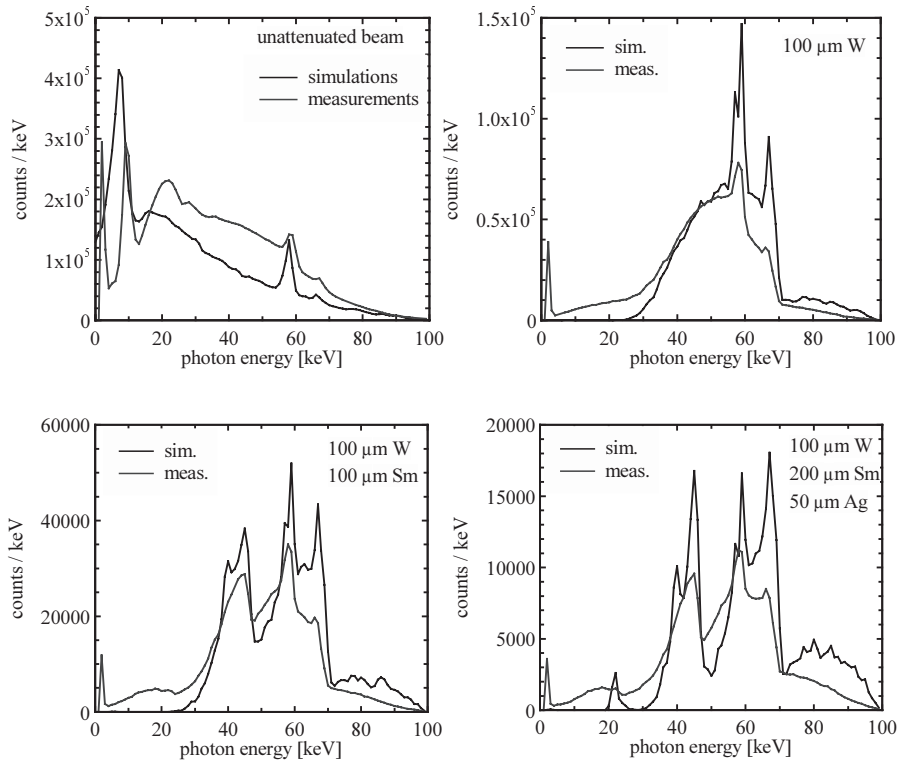


Figure 9.9 Results from TSFX measurements together with simulated spectra, for the unattenuated primary X-ray spectrum and for set-ups that include different secondary fluorescence foils, the thicknesses of which are indicated in the graphs.

10 Reflection Secondary Fluorescence X-ray Spectra

In Chapter 9, we concluded that MEXA analysis by means of the optimized TSFX spectrum does not enable determination of X-ray line intensities with the required accuracy of about $\sim 1 \times 10^{-4}$. The background continuum contribution in the spectrum causes small deviations in detected intensities, resulting in large errors in the component fractions. This was the reason to study a second, so-called Reflection Secondary Fluorescence X-ray (hereafter: RSFX) set-up, in order to obtain spectra with higher peak/continuum ratios. The principle of RSFX is explained in the following section.

10.1 Simulation of a RSFX set-up

The main disadvantage of the geometry in the TSFX set-up is simultaneous detection of the primary X-rays in forward direction; although most of the bremsstrahlung is effectively converted into secondary fluorescence, a considerable fraction is *not* absorbed and is detected as the critical background continuum in the spectra.

Therefore, the RSFX set-up aims at taking away this background continuum by separating the directions of emission for the secondary fluorescence radiation and the primary X-rays. A schematic picture of the RSFX set-up is presented in Figure 10.1.

The secondary fluorescence radiation that is emitted by the foils is detected under a 90 degrees angle with respect to the central axis of the primary X-rays (the +z-axis). In this geometry, the primary X-rays are not emitted in the direction of the detector, which results in higher peak/continuum ratios in the spectra.

Contrary to the TSFX set-up, the foils are not attached parallel to the end-window of the tube, but (in set-up (A)) under an angle $\vartheta = 45^\circ$ in order to reduce absorption of the emitted fluorescence in the foils themselves. In comparison with the TSFX set-up, this also implies a larger average distance between the anode and the foils, and correspondingly lower fluorescence intensities. The dimensions in the simulations of the anode and the foils in x- and y-directions are HORZDIST and VERTDIST, respectively, the values of which are equal.

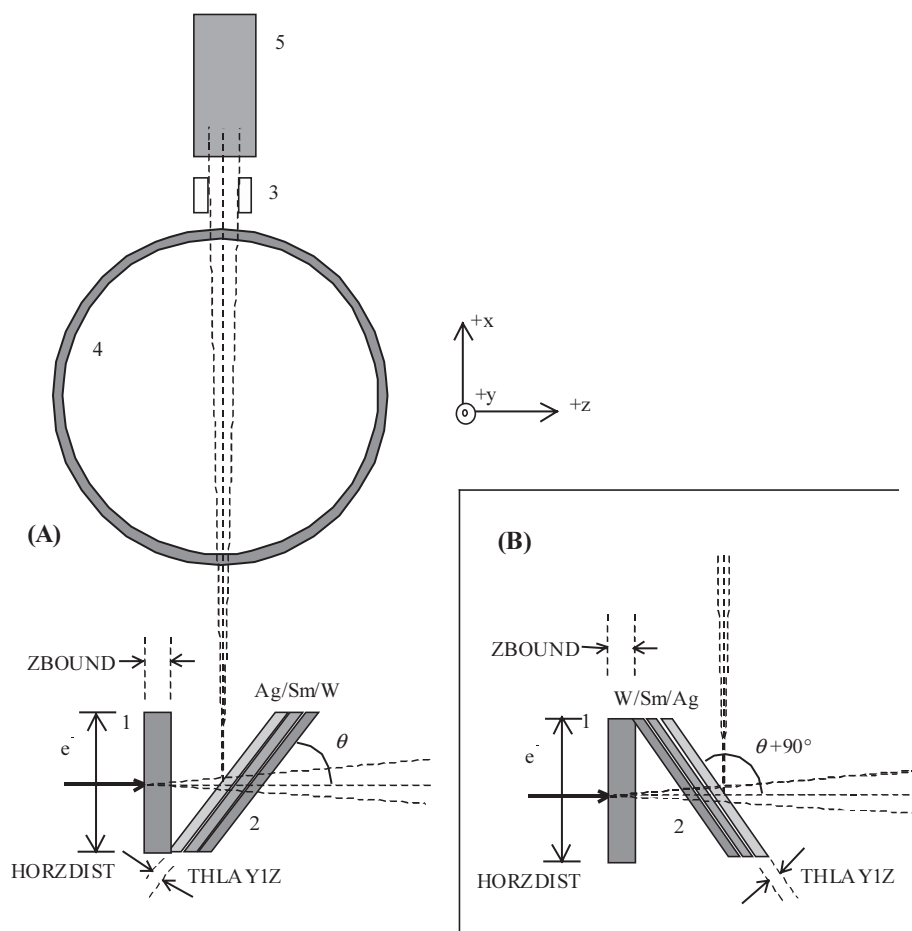


Figure 10.1 Schematic top view of a RSFX set-up. Components: anode (1), secondary foil materials (2), collimators (3), oil pipe and multiphase flow (4) and detector system (5). In graph (A) on the left, the foil order in $+z$ -direction is Ag, Sm, W. The inset shows an alternative set-up (B) with foil order W, Sm, Ag. Secondary foil thicknesses for Ag, Sm and W are given by THLAY1Z, THLAY2Z and THLAY3Z, respectively (only THLAY1Z is indicated in the graphs). HORZDIST indicates the dimension of the anode in the x -direction and $\theta = 45^\circ$ denotes the angle between the foil surface and the $+z$ -direction.

With HORZDIST = VERTDIST = 2 cm and $\theta = 45^\circ$ in Figure 10.1, the distance between the anode and the centre of the foils is 1 cm, a realistic value for an MPFM device (see section 10.5.4). However, lower values for HORZDIST and VERTDIST (3 mm) and the distance between the anode and the centre of the foils (1.5 mm) were initially used in simulations, in order to ‘speed up’ the photon scoring.

The different components anode (1), secondary foil materials (2), collimators (3), oil pipe and multiphase flow (4) and detector system (5) are indicated in the drawings. Secondary foil thicknesses in the simulations for Ag, Sm and W are given by THLAY1Z, THLAY2Z and THLAY3Z, respectively (only THLAY1Z is indicated in the drawings).

The only components that have been implemented in the EGS4 simulations are the anode and the foil materials, while the other components (oil pipe, low radiation absorption windows and detector) were included in the simulations performed by Bom (see section 8.6.3). We refer to section 9.2 for the used input values for EGS4 as these are similar for both the TSFX and RSFX set-up.

The method for obtaining normalized spectral intensities is similar to that of the TSFX simulations; from all photons that emerge from the foil area that is ‘seen’ by the detector, only those emitted with an angle $< 10^\circ$ with respect to the $+x$ -direction are recorded. A correction is then performed for the real solid angle between foil position and detector.

10.1.1 The anode

Initial studies with the RSFX set-up were aimed at obtaining spectra suitable for MEXA analysis with integrated determination of salinity, i.e. spectra with three peaks at energies 60, 40 and 20 keV. However, contrary to the TSFX set-up, the 60 keV peak in the RSFX spectrum does not originate from primary fluorescence in the anode as this radiation is not detected. Instead, a tungsten foil with thickness THLAY3Z is added to the ‘foil sandwich’, thus providing the fluorescence peak at $E = 60$ keV.

Contrary to the TSFX set-up, the anode thickness and material are no longer prescribed by the required amount of photo-ionization that yields sufficient primary fluorescence radiation, and the energy of the latter, respectively.

The initially used anode material tungsten was therefore substituted by gold (hereafter: Au); not only does this result in a somewhat higher bremsstrahlung yield ($\sim 5\%$, derived from simulations) due to higher atomic number ($Z = 79$ and 74 for Au and W, respectively), but also the attachment of a $10 \mu\text{m}$ Au layer to a Be substrate is easier than for a W layer with the same thickness, as was argued by Howard (1999). The value ZBOUND = $10 \mu\text{m}$ follows from the analytical expression described in section 9.2.2, with $\rho = 19.3 \text{ g cm}^{-3}$ as the mass density of Au (equal to that of tungsten).

10.1.2 Foil order

The foil set-ups in graphs (A) and (B) of Figure 10.1 illustrate two different methods of generating secondary fluorescence radiation; in graph (A), the foils are positioned in order of increasing atomic number in the $+z$ -direction, i.e. Ag, Sm, W, while in graph (B), the order is reversed to W, Sm, Ag.

The lower atomic number foils are closest to the detector in both set-ups, which ensures that fluorescence radiation with lower energies, emitted in the direction of the oil pipe and detector, does not suffer absorption in an intermediate material with higher atomic number. Furthermore, set-up (A) has the additional advantage that a thick W foil can be used for shielding of the primary X-rays.

10.2 Results from simulations

10.2.1 Comparison between the RSFX set-ups

In this section, we discuss results from initial simulations to determine which of the two RSFX set-ups (A) and (B) yields the most favourable spectra for MPFM. Figure 10.2 shows the simulated spectra from the RSFX set-ups (A) or (B), using a W anode with ZBOUND = 10 μm and Ag, Sm and W foils with thicknesses THLAY1Z = 50 μm , THLAY2Z = 200 μm and THLAY3Z = 100 μm . The centre of the first foil is positioned at a distance of 1.5 mm from the anode.

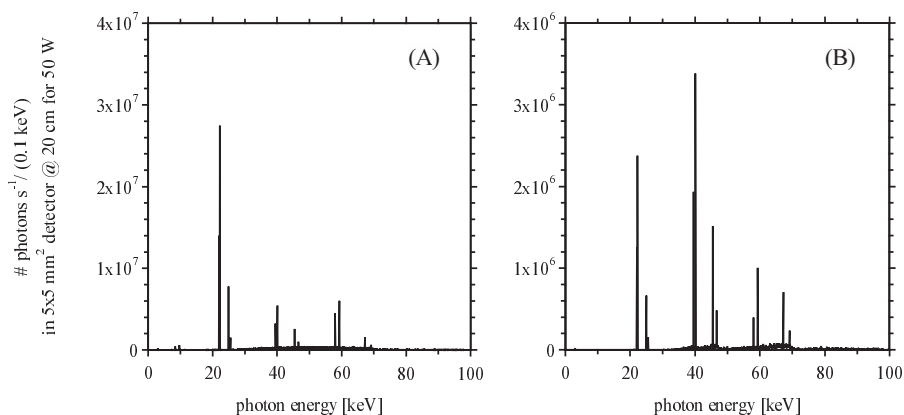


Figure 10.2 Simulated spectra from the RSFX set-ups (A) and (B), using a W anode with ZBOUND = 10 μm and Ag, Sm and W foils with thicknesses THLAY1Z = 50 μm , THLAY2Z = 200 μm and THLAY3Z = 100 μm . The centre of the first foil is positioned at a distance of 1.5 mm from the anode. Note that the vertical scale in graph (A) is higher by a factor 10.

The average intensity of the background continuum, that originates from scattering in the foils, has decreased considerably in comparison with the optimized TSFX spectrum (see Figure 9.6), with fluorescence peak/continuum ratios now varying between 100 and 1000.

The fluorescence intensities from set-up (B) are in the same order of magnitude as those from the optimized TSFX spectrum, however, in set-up (A) these are considerably higher (about one order of magnitude for Ag fluorescence). The explanation for this is the better match between the order of foils in set-up (A) and the shape of the primary X-ray spectrum; the lower energy photons with $E \geq 26$ keV (Ag K-binding energy) are effectively absorbed in the Ag foil and at the same time the transmission of photons with $E \geq 47$ keV (Sm K-binding energy) is acceptable, which results in sufficient generation of fluorescence in the Sm foil. Finally, the intensity of photons with $E \geq 70$ keV (W K-binding energy) that are not absorbed in the Ag and Sm foils is high enough for generation of fluorescence in the W foil.

The intensity of Ag fluorescence in set-up (A) is considerably higher (\sim a factor 5) than that of Sm or W, which is considered favourable because of the stronger attenuation in the oil pipe and multiphase flow. However, the optimum ratio of the separate fluorescence peaks is a different issue that is addressed in section 10.5.

These results indicate that further optimization should concern set-up (A). For this set-up, the influence of a different foil rotation angle ϑ has been studied which will now be discussed.

10.2.2 Influence of foil rotation

The RSFX spectra of Figure 10.2 correspond to an angle $\vartheta = 45^\circ$ between the surfaces of the anode and the foils, which means that the average pathlengths for absorption of primary X-rays and emission of secondary fluorescence photons are equal. A lower value for the foil rotation angle ϑ is anticipated to yield higher fluorescence intensities, since absorption in the $+z$ -direction increases and attenuation of fluorescence photons in the $+x$ -direction decreases.

Therefore, simulations were performed similar to those for set-up (A) of section 10.2.1, i.e. with Ag, Sm and W foils with thicknesses $THLAY1Z = 50 \mu\text{m}$, $THLAY2Z = 200 \mu\text{m}$ and $THLAY3Z = 100 \mu\text{m}$, but with foil rotation angles $\vartheta = 15^\circ, 30^\circ, 60^\circ$ and 75° . The results for the integrated K fluorescence intensity vs. ϑ show that a lower value for ϑ is indeed more favourable: compared with $\vartheta = 45^\circ$, the intensities (total for Ag, Sm and W) change by +20%, +10%, -10% and -30% for $\vartheta = 15^\circ, 30^\circ, 60^\circ$ and 75° , respectively.

A lower value for ϑ is especially beneficial for Ag fluorescence, since this is the first foil to be irradiated by the primary X-rays. The influence is less pronounced for Sm and W, because increased absorption in the Ag foil also implies that less transmitted photons are available for photo-ionization in the other two foils. Since the beneficial effect of a lower value for ϑ on the already sufficient fluorescence intensities is only within 20% and, more important, the peak/continuum ratios remain equal within 10%, it was decided to maintain the value $\vartheta = 45^\circ$ because of the symmetric geometry (see section 10.5.3).

10.2.3 The optimized RSFX spectrum

Further improvements on the RSFX set-up, in particular on the peak/continuum ratio, has eventually resulted in optimum foil thicknesses $THLAY1Z = 20 \mu\text{m}$ and $THLAY2Z = 20 \mu\text{m}$ for Ag and Sm. The optimized RSFX spectrum is shown in the above graph from Figure 10.3. The use of thinner Ag and Sm foils results in reduction of the continuum background from scattered photons, yielding peak/continuum ratios in the order of 1000, illustrated by the inset in the figure. The simulation was performed with Au as anode material, with a thickness of $ZBOUND = 10 \mu\text{m}$. With a thickness of $THLAY3Z = 5 \text{ mm}$, the fluorescence intensity from the W foil is 'saturated'; when $THLAY3Z$ is higher than $\sim 500 \mu\text{m}$, the enhanced absorption in the W foil compensates a significant increase of the emitted fluorescence. The value therefore illustrates the potential use of the W foil for shielding of primary X-rays.

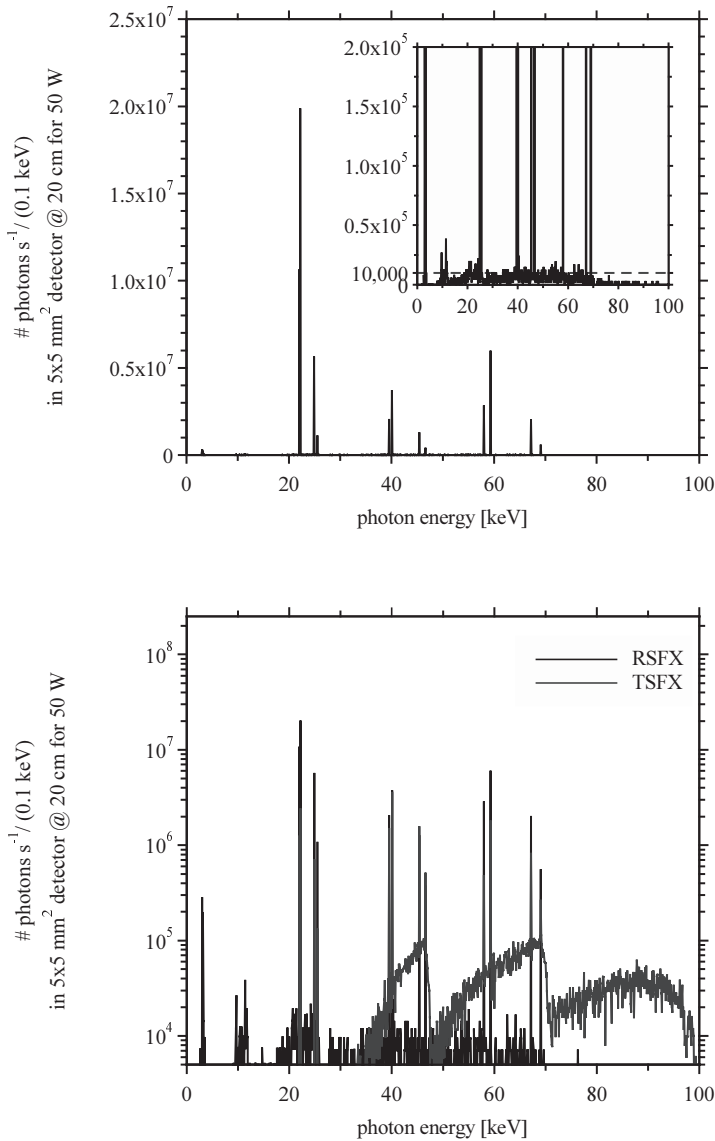


Figure 10.3 Above: the optimized RSFX spectrum from simulations, based on foil thicknesses $THLAY1Z = 20 \text{ } \mu\text{m}$, $THLAY2Z = 20 \text{ } \mu\text{m}$ and $THLAY3Z = 5 \text{ mm}$ for Ag, Sm and W respectively, Au anode with thickness $ZBOUND = 10 \text{ } \mu\text{m}$. The peak/continuum ratios are in the order of 1000, illustrated by the inset Below: comparison between the same optimized RSFX spectrum and the optimized TSFX spectrum from Figure 9.6.

The same optimized RSFX spectrum is depicted in the below graph from Figure 10.3, together with the optimized TSFX spectrum from Figure 9.6. The advantage of the RSFX principle for the generation of secondary fluorescence radiation is clearly illustrated by the higher peak/continuum ratios. Also, as opposed to the TSFX spectrum, the continuum

background is more or less constant which facilitates extraction of net peak intensities from the detected spectra.

10.3 Comparison with measurements

Reimerink (1999) performed measurements at Shell in order to verify the RSFX simulations. The equipment that was used has been described in section 9.6.1 for the TSFX measurements, while the geometry of the experimental set-up is similar to that of the simulations, see Figure 10.1, set-up (A): the foils are positioned under an angle $\theta = 45^\circ$ with respect to the primary X-rays and the emitted secondary fluorescence is detected under a 90 degrees angle. However, the various dimensions in the experimental set-up differ from those in the simulations.

The distance between the anode of the side-window X-ray tube and the first foil is 3.2 cm (1.5 mm in the simulations), the foils-detector distance is 50 cm (20 cm in the simulations) and a lead collimator with an aperture diameter of 1.0 cm was placed in between the foils and the detector, at 20 cm from the foils. The comparison between measurements and simulations is performed for foils with thicknesses 50 μm Ag / 200 μm Sm / 100 μm W.

The experimental data are compared with results from simulations after correction for the different dimensions. Other corrections to the simulations and the data processing are similar to those for the TSFX set-up and have been described in sections 9.6.2 and 9.6.3.

10.3.1 Results

Results from RSFX measurements and simulations are presented in Figure 10.4. It is clear that the agreement for the peak intensities is reasonable for Ag and Sm fluorescence peaks (within 25%), but moderate for W K_{α} fluorescence peaks, with a measured peak intensity higher by a factor ~ 2 , as illustrated by the inset in the figure.

The higher background intensities in measurements are partly due to scattering in the set-up other than from the target and secondary fluorescence foils. Besides this, imperfect charge collection in the detector causes part of the measured peak intensities to be 'smeared' to lower energies, thus enhancing the background intensity, especially for the higher energies. The visible structure in the measured intensity below 20 keV originates from various escape peaks in the CdZnTe detector, e.g. Sm $K_{\alpha 1}$ - Te $K_{\beta 1}$ at 9.1 keV, Sm $K_{\alpha 1}$ - Te $K_{\alpha 1}$ at 12.6 keV and Sm $K_{\beta 1}$ - Te $K_{\alpha 1}$ at 17.9 keV.

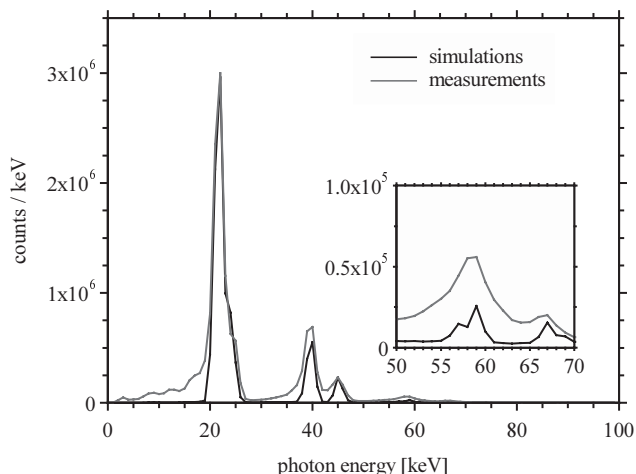


Figure 10.4 Results from RSFX measurements and simulations for secondary fluorescence foils with thicknesses 50 , m Ag / 200 , m Sm / 100 , m W.

10.4 MPFM with RSFX spectra

Bom (2000) concluded from the MEXA analysis (with integrated determination of water salinity) that the optimized RSFX spectrum of Figure 10.3 still does not enable determination of X-ray line intensities with a required accuracy of about $\sim 1 \times 10^{-4}$.

If a fluorescence peak with energy < 20 keV could be included in the spectrum, this would reduce the sensitivity of the analysis for exact X-ray line intensities (see section 8.6.3) and the background intensity in the RSFX spectra might become acceptable. Therefore, simulations were also performed with the Ag foil replaced by other foils with lower K fluorescence energies, e.g. molybdenum with $K_{\alpha} = 17.5$ keV and zirconium with $K_{\alpha} = 15.8$ keV. Both secondary fluorescence intensities and peak/continuum ratios with these foils are in the same order of magnitude as with the Ag/Sm/W foil combination.

It was however confirmed by Frieling (1999) that in an MPFM device the radiation pathlength t in the multiphase flow cannot be assigned a value below 40 mm, which implies a minimum photon energy of 20 keV (see section 8.5.2). Thus, the conclusion that RSFX spectra (although more suitable than TSFX spectra) cannot be used for MEXA analysis with integrated determination of water salinity, still holds.

From now on, further optimization in this chapter on the design of the MPFM device therefore applies to MEXA analysis *without* integrated determination of water salinity.

10.5 The prototype RSFX set-up for MPFM

In section 8.6.4, it was concluded that disturbance of the line intensities with 1% of the peak contents results in an oil fraction error of 1-2%, depending on the specific multiphase flow composition. With peak/continuum ratios from the optimized RSFX spectrum in the order of 1000, the required accuracy is anticipated to be reached.

The RSFX principle is therefore considered to be suitable for MEXA analysis; now that salinity is no longer considered a variable to be solved, the optimum spectrum to be used in a prototype RSFX set-up consists of two fluorescence peaks at energies 21 and 49 keV, with an intensity ratio 1 to 10 (see section 8.6.4). Since the dependence of MEXA analysis results on these exact energies is small, Sm and Ag foils were maintained for the generation of fluorescence. Before addressing how the optimum RSFX spectrum can be generated, two items in the equipment of the prototype RSFX set-up are discussed: the X-ray tube and the detector.

10.5.1 The Trufocus MAX-10 X-ray tube

In section 9.1.3, we discussed the rationale of an end-window X-ray tube. Frieling (1999) issued required specifications (see section 8.4) to various vendors; based on the optimization with RSFX simulations, the ideal end-window X-ray tube should include a high atomic number material (W or Au) anode with a thickness of $\sim 10 \mu\text{m}$, preferably integrated with the exit window of the tube. After comparison of the different types of end-window X-ray tubes that were available, Trufocus Corporation, Watsonville, CA, USA seemed the most suitable candidate to provide us with the desired X-ray tube.

Since the so-called Trufocus MAX-10 X-ray tube is still under development, the following specifications are subject to changes. Electrons are incident on an $8 \mu\text{m}$ thick Au layer (with a focal spot size of $1.5 \times 1.5 \text{ mm}^2$) on a $\sim 750 \mu\text{m}$ thick Be substrate. The primary X-rays are transmitted through a $250 \mu\text{m}$ thick Be exit window at a distance of 0.19 cm from the Au layer. The target holder assembly, shown in Figure 10.5, is enclosed in a copper ring holder with a diameter of 2.1 cm, that itself forms a concentric protrusion of 0.4 cm from the aluminum front plane of the housing of the tube. This cylindrical housing with a diameter of 11.4 cm is also made from aluminum and consists of a mounting flange on the front plane that enables a rigid external connection with the secondary fluorescence foils at a short distance. This is discussed in section 10.5.4.

The air-cooled X-ray tube with integrated power supply is operated at a high voltage $\leq 100 \text{ kV}$ (stability 0.05%) and a tube current of 1.0 mA up to 50 kV / 0.5 mA up to 100 kV (stability 0.1%), i.e. a maximum power of 50 W. Information about the energy and angular distribution of X-rays from the Trufocus MAX-10 X-ray tube is yet to be made available by Trufocus Corporation.

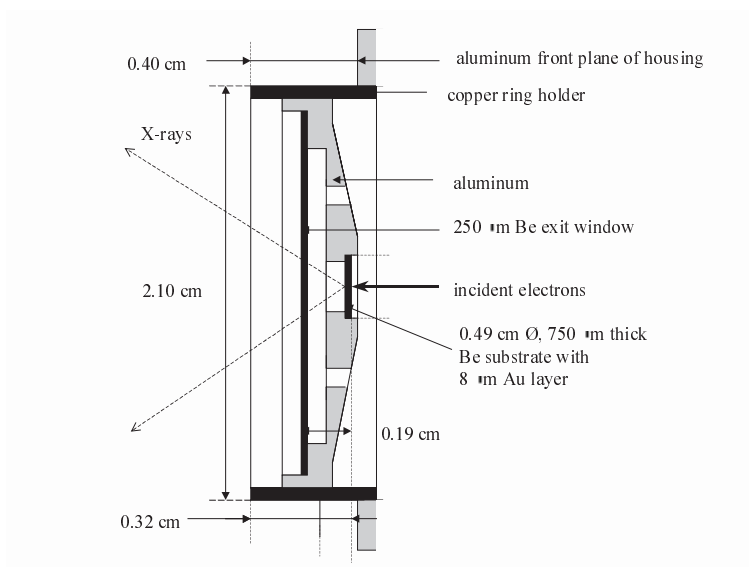


Figure 10.5 Target holder assembly in the Trufocus MAX-10 X-ray tube.

10.5.2 The Amptek XR-100CR Si detector

An elaborate discussion about different types of X-ray detectors is e.g. given by Knoll (1967). Here, we will restrict ourselves to the rationale of the detector choice, with CdZnTe and Si detectors as two main candidates for the detection of X-rays.

The CdZnTe detector is characterized by an efficiency of $\sim 100\%$ for photon energies up to 100 keV. There are nevertheless several disadvantages to the use of a CdZnTe detector for RSFX spectra: each combination of a fluorescence line from the foil materials Ag and Sm on the one hand and the different detector elements Cd, Zn and Te on the other hand occurs as an escape peak in the detected spectra, at an energy shifted downwards with respect to that of the foil materials, by an amount equal to the difference between the two lines (see section 10.3.1). Many of these escape peaks will interfere with the Ag and Sm fluorescence lines which seriously hinders MEXA analysis.

Interpretation of the spectra is furthermore complicated by the charge collection tails of the detected peaks, that hamper accurate determination of the net intensities.

The main rationale of the use of a Si detector is the suitability for low energies and the relative simplicity of the spectrum; escape peaks do not show up in the detected spectra due to the very low Si K-fluorescence yield $\omega_K = 0.047$ (data from Lederer et al. (1978)). Furthermore, there are no charge collection tails of the fluorescence peaks. Compared to CdZnTe, the energy resolution is generally better in smaller Si detectors and the contribution of Compton scattering in the detector is less, due to the lower mass density of Si ($\rho = 2.33 \text{ g cm}^{-3}$) and the lower anticipated detector thickness.

The low efficiency for higher energies is a disadvantage of a Si detector: whereas the efficiency of a 2 mm thick CdZnTe detector is $\sim 100\%$ for energies up to 100 keV, this value is $\sim 20\%$ at 20 keV and $\sim 2\%$ at 50 keV, for a 200 μm thick Si detector. A thicker Si detector would therefore be advantageous, as long as correspondingly longer shaping times do not conflict with the required high total count rate of $10^5 \text{ counts s}^{-1}$.

Miller (2000) issued the required specifications for a Si X-ray detector to various vendors. Based on their reactions, it was concluded that the Amptek XR-100CR Si-PIN detector is most suitable: while the thickness of 500 μm (fully depleted) ensures higher efficiency for the Ag and Sm fluorescence peaks ($\sim 40\%$ and $\sim 4\%$ for 20 and 50 keV, respectively), full spectrum count rates $\geq 10^5 \text{ counts s}^{-1}$ can be achieved, with an energy resolution $\leq 2 \text{ keV FWHM}$ at 20 keV (in combination with a Canberra 2026-series shaping amplifier, at 0.5 μs shaping time). This energy resolution enables distinction of the Ag K_α and K_β lines in the spectrum analysis.

Calculations by Bom and Clarijs (2000) show that with simulated RSFX intensities, a 500 μm thick Si detector is suitable for MEXA analysis. Furthermore, the active area of the Amptek XR-100CR Si-PIN detector is $5 \times 5 \text{ mm}^2$ and the thickness of the Be entrance window is 100 to 250 μm . The detector can be mounted on a single or dual stage Peltier thermoelectric cooler in order to accomplish a maximum temperature difference of 80 $^\circ\text{C}$; with a closed-loop temperature control, the detector can then be operated at room temperature while the ambient operating temperature varies between -20°C and $+90^\circ\text{C}$. More detailed information about the Amptek XR-100CR Si detector can be found at <http://www.amptek.com>.

10.5.3 Inclusion of the second detector

During operation of the MPFM device, the shape and intensity of the secondary fluorescence spectrum are subject to (minor) changes in high voltage and current stability of the X-ray tube, temperature drift, mechanical vibrations, etc. Since the MEXA analysis is sensitive to small deviations in measured peak intensities, a second detector must be used to monitor the fluorescence spectrum emitted by the foils, thus enabling corrections in the MEXA analysis.

This reference spectrum is not transmitted through the oil pipe and multiphase flow and since it is preferable to have equal fluorescence intensities emitted in the directions of both detectors, the latter should be symmetrically positioned with respect to the secondary foils. The anticipated geometry with the secondary foils and the detectors is shown in Figure 10.6.

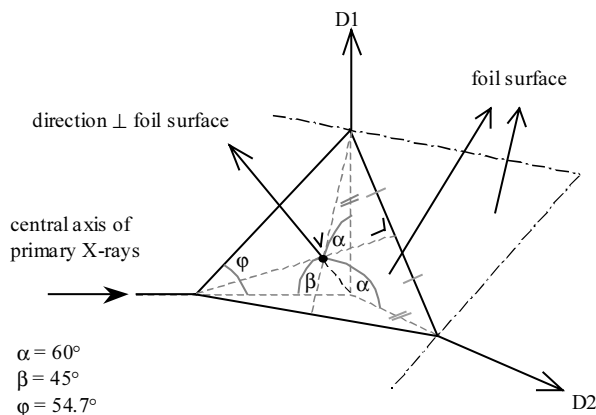


Figure 10.6 The geometry of the secondary foils and the detectors in the prototype RSFX set-up. The central axis of the primary X-rays is indicated by the bold arrow on the left. The useful secondary fluorescence radiation is emitted towards two detectors (indicated by D1 and D2), positioned in mutually perpendicular directions, with an average angle of $90 - \alpha = 30^\circ$ with respect to the foil surface.

The triangular plane in the figure represents the surface of the fluorescence foil, truncated by the three perpendicular planes in the Cartesian coordinates system. The primary X-rays, indicated by their central axis (bold arrow on the left), are incident with an angle of $\beta = 45^\circ$ with respect to the direction perpendicular to the foil surface. With the incoming X-rays and the two detectors (indicated by D1 and D2) in mutually perpendicular directions, the useful secondary fluorescence radiation is now emitted towards these detectors with an average angle of $90 - \alpha (=60^\circ) = 30^\circ$ with respect to the foil surface. This implies that, compared to the initial RSFX simulations on a geometry that comprised only one detector under an angle of 45° with respect to the foil surface, the average attenuation of the emitted fluorescence in the foils has increased, which is taken into account in the simulations of section 10.6.

10.5.4 The foil holder assembly

Whereas initial RSFX simulations have been performed for a distance of 1.5 mm between the Au target and the centre of the foils, this value will be larger in the prototype RSFX set-up; not only is there a 0.32 cm separation between the position of the 8 μm thick Au target and the front plane of the copper ring holder (see Figure 10.5), but any contact between the foils and the Be exit window of the X-ray tube must be avoided as this is one of the most fragile parts of the system.

Also taking into account the oblique orientation of the fluorescence foils, the distance between the Au target and the centre of the foils will be in the order of ~ 1 cm, the value that is used in the simulations of section 10.6.

We designed a device that keeps the secondary foils in fixed position at a well-defined distance from the Au target. The so-called foil holder assembly is currently being manufactured at Daniel Europe ltd. A schematic is presented in Figure 10.7.

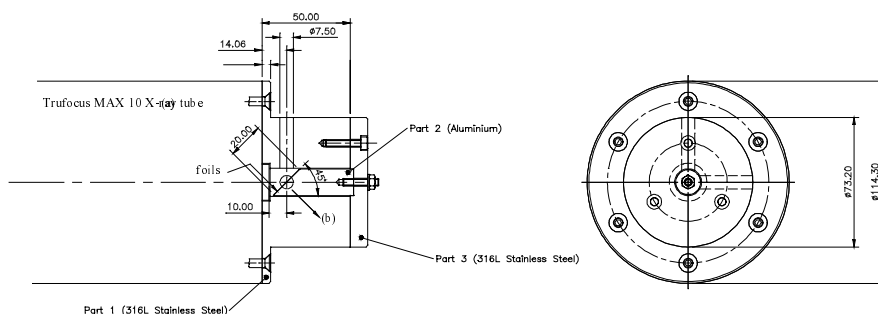


Figure 10.7 Schematic of the foil holder assembly that keeps the secondary foils in fixed position at a distance of ~ 1 cm from the Au target.

The foil holder assembly comprises three parts: the cylindrical body of the assembly (Part 1) is made of 316 L stainless steel and is connected to the aluminum mounting flange on the front plane of the Trufocus MAX-10 X-ray tube housing. A cylindrical aluminum foil support rod (Part 2) is inserted at the back-side of Part 1 in a concentric cylindrical canal and kept in fixed position by means of a 316 L stainless steel flange (Part 3) that is mounted on Part 1. The secondary fluorescence foils are attached to the oblique end of the support rod and matched to the full size of this surface. Adhesives, which are not susceptible to radiation damage, are to be investigated.

The slice angle of the foil support rod is 45° ; the foils are brought in the desired orientation by rotating the rod over 45° around its central axis. The secondary fluorescence radiation is emitted towards both detectors via two narrow, mutually perpendicular collimator canals (a) and (b). The surface of the rod immediately behind the foils may be machined out to reduce background scattering in the fluorescence spectrum. As for the stainless steel body of the assembly, the higher level of radiation shielding provided by this material is considered to outweigh the lower spectral background expected from an aluminum construction. Again, any background radiation reaching the detector will be minimized by machining out material from the vicinity of the primary X-ray beam as required.

10.6 Simulation of the prototype RSFX set-up

The simulation model of the prototype RSFX set-up is based on previous RSFX simulations, that have been discussed in section 10.1. Electrons are incident on the Au target with a focal spot size of $1.5 \times 1.5 \text{ mm}^2$ and a thickness of $ZBOUND = 8 \text{ }\mu\text{m}$. The Be substrate and exit window with a total thickness of $\sim 1 \text{ mm}$ were not included in the simulations. Furthermore, the centre of the first foil is positioned at 1 cm from the Au target, the anticipated distance in the prototype RSFX set-up.

The oblique orientation of the fluorescence foils is taken into account in the simulations by only considering the effective area of the foils that is 'seen' by the detectors, i.e. the central part of the foils with a projected area of 25 mm^2 . From all photons that emerge from this

effective area, the simulations record only those emitted with an angle $< 10^\circ$ with respect to the direction of one the detectors. As mentioned in section 10.5.3, these mutually perpendicular directions are defined by an angle of 30° with respect to the foil surface, as shown in Figure 10.6.

Simulations on different foil combinations confirmed that equal fluorescence intensities (within a statistical uncertainty of 2%) are emitted in the directions of both detectors. Normalized spectral intensities are obtained after correction for the real solid angle between foil position and detector.

10.6.1 The fluorescence foil order

The optimum fluorescence spectrum for the prototype RSFX set-up is characterized by an intensity ratio of 1 to 10 for the Ag and Sm fluorescence intensities, as discussed in section 8.6.4. The simulations in section 10.2 on RSFX set-ups with a Ag foil in front of a Sm foil (Ag/Sm foil order) have illustrated that the 1 to 10 ratio is difficult to achieve; the Ag foil yields a higher fluorescence intensity than the Sm foil, due to the direct irradiation of the primary X-rays and the lower absorption of the fluorescence radiation in the foil.

A combination of a very thin Ag foil in front of a thick Sm foil provides an estimate of the maximum Sm/Ag fluorescence intensity ratio. From simulations on a $10\text{ }\mu\text{m}$ Ag / 5 mm Sm foil combination, we calculated a ratio of 1.6 for the integrated K fluorescence intensities; this confirms that the Ag/Sm foil order does not yield suitable spectra for the prototype RSFX set-up.

It was decided to invert the order of the foils to Sm/Ag, in order to enhance Sm fluorescence intensity at the expense of lower Ag fluorescence intensity. From simulations on different Sm/Ag foil combinations we derived the optimum combination as $90\text{ }\mu\text{m}$ Sm / $100\text{ }\mu\text{m}$ Ag; the corresponding Sm/Ag fluorescence intensity ratio is 9.5, close to the required value 10. These foil thicknesses are therefore used in the optimized spectrum for the prototype RSFX set-up, discussed in section 10.6.2.

10.6.2 The optimized spectrum for the prototype RSFX set-up

The optimized spectrum for the prototype RSFX set-up is shown in Figure 10.8 and corresponds to the following specifications:

- 100 keV electrons incident on a Au anode with a focal spot size of $1.5 \times 1.5\text{ mm}^2$ and a thickness of $8\text{ }\mu\text{m}$.
- $90\text{ }\mu\text{m}$ Sm / $100\text{ }\mu\text{m}$ Ag foils positioned at 1 cm from the Au target under an angle of 45° with respect to the central axis of the primary X-rays.
- Normalized intensity: the number of photons per second that is emitted under an average angle of 30° with respect to the foil surface and hits a $5 \times 5\text{ mm}^2$ detector surface at a distance of 20 cm from the centre of the foils, with the X-ray tube operated at 0.5 mA / 100 kV (50 W).

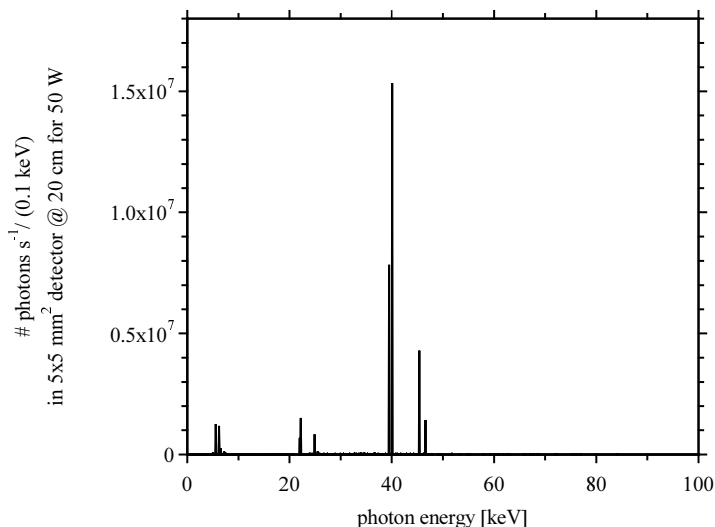


Figure 10.8 The optimized spectrum for the prototype RSFX set-up: Au anode with a focal spot size of $1.5 \times 1.5 \text{ mm}^2$ and thickness ZBOUND = 8 μm , 90 μm Sm / 100 μm Ag foils positioned at 1 cm from the Au target under an angle of 45° with respect to the central axis of the primary X-rays.

The integrated K fluorescence intensities are $2.87 \times 10^7 \text{ photons s}^{-1}$ and $3.02 \times 10^6 \text{ photons s}^{-1}$ for Sm and Ag respectively, i.e. an intensity ratio of 9.5. The peak/continuum ratio for Sm fluorescence is in the order of ~ 1000 , however for Ag this value is ~ 100 due to the lower fluorescence intensity. The background in the spectrum up to 100 keV takes up $\sim 15\%$ of the total intensity, i.e. the same order of magnitude as the 20% assumed in the MEXA analysis from section 8.6.3. The low peaks at $\sim 6 \text{ keV}$ originate from Sm L fluorescence and are not anticipated to show up in the detected spectrum due to absorption in the MPFM set-up.

The optimum Ag/Sm fluorescence intensity ratio 1 to 10 corresponds to required intensities of $1.2 \times 10^5 \text{ photons s}^{-1}$ and $1.2 \times 10^6 \text{ photons s}^{-1}$, respectively, in the MEXA analysis by Bom and Clarijs (2000). These values are lower than the fluorescence intensities in the optimized spectrum for the prototype RSFX set-up by a factor ~ 25 .

It follows that, with an X-ray tube power in the order of $\sim 2.5 \text{ W}$, successful MEXA analysis should be possible. The ultimate performance of the prototype MPFM device will be assessed by an extensive test program for the measurement of multiphase flow compositions at Daniel Europe Ltd.

11 Conclusions

In this thesis, three studies on new applications of radiation in medicine and industry have been summarized. Studies I and II illustrate that beta and low energy photon radiation are valuable tools in respectively cardiovascular and intraoperative brachytherapy. In Study III the diagnostic qualities of photon radiation are used in industry for non-invasive flow metering.

The main goal in each of the studies was to design radiation-based systems that meet the prescribed requirements for the specific applications. In other words, optimizing the use of radiation is what was being aimed at throughout this thesis. The use of Monte Carlo simulations played an important role in the design processes as they provide a quick, flexible means of inspecting the influence of different design parameters. However, experimental verification is indispensable to the validity of simulations and therefore comparisons with measured data were made prior to conclusions. In this final chapter a summary will be given of the results obtained, followed by recommendations for further research.

11.1 Study I: Modelling of a $^{188}\text{W}/^{188}\text{Re}$ beta line source for coronary brachytherapy by means of EGS4 Monte Carlo simulations

Three different source models were used to simulate the dose distribution around a $^{188}\text{W}/^{188}\text{Re}$ coronary brachytherapy source by means of EGS4 Monte Carlo simulations. Besides an elaborate source model that contains the microstructure of the radioactive tungsten coil (SR model), we used two models with a modified source geometry. In both the DENCOR and the DIACOR models the radial center of radioactivity is the same as in the real source, but whereas the DENCOR model uses a source mass density correction to compensate the modified geometry, the DIACOR model makes use of a source diameter scaling. The three models showed an acceptable consistency within 10%, in terms of the radial dose distribution in water, allowing us to use one of them as a flexible tool for optimization of source design parameters. Consistency with measurements was verified by experiments using a PMMA phantom. This consistency is within 15% up to $r = 4$ mm.

Characterization of the source for vascular application is achieved by specifying the radial dose distribution in water, together with the length along which the dose deposition does not decrease by more than a certain percentage. This representation is considered more

suitable for long beta line sources than the dose calculation formalism recommended by the AAPM Task Group 60. Simulations predict $D(r_0, z=0) = 0.313 \pm 0.012$ Gy/min for a 204 ± 8 (2 σ) MBq $^{188}\text{W}/^{188}\text{Re}$ source in water.

From the dose rate distribution over the full radial range up to the maximum possible target depth in the vessel wall, a source activity of 2.0 GBq for a 40 mm long source is derived in order to achieve a required dose rate of 1 Gy/min at 3 mm radial distance. Dose is predominantly deposited by beta radiation since $^{188}\text{W}/^{188}\text{Re}$ gamma and X-ray dose deposition contributes less than 5% within the therapeutically relevant region $1 < r < 5$ mm.

Dosimetric effects due to the microgeometry of the source do not extend into the therapeutically relevant region, which means that the dose homogeneity in the target is not disturbed. The dose distribution shows a rapid decrease at the source ends, in between which there is a region along the source in which the dose deposition remains constant within 10% up to $r = 5$ mm. From this, we derive an effective length $L_{eff} = 2.95$ cm for a line source with a length of 40 mm.

In the context of radiation safety, air kerma rates members of the medical staff are exposed to during treatment have been determined. These have been assessed by simulation, analytical calculation and experiment. For a therapeutic source with activity $A(^{188}\text{W}/^{188}\text{Re}) = 2.0$ GBq and without any shielding precautions, we derive an air kerma rate of ~ 20 $\mu\text{Gy/h}$ at 1 m. This numerical value can be regarded an upper limit for the total effective dose to a member of the medical staff, assuming a distance of 0.5 m from the source and a treatment time of 15 minutes. The assessed air kerma rate can be used in detailed calculations to determine the effective dose. These calculations require information about the specific positions of the source, patient and medical staff member. They should also include the use of weighting coefficients for different types of radiation and organs or tissues.

The simulated air kerma rate is in moderate agreement with experimental data (the latter being higher by 34%) which may be due to overresponse of the TLD at low photon energies. It should be investigated whether this effect is also responsible for the observed discrepancy between simulated and measured radial depth-dose distributions beyond $r = 4$ mm (difference $> 15\%$).

Both 1) the absolute dose rate distribution over the full radial range up to the maximum possible target depth in the vessel wall and 2) the homogeneity of the dose distribution in the vessel wall in the direction along the lesion have been quantified, which was the primary aim of Study I. This dosimetry study has contributed to the design and development of a prototype $^{188}\text{W}/^{188}\text{Re}$ beta line source for coronary brachytherapy. Notwithstanding the fact that satisfactory results have been obtained during the prototype development, indicating feasibility of the $^{188}\text{W}/^{188}\text{Re}$ beta line source for coronary brachytherapy, Nucletron B.V. has decided not to proceed with commercial production, for reasons beyond the scope of this thesis.

11.2 Study II: Feasibility of an intraoperative brachytherapy source

Using a calculational model for the source, applicator and target in a homogeneous water medium, we analyzed the feasibility of using a low-energy photon source for intraoperative brachytherapy (IOBT).

Assuming an isotropic point source emitting monoenergetic photons, the accumulated dose distribution in the target has been determined for different photon energies E , including the dose deposition due to Compton scattered photons. The accumulated dose distribution in the target depends on the photon energy, the dimensions of the source applicator and the source activity. Assuming equal dwell times for all source positions in an applicator with an area about equal to that of the target prescription plane (200 cm^2), we derive an optimum photon energy $E \sim 25 \text{ keV}$. Assuming furthermore a radiation yield of 1 photon per disintegration, a source activity $A(E = 25 \text{ keV}) \sim 1.5 \times 10^{12} \text{ Bq}$ is required in order to achieve within a maximum treatment time of 20 minutes an average dose deposition of 10 Gy in the target prescription plane at a depth of $r = 1 \text{ cm}$.

As opposed to the above, we conclude that photon energies $E < 30 \text{ keV}$ energies are increasingly less suitable because of significant absorption of photons in the source capsule that is anticipated to contain the IOBT source. For $E < 30 \text{ keV}$, the source capsule absorption, quantified as the relative decrease in dose deposition at $r = 1 \text{ cm}$, strongly exceeds 50%, whereas for $50 < E < 100 \text{ keV}$, this value ranges from $\sim 20\%$ to $\sim 10\%$. The lower limit for the suitable photon energy of an IOBT source is therefore estimated at $E \sim 30 \text{ keV}$.

In order to ensure radiation safety during IOBT, we calculated the amount of radiation shielding material that restricts the air kerma rate for a member of the medical staff to an acceptable value of 1 to $10 \text{ } \mu\text{Gy}$ per treatment of 20 minutes; assuming that $\sim 1.5 \text{ mm}$ of lead is the maximum amount of shielding that can be applied during treatment, the upper limit for the suitable photon energy E of an IOBT source is assigned a value of $\sim 100 \text{ keV}$. Although photons with higher energies contribute (significantly) to therapeutic dose delivery in the target, this does not compensate for the shielding difficulties they entail during IOBT. In this context, the maximum allowed intensity for photons with energies $100 \text{ keV} < E < 2 \text{ MeV}$ has been determined.

Taking into account the absorption of photons in the source capsule, required point source activities (assuming a radiation yield of 1 photon per disintegration) for $30 \text{ keV} < E < 100 \text{ keV}$ range from $A(E = 30 \text{ keV}) = 3.4 \times 10^{12} \text{ Bq}$ to $A(E = 100 \text{ keV}) = 1.9 \times 10^{12} \text{ Bq}$, in order to achieve within a maximum treatment time of 20 minutes an average dose deposition of 10 Gy in the target prescription plane at a depth of $r = 1 \text{ cm}$. The required homogeneity in the target, that should be within a factor 2, is achieved for $30 \text{ keV} < E < 100 \text{ keV}$.

Self-absorption of photons and the use of a carrier in the source material lead to reduced dose deposition in the target and correspondingly higher required source activities. These effects have been quantified for ^{125}I . From this analysis we conclude that ^{125}I does not meet the therapeutic requirements for an IOBT source.

The results from Study II have been translated into an outline for the feasibility analysis that comprises both therapeutic and radiation safety requirements. It can be used in further research in order to quantify the suitability of a potential IOBT source.

11.3 Study III: Design of an X-ray setup for a multiphase flow metering device

In a multiphase flow metering (MPFM) device that determines the composition of oil/water/gas mixtures based upon the principle of multiple energy X-ray absorption (MEXA), monoenergetic X-rays in the energy range $20 \text{ keV} < E < 60 \text{ keV}$ should be used, instead of filtered (narrow) energy bands or the entire X-ray spectrum.

In this energy range, only photoelectric absorption and Compton scattering play a role in the attenuation of X-rays. Since the energy dependence of these photon-matter interaction effects is to first order independent of the atomic number of the constituents oil, water, salt and gas in the multiphase flow, inclusion of a third energy in the analysis does not allow for more than three of the four fractions to be derived. The salinity could only be calculated if measured intensities are determined with an extremely high accuracy of $\sim 1 \times 10^{-4}$. It is not believed that unattended stand-alone field systems can attain the required accuracy.

It was therefore decided to abstain from optimizing the design of the MPFM device for integrated determination of water salinity. The latter should be assessed by an independent measurement.

The optimum X-ray energies for MEXA were assigned the values 21 and 49 keV, with an optimum intensity ratio 1 to 10. These optimum energies ensure that the system is least sensitive to line intensity deviations as they are defined as those energies for which the oil fraction error is minimal, over the range of all relevant energy sets, oil-, water-, and gas fractions and salinity. The continuum background in the X-ray spectra should be as low as possible.

Two different types of X-ray set-ups have been studied by means of EGS4 simulations in order to try to generate the optimum X-ray spectra for MEXA analysis. Results from simulations have been verified by analytical calculations and experiments. In both set-ups, thin samarium and silver foils are positioned at a short distance from an end-window X-ray tube operated at 100 kV. The primary X-ray spectrum is effectively converted into secondary fluorescence generated in these foils, yielding high intensity spectra of mono-energetic peaks on a low intensity background continuum that are used for the MEXA analysis.

Whereas in the transmission-type set-up the primary X-rays and the secondary fluorescence radiation are both detected in forward direction, in the reflection-type set-up the spectrum is detected under a 90 degrees angle. This separation between the directions of

emission for the secondary fluorescence radiation and the primary X-rays effectively reduces the contribution from the latter, yielding higher peak/continuum ratios in the order of 100 to 1000. Therefore, also taking into account that spectral intensities are sufficiently high, so-called Reflection Secondary Fluorescence X-ray spectra are considered most suitable for MEXA analysis. We conclude from simulations that, with optimum foil thicknesses $90\text{ }\mu\text{m Sm} / 100\text{ }\mu\text{m Ag}$ and a required X-ray tube power in the order of only $\sim 2.5\text{ W}$, successful MEXA analysis should be possible.

We designed a prototype RSFX set-up for MPFM, that comprises the following:

- (1) An end-window X-ray tube in which 100 keV electrons are incident on a Au transmission anode with a focal spot size of $1.5 \times 1.5\text{ mm}^2$ and a thickness of $8\text{ }\mu\text{m}$.
- (2) A stainless steel/aluminum foil holder assembly that keeps the secondary fluorescence foils in fixed position at a distance of $\sim 1\text{ cm}$ from the Au target.
- (3) $90\text{ }\mu\text{m Sm} / 100\text{ }\mu\text{m Ag}$ foils, attached to the oblique end of the support insert rod from the above foil holder assembly under an angle of 45° with respect to the central axis of the primary X-rays.
- (4) Two Si detectors of $500\text{ }\mu\text{m}$ thickness, fully depleted, enabling full spectrum count rates $\geq 10^5\text{ counts s}^{-1}$ with a required energy resolution $\leq 2\text{ keV FWHM}$. One detector records the spectrum transmitted through the oil pipe, while the other one is used to monitor the fluorescence spectrum emitted by the foils. The anticipated position for both detectors is at 20 cm from the secondary fluorescence foils.

At present, we are awaiting delivery of the complete equipment, after which the prototype unit will be assembled and prepared for initial experimental tests. The ultimate performance of the prototype MPFM device will then be assessed by an extensive test program for the measurement of multiphase flow compositions at Daniel Europe Ltd., Larbert, Stirlingshire, Scotland.

References

Amersham 1999 *Complete Guide to Radiochemicals* Amersham Pharmacia Biotech Benelux, Roosendaal, The Netherlands

Amols H I and Weinberger J 1996 Intravascular Brachytherapy Physics: Review of Radiation Sources & Techniques, in *Vascular Brachytherapy*, edited by R. Waksman, S. B. King, I. R. Crocker and R. F. Mould, Nucletron B.V., Veenendaal, The Netherlands

Attix F H 1986 *Introduction to Radiological Physics and Radiation Dosimetry* John Wiley & Sons, New York

Bertin E P 1978 *Introduction to X-ray Spectrometric Analysis*, Plenum Press, New York

Bertrand O F et al. 1997 Intravascular radiation therapy in atherosclerotic disease: promises and premises *Eur. Heart. J.* **18** 1385-1395

Bielajew A F, Mohan R, Chui C 1989 *Improved bremsstrahlung photon angular sampling in the EGS4 code system*, report nr. PIRS-0203, Institute for National Measurements Standards, NRCC, Ottawa, Canada

Bilski P, Olko P, Burgkhardt B and Piesch E 1995 Ultra-thin LiF:Mg, Cu, P detectors for beta dosimetry *Radiat. Meas.* **24** 439-443

Blaauw M 1993a A Versatile Computer Algorithm for Linear First-order Equations Describing Compartmental Models with Backward Branching *Appl. Radiat. Isot.* **44**, 1225-1229

Blaauw M 1993b *The Holistic Analysis of Gamma-ray Spectra in Instrumental Neutron Activation Analysis*, PhD thesis, Interfaculty Reactor Institute (IRI), Delft University of Technology, Delft, The Netherlands

- Bom V R 1997 Radiation Technology Group, Interfaculty Reactor Institute (IRI), Delft University of Technology, Delft, The Netherlands, private communication
- Bom V R, Clarijs M C, Kolar Z I and van Eijk C W E 1998 *Progress report on the development of MEXA, a Multiple Energy X-ray Analysis system for multiphase flow measurements – Period January 1-June 30, 1998*, report nr. IRI-ISO-980035, Radiation Technology Group, Interfaculty Reactor Institute (IRI), Delft University of Technology, Delft, The Netherlands
- Bom V R 1999 *Multiphase flow metering – Triple Energy X-ray Absorption, a means to determine salinity?*, Radiation Technology Group, Interfaculty Reactor Institute (IRI), Delft University of Technology, Delft, The Netherlands, private communication
- Bom V R 2000 Radiation Technology Group, Interfaculty Reactor Institute (IRI), Delft University of Technology, Delft, The Netherlands, private communication
- Bom V R, Clarijs M C, van Eijk C W E, Kolar Z I, Frieling J, Scheers A M and Miller G 2000 Accuracy Aspects in Multiphase Flow Metering using X-ray Transmission, presented at IEEE 2000, Lyon, France, to be published in IEEE Trans. Nucl. Sci.
- Bom V R and Clarijs M C 2000 *Optimal X-ray energies for DEGRA multiphase flow metering – Report by order of SHELL-SIEP, Rijswijk, The Netherlands*, Stratech Report ST-ISO-2000-004, Radiation Technology Group, Interfaculty Reactor Institute (IRI), Delft University of Technology, Delft, The Netherlands
- Bos A J J 1994 *Inleiding in de dosimetrie van ioniserende straling*, IRI-131-94-016, Interfaculty Reactor Institute (IRI), Delft University of Technology, Delft, The Netherlands
- Bos A J J, Draaisma F S, Okx W J C and Rasmussen C E 2000 *Inleiding tot de stralingshygiëne* Elsevier Gezondheidszorg, Maarssen, The Netherlands ISBN 90 352 22601
- Brun R and Carminati F 1994 *GEANT Detector Description and Simulation Tool*, CERN Program Library Long Witeup W5013, Geneve, Switzerland
- Chaouki J (editor) 1997 *Non-invasive Monitoring of Multiphase Flows*, Elsevier Science B.V., Amsterdam, The Netherlands
- Chilton A B, Shultis J K and Faw R E 1984, *Principles of Radiation Shielding*, Prentice-Hall Int. Inc, London
- Clarijs M C 1996 *Monte Carlo Computer Simulations on a Cardiovascular Brachytherapy Source (I)*, Stratech Report nr. TUD-MEDR-96-03, Radiation Technology Group, Interfaculty Reactor Institute (IRI), Delft University of Technology, Delft, The Netherlands

- Clarijs M C 1997 *Monte Carlo Computer Simulations on a Cardiovascular Brachytherapy Source (II)*, Report nr. IRI-ISO-970088, Radiation Technology Group, Interfaculty Reactor Institute (IRI), Delft University of Technology, Delft, The Netherlands
- Clarijs M C, Bos A J J, van Eijk C W E and Schaart D R 2000 Modelling of a $^{188}\text{W}/^{188}\text{Re}$ beta line source for coronary brachytherapy by means of EGS4 Monte Carlo simulations Phys. Med. Biol. **45** 1319-1334
- Dawson J T 1991 Theoretical considerations regarding low-dose radiation therapy for prevention of restenosis after angioplasty Texas Heart Journal **18** 4-7
- Diamond D A and Vesely T M 1998a The Role of Radiation Therapy in the Management of Vascular Restenosis. Part I: Biological Basis J. Vascular & Interventional Radiol. **9** (2) 199-208
- Diamond D A and Vesely T M 1998b The Role of Radiation Therapy in the Management of Vascular Restenosis. Part II: Radiation Techniques and Results J. Vascular & Interventional Radiol. **9** (2) 389-400
- Dillman L T and von der Lage F C 1975 Radionuclide decay schemes and nuclear parameters for use in radiation-dose estimation, MIRD Pamphlet **10** Society of Nuclear Medicine, New York
- Dries W J F 1997 Catharina Hospital, Eindhoven, The Netherlands, private communication
- Dries W J F (editor) et al. 1999 *Klinische Fysica, Nr. 1999/2*, issued by Nederlandse Vereniging voor Klinische Fysica (NVKF), Utrecht, The Netherlands
- Duane S, Bielajew A F and Rogers D W O 1989a NRCC Report PIRS-0173, *Use of ICRU-37/NBS Collision Stopping Powers in the EGS4 System* NRCC, Ottawa, Canada
- Duane S, Bielajew A F, Rogers D W O and Nelson W R 1989b NRCC Report PIRS-0177, *Use of ICRU-37/NBS Radiative Stopping Powers in the EGS4 System* NRCC, Ottawa, Canada
- Erdtmann G 1976 *Neutron Activation Tables*, Kernchemie in Einzeldarstellungen Volume 6, Verlag Chemie, Weinheim, New York
- Erdtmann G and Soyka W 1979 *The Gamma Rays of the Radionuclides* Verlag Chemie, Weinheim, New York
- Evans R D 1955 *The atomic nucleus* McGraw-Hill, reprinted (1982), Krieger R E, Malabar, Florida, USA
- Frieling J 1999 Shell International Exploration and Production, Rijswijk, The Netherlands, private communication

- Hammer E A, Johansen G A and Thorn R 1998 Measurement Principles in Multiphase Metering – Their Benefits and Limitations, in *The Future of Multiphase Metering, 4th International Conference – Multiphase Technology Series (March 1998)*, conference documentation.
- Harrison L B 1995 HDR Intraoperative Brachytherapy, in *8th International Brachytherapy Conference, Nice 1995* Nucletron B.V., Veenendaal, The Netherlands
- Hooft E van 't, Löffler E, Schaart D R, Gerrits F and Bauer B 1996 Brachytherapy for Prevention of Restenosis: Afterloading Requirements for Endovascular Use, in *Vascular Brachytherapy*, edited by R. Waksman, S. B. King, I. R. Crocker and R. F. Mould, Nucletron B.V., Veenendaal, The Netherlands
- Hoppenbrouwers M B 1996 *Design of a multiphase composition meter for oil-water-gas mixtures based on dual energy X-ray transmission*, STUDREP report nr. 95.081, Shell International Exploration and Production, Rijswijk, The Netherlands
- Howard G 1999 Trufocus Corporation, Watsonville, CA, USA, private communication
- Hubbell J H 1982 Photon Mass attenuation and Energy-absorption Coefficients from 1 keV to 20 MeV, *Int. Jour. Appl. Radiat. Isot.* **33**, pp 1269-1290.
- ICRP Publication 51 1987 Data for Use in Protection Against External Radiation, *Annals of the ICRP* 17 (2/3)
- ICRP Publication 60 1990 Recommendations of the International Commission on Radiological Protection, Publication 60, ISBN 0-08-041144-4 Pergamon Press, New York
- ICRU Report 37 1984 *Stopping Powers for Electrons and Positrons* The International Commission on Radiation Units and Measurements (ICRU), ICRU Publications, Bethesda, Washington DC, USA
- Jenkins TM, Nelson W R and Rindi R 1987 *Monte Carlo Transport of Electrons and Photons*, Plenum Press, New York
- Khan F M 1992 *Physics of Radiation Therapy*, 2nd edition, Williams & Wilkins, Baltimore, Maryland, USA
- King S B 1996 Restenosis Following Angioplasty, in *Vascular Brachytherapy*, edited by R. Waksman, S. B. King, I. R. Crocker and R. F. Mould, Nucletron B.V., Veenendaal, The Netherlands
- Knoll G F 1967 *Radiation Detection and Measurement*, 2nd edition, John Wiley & Sons, New York

- Kocher D C 1981 *Radioactive Decay Data Tables, DOE/TIC-11026* U.S. Department of Commerce National, National Technical Information Service, Washington DC, USA
- Lederer et al. 1978 *Table of Isotopes (7th edition)*, John Wiley & Sons, New York
- Leliveld C J 1996 *A fast Monte Carlo simulator for scattering in X-ray Computerized Tomography*, PhD thesis, Department of Applied Physics, Delft University of Technology, Delft, The Netherlands
- Levy R I 1979 *Prevalence and epidemiology of cardiovascular disease*, in *Textbook of Medicine*, edited by Beeson P B, McDermott W and Wyngaarden J B, Saunders, Philadelphia, USA 1059 – 1063
- Löffler E 1997 Nucletron BV, Veenendaal, The Netherlands, private communication
- McCollough C H and Schueler B A 2000 Educational Treatise – Calculation of effective dose Med. Phys. **27** (5) 828-837
- Miller G 1999a *MEXRA Prototype – Low energy X-ray transmission at a 5 cm pathlength*, Daniel Europe Ltd., Larbert, Stirlingshire, Scotland, private communication
- Miller G 1999b *Salinity determination by the X-ray absorption method*, Daniel Europe Ltd., Larbert, Stirlingshire, Scotland, private communication
- Miller G 1999c *Static testing on 2-phase mixtures – salinity evaluation*, Daniel Europe Ltd., Larbert, Stirlingshire, Scotland, private communication
- Miller G 2000, Daniel Europe Ltd., Larbert, Stirlingshire, Scotland, private communication
- Mintz G S, Popma J J, Pichard A D, Kent K M, Satler L F, Painter J A and Leon M B 1994 Mechanisms of later arterial responses to transcatheter therapy: A serial quantitative angiographic and intravascular ultrasound study. (abstr) Circulation **90** I 24
- Namito Y, Hirayama H and Ban S 1997 Improvements of Low-energy Photon Transport in EGS4, KEK Preprint 97-237, Radiation Science Center, High Energy Accelerator Research Organization (KEK), Tsukuba, Japan
- Namito Y and Hirayama H 1999 Implementation of the electron-impact ionization into the EGS4 code Nucl. Instr. and Meth. in Phys. Res. A **423** 238-246
- Namito Y 2000 Radiation Science Center, High Energy Accelerator Research Organization (KEK), Tsukuba, Japan, private communication

- Nath R and Lui L 1997 On the depth of penetration of photons and electrons for intravascular brachytherapy Med. Phys. **24** 1358 (abstract)
- Nath R, Amols H, Coffey C, Duggan D, Jani S, Li Z, Schell M, Soares C, Whiting J, Cole P E, Crocker I and Schwartz R 1999 Intravascular brachytherapy physics: Report of the AAPM Radiation Therapy Committee Task Group No. 60 Med. Phys. **26** (2) 119-152
- Nelson W R and Jenkins T M 1980 *Computer Techniques in Radiation Transport and Dosimetry*, Plenum Press, New York
- Nelson W R, Hirayama H and Rogers D W 1985 *The EGS4 Code System* SLAC Report 265, Stanford Linear Accelerator Center, Stanford, CA, USA
- Nori D 1994 Intraoperative Brachytherapy: Rationale & Future Directions, in *Brachytherapy from radium to optimization*, edited by R F Mould, Battermann J J, Martinez A A and Speiser B L, Nucletron B.V., Veenendaal, The Netherlands
- Nucletron BV, Veenendaal, The Netherlands 1996 Freiburger flab Silopren LSR source applicator, technical drawing 089378 (company confidential).
- Nucletron BV, Veenendaal, The Netherlands 1997 Intra-Operative Brachytherapy Source document (company confidential).
- Pocock S J, Henderson R A, Rickards A F et al. 1995 Meta analysis of randomized trials comparing angioplasty with bypass surgery Lancet **346** 1184-1189
- Reimerink T 1999, Shell International Exploration and Production, Rijswijk, The Netherlands, private communication
- Santen H van, Kolar Z I and Scheers A M 1995 Photon Energy Selection for Dual Energy γ - and/or X-ray Absorption Composition Measurements in Oil-Water-Gas Mixtures Nucl. Geophys. **9** 193-202
- Schaart D R 1995a *Progress Report 1, Vascular Brachytherapy Source*, Stratech Report TUD-MEDR-05-01, Radiation Technology Group, Delft University of Technology, Delft, The Netherlands
- Schaart D R 1995b *Progress Report 2, Vascular Brachytherapy Source*, Stratech Report TUD-MEDR-05-01, Radiation Technology Group, Delft University of Technology, Delft, The Netherlands
- Schaart D R, Bos A J J, Winkelman A J M, Clarijs M C and van Eijk C W E 2000a Radial depth dose distribution of a beta particle line source measured with ultra-thin TLD's in a PMMA phantom, to be published in Radiat. Protec. Dosim.

Schaart D R, Clarijs M C and Bos A J J 2000b Comments on the applicability of the AAPM Task Group 60 dose calculation formalism to endovascular line sources, to be published in Med. Phys.

Scheers A M 1994 *Composition measurement based on DEGRA, Part 1 – Principle and selection of components*, report nr. RKGR.94.044, Shell International Exploration and Production, Rijswijk, The Netherlands

Scheers A M 1995 *Multi-phase flow metering with ILS/DEGRA – A trial in Shell's Gabon Rabi field*, report nr. RKGR.95.128, Shell International Exploration and Production, Rijswijk, The Netherlands

Scheers A M and Slijkerman W F J 1996 *Multi-phase flow measurement using multiple energy gamma ray absorption (MEGRA) composition measurement*, SPE Annual Technical Conference Proceedings 6-9 Oct 1996, Denver, USA

Seelmann-Eggebert W et al. 1981 *Karlsruher Nuclidkarte*, 5. Auflage, Kernforschungszentrum Karlsruhe GmbH, Karlsruhe, Germany

Slater D N 1962 *Gamma-rays of radionuclides in order of increasing energy*, Butterworths, London, UK

Slijkerman W F J 1994 *Multiphase composition measurement for varying water salinities; Triple Energy Gamma Ray Absorption (TEGRA)*, report nr. RKGR.94.173, Shell International Exploration and Production, Rijswijk, The Netherlands

Slijkerman W F J 1995 *Field Demonstration of calibration-free composition measurement using gamma-ray absorption*, report nr. RKGR.95.155, Shell International Exploration and Production, Rijswijk, The Netherlands

Smith A R (editor) 1995 *Radiation Therapy Physics*, Springer-Verlag, Berlin Heidelberg, Germany

Soares C G, Halpern D G and Wang C K 1998 Calibration and characterization of beta-particle sources for intravascular brachytherapy Med. Phys **25** 339–346

Sowby F D et al. 1983 *Radionuclide Transformations, Energy and Intensity of Emissions*, ICRP Publication 38, Volumes 11-13, Pergamon Press, New York

Storm E and Israel H I 1970 Photon cross sections from 1 keV to 100 MeV for elements from $Z = 1$ to $Z = 100$ Nuclear Data Tables, Vol A7, Academic Press, New York

Vries W de and Grimbergen T W M 1995 NMI-VSL Report S-TS-3401/10042548, the Dutch Radiation Standard Laboratory (Nederlands Meetinstituut, NMI), The Netherlands

- Vries W de 1997 *Second activity measurement $^{188}\text{W}/^{188}\text{Re}$ source*, Report nr. S-TS-97.05, the Dutch Radiation Standard Laboratory (Nederlands Meetinstituut, NMI), The Netherlands
- Waksman R 1996 Radiation for prevention of restenosis: where are we? *Int. J. Radiat. Oncol., Biol., Phys.* **36** 959 – 961
- Weast R C, Astle M J et al. 1980 *CRC Handbook of Chemistry and Physics*, 60th edition, CRC Press, Florida, USA
- Weber J and Rasmussen C E 1985 *Stralingsbescherming*, Delftse Uitgeversmaatschappij B.V., Delft, The Netherlands
- Weinberger J, Ennis R D and Amols H 1996 Intracoronary Irradiation for the Prevention of Restenosis: Analysis in the Swine Model, in *Vascular Brachytherapy*, edited by R. Waksman, S. B. King, I. R. Crocker and R. F. Mould, Nucletron B.V., Veenendaal, The Netherlands
- Williamson J F 1995 Recent Development in Basic Brachytherapy Physics, in *Radiation Therapy Physics* edited by Smith A R, Springer-Verlag, Berlin Heidelberg
- Wilson B J et al. 1966 *The Radiochemical Manual*, second edition, the Radiochemical Centre, Amersham
- Winkelmann A J M and Bos A J J 1997 *β -depth-dose distribution in a PMMA phantom from a ^{188}W linesource* IRI report 131-97-008 Interfaculty Reactor Institute (IRI), Delft University of Technology, Delft, The Netherlands

Abbreviations

AAPM	American Association of Physicists in Medicine
BTS	Bedrijfsgerichte Technologische Samenwerkingsprojecten
DEGRA	Dual Energy Gamma Ray Absorption
DENCOR	Density Correction
DIACOR	Diameter Correction
EGS4	Electron Gamma Shower 4
EII	Electron Impact Ionization
GVF	Gas Volume Fraction
HDR	High Dose Rate
HFIR	High Flux Isotope Reactor
ICRP	International Commission on Radiological Protection
ICRU	International Commission on Radiation Units and Measurements
IOBT	Intraoperative Brachytherapy
IORT	Intraoperative Radiation Therapy
MC	Monte Carlo
MCP	Mg, Cu, P
MEXA	Multiple Energy X-ray Absorption
MPFM	Multiphase Flow Metering
NMI	Nederlands Meetinstituut (Dutch Radiation Standard Laboratory)
PMMA	Polymethylmethacrylate
PTB	Physikalisch-Technische Bundesanstalt
PTCA	Percutaneous Transluminal Coronary Angioplasty
RSFX	Reflection Secondary Fluorescence X-ray
SR	Square Rings
TLD	Thermoluminescent Detector
TSFX	Transmission Secondary Fluorescence X-ray
WC	Water-cut

Design studies on Cardiovascular & Intraoperative Brachytherapy and Multiphase Flow Metering

New applications of radiation in medicine and industry

Summary

In this thesis, three studies on new applications of radiation in medicine and industry are summarized. Studies I and II illustrate that beta and low energy photon radiation are valuable tools in cardiovascular and intraoperative brachytherapy, respectively. In Study III the diagnostic qualities of photon radiation are used in industry for non-invasive flow metering.

Study I: Modelling of a $^{188}\text{W}/^{188}\text{Re}$ beta line source for coronary brachytherapy by means of EGS4 Monte Carlo simulations

One of the relatively new therapeutic applications of radiation lies in the field of restenosis prevention. Restenosis can be defined as the re-narrowing of an artery following interventions aimed at taking away obstructions in the blood vessel. Restenosis may for instance occur after a procedure known as Percutaneous Transluminal Coronary Angioplasty.

The primary objective of this procedure is to take away obstructions in the coronary artery and to re-establish a stable blood vessel with a diameter similar to that of the normal artery. This is achieved by inflating a balloon within the coronary artery in order to stretch the blood vessel wall, aimed at taking away a vascular lesion. It has been observed however that the artery may become obstructed again following this procedure.

Recent preclinical studies have indicated that irradiation in the dose range of 15-30 Gy may reduce the problem of restenosis in patients who have undergone an angioplasty. Treatment can be performed by advancing the radioactive source inside the coronary artery to the location of the obstruction by means of a catheter. In this context, the term *brachy* refers to the therapeutic geometry with the radiation source at a short distance from, or in direct contact with the target to be irradiated.

Whereas previously gamma emitters such as ^{192}Ir were used for treatment of restenosis, beta emitters are in principle more suitable; not only do the short spatial range and high dose deposition from beta radiation with energies in the order of 1 MeV allow treatment to be focused in the small diametrical dimensions of a blood vessel (in the order of several millimeters), but also radiation shielding problems are significantly reduced. What is new in the field of intravascular brachytherapy is that much recent effort has been directed towards the development of beta sources.

The aim of Study I is to quantify the absolute dose distribution about the prototype $^{188}\text{W}/^{188}\text{Re}$ beta source for coronary brachytherapy by means of EGS4 Monte Carlo simulations, that provide excellent possibilities for achieving accurate source dosimetry. In particular, (1) the dose deposition over the full radial range up to the maximum possible target depth in the vessel wall and (2) the homogeneity of the dose in the vessel wall in the direction along the lesion must be quantified, as these are decisive for the suitability of the source for the application of restenosis prevention after PTCA. This knowledge of the dose distribution around the source is vital to successful treatment.

In Chapter 2 we present three different simulation models that were used to determine the dose distribution around the $^{188}\text{W}/^{188}\text{Re}$ beta line source. The results for therapeutic depth-dose distributions are compared in Chapter 3, allowing us to gain insight in the quality of the simulation models, as well as in the contributions to the total dose rate from the different radionuclides in the source. In Chapter 4, a comparison is made between simulated and experimental data, after which we present final results for the radial depth-dose distribution in water.

In addition to the above, the air kerma rate that members of the medical staff are exposed to during treatment have been determined in order to estimate the radiation safety of the $^{188}\text{W}/^{188}\text{Re}$ beta source. This issue is addressed in Chapter 5, where we present results for air kerma rates from the source under therapeutic conditions assessed by simulation, analytical calculation and experiment.

Study II: Feasibility of an intraoperative brachytherapy source

Radiation therapy for cancer treatment is often performed during surgery to treat remainders of a tumour (bed) which are not surgically removed. This involves selective irradiation of the tumour (bed) while minimizing the dose deposition in adjacent healthy tissues and organs. A single, large dose boost in the order of 10 Gy is then delivered to a surgically exposed tumour

or tumour bed while displacing or shielding some or all of the dose-limiting radiation-sensitive normal tissues. In such situations, the term intraoperative radiation therapy is used for dose delivery by means of electron beams in the 6 to 18 MeV range produced by a linear accelerators.

It can be problematic to exclusively irradiate complex anatomical structures during surgery, particularly in the pelvis or chest, with available electron IORT techniques. It is often difficult to orientate the equipment such that these regions can be treated adequately without overexposing the adjacent radiation-sensitive organs. In addition, it is quite expensive to either install a linear accelerator into a dedicated surgery room, or to equip a linear accelerator room with surgery facilities. This seriously limits the number of medical centres that use this form of therapy. The alternative of transporting a patient under general anaesthesia from the operating room to the radiation therapy department entails logistic problems.

These constraints have stimulated development of different techniques of more accurate dose delivery to the target site during surgery without overexposing the surrounding dose-restricting organs. In intraoperative brachytherapy (IOBT), selective irradiation of the tumour (bed) can be achieved by using a radioactive source in combination with a source applicator.

The applicator generally consists of a flexible material that can shape to any (surgically exposed) surface to which it is applied. It may contain an array of paths through which the radioactive source is transported, using a preprogrammed dwell time distribution. The applicator thus becomes a radioactive mould for accurate dose deposition in the target area. Furthermore, IOBT equipment is far less expensive than a linear accelerator and involves the use of a portable unit that can be brought into the operating room when needed and that can also be used for other irradiation procedures.

However, the application of IOBT with gamma emitters such as ^{192}Ir is limited by possibilities of radiation shielding due to the relatively high photon energies.

The aim of Study II is therefore to overcome these radiation shielding problems by determining the feasibility of using a low-energy gamma and/or X-ray emitting radionuclide for application in IOBT.

In Chapter 6 we determine the requirements for the radiation output of a potential radionuclide, both in terms of therapeutic dose delivery and radiation safety. On one hand, the photon intensity emitted by the radionuclide should be high enough to achieve the prescribed dose deposition of ~ 10 Gy at the target depth at 1 cm from the source during a treatment time of 20 minutes. On the other hand, it must be possible to shield the personnel from such a high activity radiation source by means of realistic shielding measures that do not impede treatment. In Chapter 7, we translate the above requirements into a selection procedure for the feasibility analysis, which is applied to ^{125}I in order to assess its feasibility for application in IOBT. The selection procedure can be used in further research in order to quantify the suitability of a potential IOBT source.

Study III: Design of an X-ray setup for a multiphase flow metering device

The production of crude oil is often accompanied by large amounts of gas and water. Measurement of the individual oil, water and gas flow rates is required for the purpose of reservoir management and production allocation. Traditionally in oil production, the multiphase flow was separated into its constituent component parts, which allowed straightforward single phase metering techniques to be used. This approach proved to be both practical and effective, although it did involve processing systems like separators which were quite heavy, bulky and expensive.

Therefore, since the early 1980s considerable research has been conducted into more operationally flexible metering technologies: so-called multiphase flow metering (MPFM) techniques. In all of these multiphase flow meters the mass or volume flow rates of the oil, water and gas components through pipelines are determined by means of a combination of instantaneous measurements of e.g. velocities and cross-sectional fraction of each component.

The measurement principle of Dual Energy Gamma Ray Absorption (hereafter: DEGRA) can be used to directly yield the oil, water and gas fractions. The total attenuation of radiation in the mixture is determined by its composition and is energy dependent. In principle, using a radiation source with two different photon energies yields two equations with the three flow component fractions as unknowns. Because the cross-sectional sum of the oil, water and gas fractions equals one, it is possible to solve the system of equations.

The main disadvantage of this technique is that all commercially available gamma or X-ray absorption based multiphase flow meters do, at present, use permanent radioactive sources to generate the gamma or X-rays. Issues like licensing procedures, transportation, on-site safety, disposal and furthermore the social, environmental and emotional barriers which accompany the use of radioactive sources, make their application difficult.

The application of an X-ray tube can help to overcome some of these problems. It maintains the advantages of the superior photon absorption technique while at the same time eliminating all the hazards, cumbersome and extensive licensing procedures and disposal problems attached to the use of radioactive sources. By applying an X-ray tube (that can be switched off) instead of a radioactive source, the hazards which exist during transportation, installation, maintenance or emergency situations can be eliminated. Furthermore, licensing procedures for X-ray equipment are far more relaxed than those applicable to radioactive sources.

Besides this, an X-ray tube can yield additional profits. By using an X-ray tube instead of a radioactive source, one is no longer restricted to fixed radionuclide photon energies but in principle free to choose a number of tunable energies. The high X-ray tube radiation intensities compared to photon intensities emitted by radionuclides will result in improved accuracy in the composition analysis and thus form another advantage of the X-ray tube. Because of these reasons use of an X-ray tube would be preferable. An MPFM device based on X-ray technology is however not yet available to date.

The primary aim of Study III is to design an MPFM device that consists of an X-ray tube instead of a radioactive source. The additional aim is to attain an integrated determination of the salinity (the salt concentration in the water).

In Chapter 8 we discuss the theory of multiphase flow metering based on photon absorption, the technique of the meter that is used at present and the requirements on the X-ray MPFM device. Furthermore, results are presented from simulations on the sensitivity and accuracy aspects of the different X-ray based MPFM principles.

These results are used in Chapters 9 and 10 for the modelling of different types of X-ray set-ups by means of EGS4 simulations, in order to assess the design of an MPFM device that yields optimum X-ray spectra. The ultimate measurement principle is based upon the use of X-ray spectra characterized by various monoenergetic high intensity peaks, superposed on a background continuum of considerably lower intensity (in the order of a factor 100 to 1000). The monoenergetic peaks are provided by secondary fluorescence; a number of thin foils is irradiated at a short distance from the X-ray tube with the primary bremsstrahlung continuum to generate the characteristic radiation with the desired energies. Based upon the results, we also present in Chapter 10 the prototype X-ray set-up for MPFM.

Ontwerpstudies voor Cardiovasculaire & Intra-operatieve Brachytherapie en “Multiphase Flow Metering”

Nieuwe toepassingen van straling in de geneeskunde en de industrie

Samenvatting

In dit proefschrift worden drie ontwerpstudies van nieuwe toepassingen van straling in de geneeskunde en de industrie samengevat. Studies I en II laten zien dat beta-, en lage-energie fotonstraling waardevolle instrumenten zijn voor respectievelijk cardiovasculaire en intra-operatieve brachytherapie. In studie III worden de diagnostische eigenschappen van fotonstraling aangewend voor de industriële toepassing van zogeheten *non-invasive flow metering*.

Studie I: Het modelleren van een $^{188}\text{W}/^{188}\text{Re}$ beta lijnbron voor coronaire brachytherapie door middel van EGS4 Monte Carlo simulaties

Het voorkomen van restenosis vormt een relatief nieuwe therapeutische toepassing van straling. Restenosis kan gedefinieerd worden als het zich opnieuw vernauwen van een (slag)ader na afloop van een medische ingreep die tot doel heeft een verstopping in een bloedvat te verwijderen. Restenosis kan zich bijvoorbeeld voordoen na zogeheten Percutane Transluminale Coronaire Angioplastie.

Deze procedure is in de eerste plaats bedoeld om de verstopping in de krans(slag)ader ongedaan te maken, hetgeen moet leiden tot een stabiel bloedvat met een diameter gelijk aan die van de normale ader. Een kleine ballon wordt opgeblazen in de krans(slag)ader, waardoor de wanden van het bloedvat worden opgerekt, hetgeen moet resulteren in de verwijdering van

de vaatvernauwing. Het blijkt nochtans dat de ader relatief snel opnieuw verstopt kan raken na deze medische behandeling.

Recentelijk uitgevoerd preklinisch onderzoek heeft aangetoond dat bestraling van de vaatwand met ioniserende straling in het dosisgebied van 15-30 Gy het probleem van restenosis kan verminderen voor patiënten die een angioplastie hebben ondergaan. De behandeling kan worden uitgevoerd door een radioactieve bron in de krans(slag)ader in te brengen en te transporteren naar de positie van de vaatverstopping met behulp van een katheter. In dit verband verwijst de term *brachy* naar de therapeutische geometrie met de stralingsbron op korte afstand van, of in direct contact met het te bestralen weefsel of orgaan.

Daar waar vroeger gammastraling uitzendende radionucliden zoals ^{192}Ir werden gebruikt voor de behandeling van restenosis, zijn betastraling uitzendende radionucliden in beginsel meer geschikt; de korte ruimtelijke dracht en hoge dosisdepositie van betastraling met energieën in de orde van 1 MeV maakt het mogelijk de behandeling te concentreren binnen de kleine diametrale afmetingen van een bloedvat (in de orde van enkele millimeters). Daarnaast zijn er aanzienlijk minder aan stralingsveiligheid gerelateerde problemen bij het gebruik van een betastraling uitzendend radionuclide. Een nieuw aspect binnen de intravasculaire brachytherapie is dat er de laatste tijd veel onderzoek verricht wordt naar de ontwikkeling van betabronnen.

Het doel van Studie I is het kwantificeren van de absolute dosisverdeling rondom de prototype $^{188}\text{W}/^{188}\text{Re}$ betabron voor coronaire brachytherapie door middel van EGS4 Monte Carlo simulaties, die uitstekende mogelijkheden bieden om nauwkeurig dosimetrie te bestuderen. In het bijzonder dienden gekwantificeerd te worden: (1) de dosisdepositie binnen het volledige radiële gebied tot aan de maximaal mogelijk *target* diepte in de vaatwand en (2) de homogeniteit van de dosis in de vaatwand, in de richting van de lesie. Dit aangezien (1) en (2) de geschiktheid van de bron bepalen voor de toepassing van het voorkomen van restenosis na PTCA. De kennis van de dosisverdeling rondom de bron is van essentieel belang voor succesvolle medische behandeling.

In hoofdstuk 2 worden de drie verschillende simulatiemodellen gepresenteerd, waarmee de dosisverdeling rondom de $^{188}\text{W}/^{188}\text{Re}$ beta lijnbron is bepaald. De vergelijking van de resultaten voor de therapeutische dieptedosisverdelingen komt aan bod in hoofdstuk 3; dit stelt ons in staat inzicht te verkrijgen in de kwaliteit van de simulatiemodellen, alsmede in de bijdragen van de verschillende radionucliden in de bron aan het totale dosistempo. In hoofdstuk 4 wordt een vergelijking gemaakt tussen gesimuleerde en experimentele data, waarna we de definitieve resultaten voor de radiale dieptedosisverdeling in water presenteren.

Het vraagstuk van stralingsveiligheid wordt behandeld in hoofdstuk 5, waarin we resultaten presenteren in de vorm van luchtkermatempi rondom de bron, geldend voor verschillende therapeutische omstandigheden. De resultaten hiervan zijn bepaald door middel van simulaties, analytische berekeningen en metingen.

Studie II: Haalbaarheidsstudie van een intra-operatieve brachytherapiebron

Stralingstherapie ter bestrijding van kanker wordt vaak uitgevoerd in combinatie met chirurgie. Dit maakt het mogelijk de niet chirurgisch te verwijderen restanten van de tumor (of het tumorbed) selectief te bestralen, terwijl de dosisdepositie in aangrenzende gezonde weefsels en organen geminimaliseerd wordt. Hierbij wordt een eenmalige, hoge stralingdosis in de orde van 10 Gy (de zogeheten dosis *boost*) afgegeven in een chirurgisch blootgelegde tumor (of tumorbed), waarbij tegelijkertijd de stralingsgevoelige en dosisbeperkende normale weefsels verplaatst of afgeschermd worden. In deze situaties wordt de term intra-operatieve stralingstherapie gebezigd om dosisafgifte door middel van elektronenbundels, afkomstig van lineaire versnellers in het energiegebied van 6 tot 18 MeV, aan te duiden.

Het kan problematisch zijn om met de beschikbare elektronenbundeltechnieken uitsluitend bepaalde anatomische structuren te bestralen, in het bijzonder in het bekken of de borst. Vaak is het moeilijk de apparatuur zodanig te oriënteren dat deze gebieden adequaat behandeld kunnen worden, zonder dat daarbij de aangrenzende stralingsgevoelige organen een te hoge stralingsdosis oplopen. Bovendien is het een tamelijk kostbare zaak om een lineaire versneller in een daartoe uitgeruste operatiekamer te installeren, danwel een ruimte voor lineaire versnellers te voorzien van operatiefaciliteiten. De alternatieve oplossing, waarbij de patiënt onder algehele verdoving verplaatst wordt van de operatiekamer naar de afdeling radiotherapie, gaat gepaard met logistieke problemen.

Deze beperkingen hebben een impuls gegeven aan de ontwikkeling van technieken voor meer precieze dosisafgifte aan het tijdens een operatie te bestralen weefsel of orgaan, zonder dat daarbij de omliggende dosisbeperkende organen een te hoge stralingsdosis oplopen. In intra-operatieve brachytherapie (IOBT) kan selectieve bestraling van de tumor (of het tumorbed) bereikt worden door middel van een radioactieve bron in combinatie met een zogeheten bronapplicator.

De applicator bestaat in het algemeen uit een flexibel materiaal, dat zich kan vormen naar ieder (chirurgisch blootgelegd) oppervlak waartegen het wordt aangebracht. Hij kan opgebouwd zijn uit een aantal parallel liggende kanalen waarbinnen de radioactieve bron getransporteerd wordt volgens een voorgeprogrammeerde verblijfstijdverdeling; op deze manier vormt de applicator een radioactieve *mal* voor nauwkeurige dosisafgifte in het te bestralen gebied. Daarnaast is de benodigde uitrusting voor IOBT verreweg goedkoper dan een lineaire versneller. Er wordt gebruik gemaakt van een draagbare eenheid die voor IOBT naar de operatiekamer gebracht kan worden, maar daarnaast ook voor andere bestralingsprocedures beschikbaar is.

Desalniettemin wordt de toepassing van IOBT met gammastraling uitzendende radionucliden zoals ¹⁹²Ir beperkt door de mogelijkheden van stralingsafscherming, tengevolge van de relatief hoge fotonenergieën.

Studie II is erop gericht deze problemen met stralingsafscherming het hoofd te bieden door de haalbaarheid vast te stellen van het gebruik van een radionuclide, dat lage-energie gamma- of röntgenstraling uitzendt.

In hoofdstuk 6 bepalen we de eisen aan de stralingsopbrengst van een potentieel radionuclide, zowel wat betreft de therapeutische dosisafgifte als de stralingsveiligheid. Enerzijds dient de intensiteit van de door het radionuclide uitgezonden fotonen hoog genoeg te zijn, teneinde de voorgeschreven dosisafgifte van ~ 10 Gy op de beoogde afstand van 1 cm van de bron tot stand te brengen binnen een behandelingsduur van 20 minuten. Anderzijds moet het mogelijk blijven het medisch personeel af te schermen van een bron met (zodanig) hoge activiteit en wel met realistische afschermingsmaatregelen die geen belemmering vormen voor de behandeling. In hoofdstuk 7 vertalen we de bovengenoemde eisen in een selectieprocedure voor de haalbaarheidsanalyse, die is toegepast bij de bepaling van de haalbaarheid van ^{125}I voor IOBT. In een vervolgonderzoek kan de selectieprocedure gebruikt worden om de geschiktheid van andere potentiële radionucliden te kwantificeren.

Studie III: Ontwerp van een op het gebruik van röntgenstraling gebaseerde opstelling voor multiphase flow metering

Het winnen van ruwe olie gaat vaak gepaard met grote hoeveelheden gas en water. Metingen van de individuele olie-, water-, en gasstromen zijn dan ook noodzakelijk voor het beheer van de reservoirs en de toewijzing van de productie. Zoals van oudsher gebruikelijk in de oliewinning, werden de componenten van de *multiphase flow* allereerst gescheiden, waarna *single phase* meettechnieken gebruikt konden worden. Deze benadering bleek zowel praktisch als effectief te zijn, alhoewel zij gebaseerd was op bijvoorbeeld scheidingssystemen die tamelijk zwaar, omvangrijk en duur waren.

Dientengevolge is er sinds het begin van de jaren '80 aanzienlijk veel onderzoek verricht naar meer flexibele meettechnologieën: zogeheten *multiphase flow metering* (MPFM) technieken. Bij al deze multifase-stromingsmetingen worden de massieke stromingssnelheden van ieder van de componenten olie, water en gas in de oliepijpleiding bepaald door middel van instantane metingen van de snelheid en het fractioneel aandeel in een dwarsdoorsnede van de oliepijpleiding.

Het meetprincipe van *Dual Energy Gamma Ray Absorption* (DEGRA) maakt het mogelijk om direct de afzonderlijke fracties olie, water en gas vast te stellen. De totale verzwakking van straling wordt bepaald door de samenstelling van het mengsel en is energieafhankelijk. In principe levert het gebruik van twee fotonenergieën twee vergelijkingen op, terwijl er drie onbekende componenten in de stroming zijn. Aangezien er een derde vergelijking is, die uitdrukt dat de som van de fracties gelijk is aan 1, kan het systeem van vergelijkingen opgelost worden.

Het voornaamste nadeel van deze techniek is dat alle commercieel beschikbare *flow meters*, gebaseerd op het gebruik van absorptie van gamma-, of röntgenstraling, tot op heden

gebruik maken van permanent radioactieve bronnen. De toepassing daarvan wordt in het bijzonder belemmerd door de daarmee samenhangende procedures voor het verkrijgen van vergunningen, het transport, de uitgebruikname en de bijbehorende veiligheidsmaatregelen. Bovendien zijn er de sociale en milieu-gerelateerde barrières, die gepaard gaan met het gebruik van radioactieve bronnen en evenzoo het gebruik daarvan bemoeilijken.

Het gebruik van een röntgenbuis kan helpen deze problemen het hoofd te bieden. Niet alleen blijven de voordelen van de superieure, op fotonabsorptie gebaseerde techniek behouden, tegelijkertijd worden alle omslachtige en langdurige procedures voor het verkrijgen van vergunningen en de uitgebruikname van radioactieve bronnen overbodig gemaakt (de procedures voor het verkrijgen van vergunningen voor röntgenapparatuur zijn aanzienlijk minder veeleisend dan die voor radioactieve bronnen). Door toepassing van een röntgenbuis (die uitgeschakeld kan worden) in plaats van een radioactieve bron wordt de intrinsieke onveiligheid tijdens transport, installatie, onderhoud of noodsituaties geëlimineerd.

Daarnaast biedt het gebruik van een röntgenbuis nog meer voordelen: waar men bij het gebruik van een radionuclide op voorhand wordt beperkt wordt door de beschikbare fotonenergieën, is het nu mogelijk een aantal af te stemmen energieën te kiezen. De hoge intensiteit van röntgenstraling -in vergelijking met die van door radionucliden uitgezonden straling- zullen leiden tot hogere nauwkeurigheden in de analyse van de fracties en vormen dus een ander pluspunt van het gebruik van een röntgenbuis. Vanwege deze redenen verdient de toepassing van een röntgenbuis de voorkeur. Er is echter tot op heden geen MPFM apparatuur beschikbaar, gebaseerd op het gebruik van röntgenstralingstechnologie.

Het primaire doel van Studie III is het ontwerp van een MPFM instrument dat bestaat uit een röntgenbuis in plaats van een radioactieve bron. Het uitvoeren van een geïntegreerde meting van het zoutgehalte van het water vormt hierbij een additioneel streven.

In hoofdstuk 8 behandelen we de theorie van multiphase flow metering gebaseerd op fotonabsorptie, de techniek van het instrument dat momenteel hiervoor gebruikt wordt en de geldende eisen aan een op het gebruik van röntgenstraling gebaseerd MPFM instrument. Daarnaast worden resultaten gepresenteerd van simulaties aan de gevoeligheids-, en nauwkeurigheidsaspecten van de verschillende MPFM principes.

Deze resultaten worden in hoofdstuk 9 en hoofdstuk 10 gebruikt voor het modelleren van verschillende röntgenstralingsopstellingen, teneinde het ontwerp te bepalen van een MPFM instrument dat optimale röntgenspectra oplevert. Het uiteindelijke meetprincipe is gebaseerd op het gebruik van röntgenspectra, gekenmerkt door verscheidene mono-energetische pieken met hoge intensiteit, gesuperponeerd op een continue achtergrondstraling met aanzienlijk lagere intensiteit (in de orde van een factor 100 tot 1000). De mono-energetische pieken worden geleverd door het principe van secundaire fluorescentie, waarbij een aantal dunne folies van dichtbij wordt bestraald met het primaire remstralingspectrum van de röntgenbuis. Ten gevolge hiervan wordt in de folies karakteristieke straling met de gewenste energieën gegenereerd. In hoofdstuk 10 presenteren we tevens het prototype van de opstelling voor multiphase flow metering door gebruik van röntgenstraling.

Dankwoord / Acknowledgements

Tijdens het schrijven van dit proefschrift heb ik veel respect gekregen voor monniken en stoffige boekhouders. Daar waar zij zich jaren aaneen in stille afzondering aan een nauwgezette taak kunnen wijden, moet ik nu al bekennen blij te zijn dat het schrijven van dit boekje erop zit. En wat is dan een krap jaar, dat daar voor stond? Een periode van verzamelen, opzetten, uitwerken, corrigeren, toelichten en bijschaven. Je eigen gangen nagaan, puzzelen over de juiste verwoording. Kortom, een tropenjaar, met veel koffie.

Toch gaat het te ver om het schrijven van een proefschrift af te schilderen als een pure solo-trip. Er is een aanzienlijk aantal mensen dat in belangrijke mate heeft bijgedragen aan de totstandkoming van dit proefschrift. Hen wil ik hier noemen en bedanken.

Allereerst wil ik mijn promotor Carel van Eijk bedanken. Carel, hoe vol je bureau ook ligt met allerhande paperassen, er is altijd wel een hoekje vrij te maken voor een kort overleg, een snelle suggestie of een vraag van mijn kant. Bij gebrek aan een vooraf aangewezen begeleider gedurende mijn promotieperiode was jij meestal degene tot wie ik mij meende te moeten richten. Dat dit vrijwel altijd mogelijk was zonder voorafgaande afspraak, waardeer ik enorm.

Daarnaast wil ik hier met nadruk Dennis Schaart noemen. Dennis, het lijkt wel of je bij jou op ieder moment van de dag aan kunt komen voor een wetenschappelijke discussie. In de kroeg over de onzekerheidsrelatie van Heisenberg, of een maar voortdurende discussie over de normalisatie van een betaspectrum (factortje 2.???). Voor al de uitvoerige hulp, de grondige reviews en de vele toegestopte artikelen: ik kon van je op aan. Bedankt!

Victor Bom wil ik bedanken voor de fijne samenwerking en de GEANT simulaties die hij voor me heeft uitgevoerd. Johan de Haas bedank ik voor het hanteerbaar maken van dosimetriedata. Nu ik toch bezig ben: Johan, ik wens je het allerbeste toe, maar dat geldt niet voor die club van je. Wat mij betreft blijven die gasten gewoon dezelfde lijn aanhouden van de afgelopen jaren.

Adrie Bos en August Winkelman bedank ik voor hun samenwerking in het $^{188}\text{W}/^{188}\text{Re}$ project. Verder wil ik José Buurman en mijn (ex-)kamergenoten Olivier Guillot-Noël en Cor Datema bedanken voor de vele aangename discussies, lang niet altijd over voetbal! Jelle, hartelijk bedankt voor al je hulp bij het oplossen van allerhande computerproblemen. En dan natuurlijk de rest van de ISO-groep; ieder van hen die ik hier niet met name noem, bedankt voor de prettige sfeer in de vakgroep gedurende de afgelopen vier jaar. Jan van Waarden wil ik bedanken voor het ontwerpen van de omslag van dit proefschrift.

I am grateful to: Wim Dries for his help in performing simulations on the microdosimetry of the beta line source, Mr. Namito for providing the EII patches, and Martin Caon, Mr. Hirayama and Mr. Bielajew for the long discussions about EGS4. In general, I would like to thank all the people contributing to the discussions at the EGS4 e-mail forum. I believe this medium is indispensable to all EGS4 users. I thank Nucletron B.V. and Lex Scheers, Joop Frieling and Ton Reimerink from Shell International Exploration and Production B.V. for their cooperation and funding that made the studies in this thesis possible. Furthermore, I would like to thank Zvonko Kolar and the Rangers and Celtic fans from Daniel Europe ltd., Larbert, Scotland for their cooperation in the joint MPFM project.

Er zijn een hoop niet-collega's die minstens zo belangrijk voor me zijn geweest in de afgelopen jaren. Niet ieder van hen kan ik hier noemen, hoe graag ik ook zou willen. Maar aan de foutmanne kan ik moeilijk voorbijgaan. Deze hechte en bonte club vrienden zorgt al jaren voor de broodnodige verstrooiing, die met wetenschap nagenoeg niets van doen heeft. Maar belangrijk is het wel, onmisbaar zou ik willen zeggen. Jongens, bedankt, en hou 't breed!

Met nadruk bedank ik mijn ouders, broer en zus voor hun liefdevolle interesse en betrokkenheid. Ditzelfde geldt voor mijn vriendin Vivian. Viv, jij was het die me met je luisterend oor, relativerend advies en eindeloos geduld telkens weer motiveerde en over menig dood punt heen wist te helpen. Bedankt!

Curriculum Vitae

De auteur van dit proefschrift werd geboren op 21 januari 1971 te Schiedam. Aan de in diezelfde plaats gelegen scholengemeenschap Spieringshoek behaalde hij in 1989 het VWO-B diploma. Aansluitend begon hij met de studie Technische Natuurkunde aan de Technische Universiteit te Delft. Het afstudeeronderzoek onder begeleiding van dr. Herbert Smorenburg werd verricht in de vakgroep Stralingsfysica van het Interfacultair Reactor Instituut (IRI), onderdeel van de Technische Universiteit Delft. Dit onderzoek bestond uit twee delen: enerzijds het bestuderen van de dynamica van helium-argon edelgasmengsels door middel van inelastische neutronenverstrooiing, anderzijds het bepalen van de structuur van diaminobutaandendrimeren met behulp van kleine-hoek neutronenverstrooiing. In maart 1996 legde hij het doctoraalexamen af en trad als toegevoegd onderzoeker in dienst bij de vakgroep Stralingstechnologie (ST) van het IRI. De resultaten van een groot deel van het sindsdien uitgevoerde onderzoek zijn vastgelegd in dit proefschrift.

